

2015-01-01

High Temperature Oxidation of Nb-Cr-Mo-Si-B Alloys

Kathryn S. Thomas

University of Texas at El Paso, ksthenas2457@gmail.com

Follow this and additional works at: https://digitalcommons.utep.edu/open_etd



Part of the [Materials Science and Engineering Commons](#), and the [Mechanics of Materials Commons](#)

Recommended Citation

Thomas, Kathryn S., "High Temperature Oxidation of Nb-Cr-Mo-Si-B Alloys" (2015). *Open Access Theses & Dissertations*. 1168.
https://digitalcommons.utep.edu/open_etd/1168

This is brought to you for free and open access by DigitalCommons@UTEP. It has been accepted for inclusion in Open Access Theses & Dissertations by an authorized administrator of DigitalCommons@UTEP. For more information, please contact lweber@utep.edu.

HIGH TEMPERATURE OXIDATION
OF Nb-Cr-Mo-Si-B ALLOYS

KATHRYN SUZANNE THOMAS

Department of Metallurgical and Materials Engineering

APPROVED:

Shailendra K. Varma, Ph.D., Chair

Stephen W. Stafford, Ph.D.

Juan C. Noveron, Ph.D.

Felicia S. Manciu, Ph.D.

Charles Ambler, Ph.D.

Dean of the Graduate School

Copyright ©

by

Kathryn Suzanne Thomas

2015

Dedication

Dedicated to my parents:

John & Diane

HIGH TEMPERATURE OXIDATION
OF Nb-Cr-Mo-Si-B ALLOYS

by

KATHRYN SUZANNE THOMAS, B.S. MME

DISSERTATION

Presented to the Faculty of the Graduate School of

The University of Texas at El Paso

in Partial Fulfillment

of the Requirements

for the Degree of

DOCTOR OF PHILOSOPHY

Doctoral Program in Materials Science and Engineering

THE UNIVERSITY OF TEXAS AT EL PASO

May 2015

Acknowledgements

It is my honor to have worked with Dr. S. K. Varma these last few years as I investigated these alloys. It is thanks to the opportunity he provided, his patience, and especially the support he has tirelessly given that I have been able to do this work. I would like to thank Dr. Stafford, Dr. Noveron, and Dr. Manchiu for their time as members of my committee. I would also like to acknowledge the support and guidance of the faculty of the Materials Science and Engineering program during my tenure at UTEP. I would like to acknowledge the financial support of the Metallurgical and Materials Engineering Department as well as that of the Office of Naval Research and Dr. David Shiffler through the project #N00014-08-0506. Finally, I would like to thank my parents and friends who put up with me and gave me support as I proceeded through this work.

Abstract

It has been the trend to use nickel based superalloys in high temperature applications, however higher temperatures are required in the effort to enhance the efficiency of such components as jet turbine engines. The melting temperature of the nickel based superalloy limits the extent to which temperature can be raised as these materials are typically used at temperatures within 200 degrees of their melting point. Refractory metal based systems are attractive due to their high melting points, low densities, and good high temperature strength. However, in such cases as niobium, poor oxidation resistance limits the widespread use of such alloys. The development of new alloy systems that retain the desirable characteristics of the refractory metal while reducing the oxidation of the system is one of the goals of several studies.

For this study the compositions of the alloys in atomic percent are Nb-25Cr-20Mo-15Si-10B, Nb-25Cr-20Mo-15Si-15B, Nb-25Cr-15Mo-15Si-15B, Nb-25Cr-15Mo-20Si-15B, and Nb-25Cr-15Mo-20Si-10B. The oxidation behavior and microstructural characteristics of these alloys is studied in the temperature range of 700-1400°C. Oxidation is performed in air from 24 hours up to two weeks (336 hours) of exposure time. The kinetics of oxidation will be compared through the weight gain per area method. Oxidation products are a mixture of CrNbO_4 , Nb_2O_5 , and SiO_2 , the amounts of which are dependent on the phase content. An intermediate oxidation layer which appears to be protective has been found to form in this system with high boron content. Increasing the amount of boron content within the alloy has proven to enhance high temperature oxidation resistance after exposure of a period of two weeks. Examination of oxidation products and microstructural evolution with increased temperature was carried out utilizing x-ray diffraction and scanning electron microscopy in secondary, backscatter imaging modes, energy dispersive spectroscopy, and x-ray mapping.

Table of Contents

Acknowledgements.....	v
Abstract.....	vi
Table of Contents.....	vii
List of Tables	ix
List of Figures.....	x
Chapter 1: Introduction.....	1
1.1 Justification.....	2
Chapter 2: Literature Review.....	4
2.1 Refractory Metals and High Temperature Applications.....	4
2.2 Oxidation of Nb and Nb-based Alloys	5
2.3 Development of the Nb-Cr-Mo-Si-B System	7
2.4 Alloy Phases	9
2.5 Oxidation Mechanisms and Kinetics	13
2.6 Oxide Volatilization.....	18
Chapter 3: Experimental Methods	20
3.1 Sample Preparation	20
3.2 Gibbs Free Energy Modeling.....	20
3.3 Oxidation	21
3.4 X-Ray Diffraction	22
3.5 Scanning Electron Microscopy	22
3.6 Image Analysis	23
Chapter 4: Results and Discussion	24
4.1 Isothermal Modeling of the Nb-Cr-Mo-Si System.....	24
4.3 Oxidation of Nb-25Cr-20Mo-15Si-(10, 15)B.....	28
4.4 Oxidation of 15Mo Containing Alloys	67

Chapter 5: Summary and Conclusions	97
Recommendations and Future Work	101
Vita	106

List of Tables

Table 2.1: Basic properties of some refractory metals.	4
Table 2.2: Selected properties of the pure components of the alloys under investigation.	9
Table 3.1: The compositions of the experimental alloys with the weight percent given as indicated by Ames Lab.	20
Table 4.1: Phase fractions calculated for as-cast state of 10B and 15B alloys at 1000X.	31
Table 4.2: Literature values of the coefficient of thermal expansion for oxides and the phases of the study.	99
Table 4.3: Phase fractions calculated for as-cast state of alloys at 1000X.	72

List of Figures

Figure 1.1: Diagram of a single stage turbine engine.....	1
Figure 2.1: Alloy development map, bolded compositions are those utilized in this study.	8
Figure 2.2: The three lattice arrangements for the Laves phase (a) C14, (b) C15, and (c) C36, adopted from [19].	10
Figure 2.3: Tetrahedron formed by the B atoms in the three lattice arrangements for the Laves phase (a) C14, (b) C15, and (c) C36, adopted from [19].	10
Figure 2.4: The adapted metal-oxygen reaction schematic [5].	14
Figure 2.5: Adapted graphical representation of the three rate laws in arbitrary units [29].	16
Figure 2.6: Oxidation behavior observed in two phase alloys (a) independent oxidation forming a non-uniform scale, (b) cooperative oxidation forming a uniform scale, and (c) solute rich phase acts a reservoir for growth of solute scale [33].	18
Figure 4.1: The Nb-rich portion of the isothermal section calculated at room temperature (25°C) for the Nb-Cr-Mo-Si System, where * indicates for both 10 and 15% B concentrations.	25
Figure 4.2: Isothermal sections for the Nb-25Cr-Mo-Si system at selected temperatures to model the phase changes expected in the system.	26
Figure 4.3: Phase fraction curves developed for (a) 10B & 15B, (b) 1515, and (c) 2010 & 2015 alloys.	27
Figure 4.4: Phase fraction curves developed for the (a) 10B & 15B, (b) 1515, and (c) 2010 & 2015 alloys from 700 to 1400°C.	28
Figure 4.6: As-cast microstructure of the 10B alloy at (a) 250X and (b) 1000X magnification.	30
Figure 4.7: As-cast microstructure for 15B alloy at (a) 250X and (b) 1000X magnification.	30
Figure 4.8: Oxidation curve developed for the 10B and 15B alloys at 700°C during two weeks of cyclic oxidation and the curve developed during static oxidation.	32
Figure 4.9: Macro images of the pest oxidation exhibited by the 10B samples after 14-days of exposure at 700°C in cyclic (2LTO) and static (14S) modes.	32
Figure 4.10: X-Ray diffraction results for 10B and 15B alloys after two weeks of cyclic and static oxidation at 700°C, scans of the 14S sample is characteristic of those found for the successive static exposures.	33
Figure 4.11: Microstructure morphology for the 10B sample during static testing compared with the cyclic sample.	35
Figure 4.12: Microstructure morphology for the 15B sample during static testing compared with the cyclic sample.	36
Figure 4.13: Low-magnification images for the cross sections of the 10 and 15B alloys after two weeks of static exposure.	36
Figure 4.14: Oxide-metal interface developed during static exposure at 700°C after stated period of days for the 10 and 15B alloys.	37
Figure 4.15: Oxide-metal interface developed during cyclic exposure at 700°C for the 10 and 15B alloys.	37
Figure 4.16: Oxidation curve developed for the 10B and 15B alloys at 900°C during two weeks of cyclic oxidation and the curve developed during static oxidation.	38
Figure 4.17: Microstructure morphology for the 10B sample during static testing at 900°C compared with the cyclic sample.	39
Figure 4.18: Microstructure morphology for the 15B sample during static testing at 900°C compared with the cyclic sample.	39

Figure 4.19: X-Ray diffraction results for 10B and 15B alloys after two weeks of cyclic and static oxidation at 900°C, scans of the 14S sample is characteristic of those found for the successive static exposures.	40
Figure 4.20: Oxide-metal interface developed during static exposure at 900°C after indicated period of days for the 10B alloy.	41
Figure 4.21: Oxide-metal interface developed during cyclic exposure at 900°C for the 10B alloy.	42
Figure 4.22: Oxide-metal interface developed during static exposure at 900°C after indicated period of days and oxide developed during cyclic testing for the 15B alloy.	43
Figure 4.23: EDS map of Cr showing thin depletion layer developed in both the 10 and 15B samples during cyclic testing.	44
Figure 4.24: Oxidation curve developed for the 10B and 15B alloys at 1100°C during two weeks of cyclic oxidation and the curve developed during static oxidation.	45
Figure 4.25: Microstructure morphology for the 10B sample during static and cyclic testing at 1100°C.	46
Figure 4.26: Microstructure morphology for the 15B sample during static and cyclic testing at 1100°C.	46
Figure 4.27: X-Ray diffraction results for 10B and 15B alloys after two weeks of cyclic and static oxidation at 1100°C, scans of the 14S sample is characteristic of those found for the successive static exposures.	47
Figure 4.28: Oxide-metal interface developed at 1100°C after stated period of days for the 10 and 15B alloys.	48
Figure 4.29: Low magnification images of the oxide scale developed for the 10B sample at 1100°C after cyclic and static exposure for two weeks.	48
Figure 4.30: EDS mapping of the oxide-metal interface developed in the 10B sample at 1100°C.	49
Figure 4.31: Magnification of region indicated in Fig.4.28.	50
Figure 4.32: EDS mapping of the oxide-metal interface developed in the 15B sample at 1100°C.	51
Figure 4.33: Oxidation curve developed for the 10B and 15B alloys at 1300°C during two weeks of cyclic oxidation and the curve developed during static oxidation.	52
Figure 4.34: Microstructure morphology for the 10B and 15B samples during static and cyclic oxidation at 1300°C after 14 days of exposure.	53
Figure 4.35: X-Ray diffraction results for 10B and 15B alloys after two weeks of cyclic and static oxidation at 1300°C, scans of the 14S sample is characteristic of those found for the successive static exposures.	54
Figure 4.36: Oxide-metal interface developed at 1300°C after static oxidation for stated period of days for the 10 and 15B alloys.	55
Figure 4.37: Oxide-metal interface developed at 1300°C after cyclic oxidation of 10 and 15B alloys.	55
Figure 4.38 Composite images of the oxide developed for the 15B sample exposed at 1300°C after 14 days static oxidation.	56
Figure 4.39: Characteristic EDS scan developed for the SiO ₂ layer developed in the 15B alloy.	57
Figure 4.40: Composite image of the oxide developed for the 15B sample exposed at 1300°C after 12 days static oxidation.	57
Figure 4.41: Un-oxidized NbCr ₂ found near the center of the sample surrounded by CrNbO ₄	58
Figure 4.42: Gravimetric curves developed for the 10 and 15B alloy after three weeks of cyclic oxidation.	59
Figure 4.43: Morphology of the 10B alloy with temperature during three week cyclic oxidation.	59
Figure 4.44: Morphology of the 15B alloy with temperature during three week cyclic oxidation.	60
Figure 4.45: XRD patterns developed for the 10 and 15B alloys during three week cyclic exposure.	60
Figure 4.46: Oxide surface and oxide metal interface developed for the 10B and 15B alloys at 700°C.	61

Figure 4.47: Oxide surface and oxide metal interface developed for the 10B and 15B alloys at 900°C.	62
Figure 4.48: Oxide surface and oxide metal interface developed for the 10B and 15B alloys at 1100°C and EDS map of Cr.	64
Figure 4.49: Oxide surface and cross sectional micrograph of full oxide scale developed for the 10B and 15B alloys at 1300°C.	65
Figure 4.50: EDS map of the oxide metal interface developed for the 10B alloy at 1300°C.	66
Figure 4.51: EDS map of the oxide metal interface developed for the 15B alloy at 1300°C.	66
Figure 4.53: As-cast microstructure of the Nb-25Cr-15Mo-15Si-15B alloy at (a) 250X and (b) 1000X magnification.	69
Figure 4.54: EDS mapping of the 1515 alloy.	69
Figure 4.55: As-cast microstructure of the 2010 alloy (a) 250X and (b) 1000X magnification.	70
Figure 4.57: As-cast microstructure of the 2015 alloy at (a) 250X and (b) 1000X magnification, (c) magnified view of indicated region, (d) the same region in secondary imaging.	71
Figure 4.58: EDS mapping of the 2015 alloy.	72
Figure 4.59: Gravimetric curves for short term oxidation of the alloys developed after 24 hours of exposure at each specified temperature.	74
Figure 4.60: Macro images of samples after 24 hours oxidation at indicated temperature.	75
Figure 4.61: XRD patterns obtained for the alloys after 24 hours oxidation.	76
Figure 4.62: Oxide metal interfaces developed after short term oxidation at indicated temperature for the 1515, 2010, and 2015 alloys; micrographs collected in secondary imaging mode.	77
Figure 4.63: Oxide metal interfaces developed after short term oxidation at indicated temperature for the 1515, 2010, and 2015 alloys; micrographs collected in secondary imaging mode.	78
Figure 4.64: XRD patterns obtained for the alloys after cyclic oxidation.	79
Figure 4.65: Gravimetric curves developed for the 15Mo alloys after cyclic oxidation at a) 700°C, b) 800°C, and c) 900°C.	80
Figure 4.66: Oxide metal interface developed for the 1515, 2010, and 2015 samples after cyclic oxidation at 700°C, 800°C and 900°C.	81
Figure 4.67: Gravimetric curves developed for the 15Mo alloys after cyclic oxidation at 1000°C.	82
Figure 4.68: Oxide metal interface developed for the 15Mo alloys after cyclic oxidation at 1000°C.	83
Figure 4.69: Gravimetric curves developed for the 15Mo alloys after cyclic oxidation at a) 1100°C, b) 1200°C, and c) 1300°C.	84
Figure 4.70: Bulk metal remaining for the 1515 alloy at 1100°C at a) low magnification, b) high magnification of the Laves phase showing precipitated Mo ₅ Si ₃ and c) at 1200°C.	85
Figure 4.71: Bulk metal remaining for the 2010 alloy at 1300°C.	85
Figure 4.72: Bulk metal remaining for the 2015 alloy at a) 1100°C – low magnification, b) 1100°C – high magnification of Laves region, c) 1200°C – low magnification, d) 1200°C – high magnification of Laves region, e) 1300°C – low magnification, f) 1300°C – high magnification of Laves region.	86
Figure 4.73: Oxide metal interface developed for the 1515, 2010, and 2015 samples exposed at 1100°C, 1200°C, and 1300°C.	87
Figure 4.74: Gravimetric curves developed for the 15Mo alloys after cyclic oxidation at 1400°C.	88
Figure 4.75: Bulk metal remaining for the 15Mo alloys after cyclic oxidation at 1400°C, internal oxidation of Si-containing phases to form SiO ₂ occurs in all samples.	89
Figure 4.76: Oxide metal interface developed for the 15Mo alloys after cyclic oxidation at 1400°C.	90
Figure 4.77: Weight gain data for the alloys obtained after a week of static exposure.	91
Figure 4.72: Oxide and microstructure of metal remaining for the alloys after 7 days static oxidation at 700°C.	93
Figure 4.75: Oxide metal interface for the alloys after 7 days static oxidation at 1300°C.	96

Chapter 1: Introduction

Since the inception of the first turbo-jet engine in the 1930s there has been a great deal of interest in increasing the power and capabilities of these engines. While modern jet engines are a complex system of various materials there is still the basic three part set-up such as in the diagram of Figure 1.1 of an intake fan leading into the compression section, combustion chamber, and finally the exhaust. The amount of power that can be generated from the engine depends on the fuel-air mixture and temperature at which the fuel is burned. It is in the hot section where much of the complexities relating to material selection arise. The mixture of fuel and air that enters the turbine section is at high-pressure, high-velocity and high-temperature. Turbine components are subjected to high-temperature oxidation, hot corrosion, creep, high-cycle fatigue, and thermal fatigue. If even just one of these factors is neglected in the design of the section then a catastrophic failure of the entire engine can be expected.

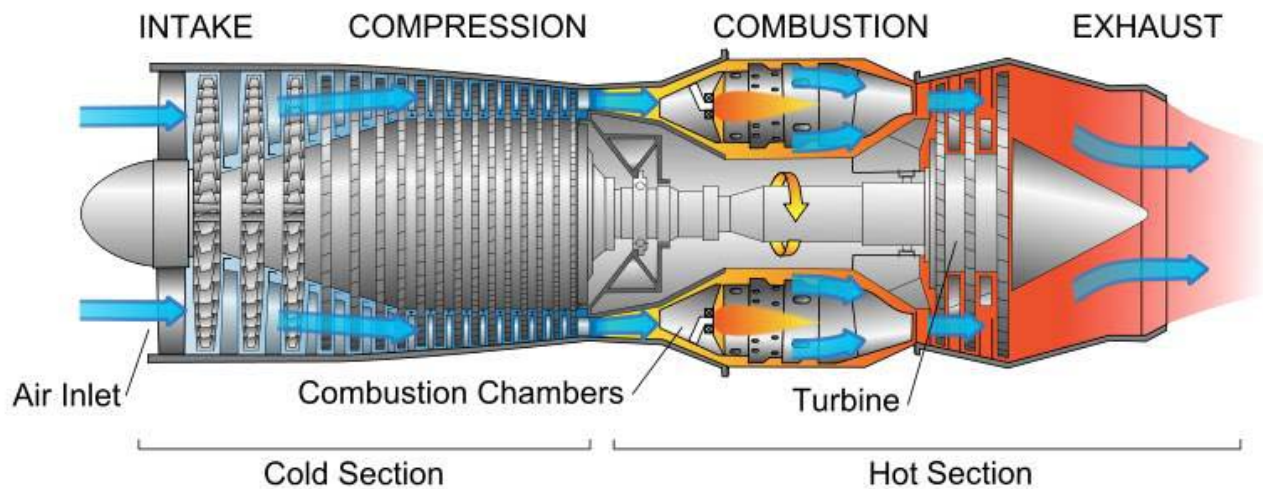


Figure 1.1: Diagram of a single stage turbine engine.

The trend of increasing temperature in various processes has necessitated the understanding of high-temperature corrosion for new alloy systems, their limitations at such temperatures, and the best directions for improvement. This is especially true for power or jet turbine engines wherein the blade section has been dominated by the use of Nickel base alloys. Advances in thermal barrier coatings,

manufacturing techniques and component design have allowed nickel based superalloys to operate within 200°C of their melting point. Increasing the maximum service temperature from 1150°C to 1300°C, would allow for a 50% gain in efficiency of the next generation jet engines [1]. However, with the Nickel based alloys, such an increase in temperature would cause the alloy system to enter a liquid-phase, prompting the research effort into new alloy systems.

Refractory metal based systems are attractive due to their high melting points, low densities, and good high temperature strength [2, 3]. The most focus has been placed on the systems of Mo and Nb both of which have melting points above 2500°C and when alloyed have desirable properties in creep resistance and toughness. The drawback of these two systems is their poor oxidation resistance at elevated temperatures limiting the use of such alloys. Research is being carried out to (a) develop an alloy capable of suppressing the catastrophic oxidation seen in the base materials and (b) be serviceable in the high-temperatures to be seen in turbo jet engines without additional protections.

Studies on the Nb-base systems have shown a gradual increase in oxidation resistance with increased boron content as the composition of the constituent phases are modified. Two of the alloys presented in this study have been subjected to a variety of exposure periods to determine some of the oxidation limits of the alloys. Such research is necessary to determine the next direction in which to pursue the goal of oxidation resistance for Nb-base alloys. The influence of high additions of boron has been shown to be beneficial to a limited extent in the modification of the constituent phases and the subsequent scales developed.

1.1 Justification

As will be indicated in the literature review there have been several studies to showing the improvement of oxidation of niobium based alloy systems with the addition of boron to the matrix. Results of initial studies for Nb-25Cr-20Mo-15Si-(10,15)B alloys indicate that the alloys have superior oxidation resistance to that of earlier systems, suggesting a need for further review into longer term

cycles Initial suspected benefits of the boron addition were thought to be limited to the creation of a layer of borosilicate glass, similar to that found in Mo-Si-B systems. The addition of boron at high concentrations has also had a positive impact on the microstructural characteristics of the alloys in question as it is related to the oxidation resistance. The combination of NbCr₂ Laves phase and mixed niobium/molybdenum silicides (Nb,Mo)₅Si₃ have provided improvements to high temperature oxidation.

The oxidation mechanisms of multi-phase Niobium alloys are not well understood under static air, which precludes testing in either moving air or the complex environment of an engine. In the interest of continuing development of this system the compositions were modified to begin investigation into the effects a lower molybdenum concentration would have in the oxidation resistance of the alloys at high temperatures. An initial investigation into the short-term (24 hour) oxidation behavior has been carried out to compare the behavior the three new alloys to previous compositions. Further periods of exposure reveal that the variance in composition has some beneficial effects in the mid- to high-temperature range, but not at 1400°C.

Chapter 2: Literature Review

The oxidation of a pure metal is a well understood process; however, the oxidation of alloys with multiple phases complicates this process based on a number of factors. After the determination that the silicide phases would be desirable from a mechanical standpoint, the focus of many studies have been to increase the oxidation resistance of such alloys. The various kinetics and mechanisms will be reviewed as part of the background to the work that has taken place. Niobium based alloys have undergone a number of studies in order to determine the balance of chemical and physical attributes needed for the use of such alloys in the aggressive environment of turbine engines. As will be apparent from the brief overview of the oxidation of pure niobium, lack of oxidation resistance is one of the most limiting factors for this system.

2.1 REFRACTORY METALS AND HIGH TEMPERATURE APPLICATIONS

The commonly designated refractory metals include niobium, molybdenum, tantalum, tungsten, and rhenium. Table 2.1 compares the basic properties for the refractory metals. In holding with a typical definition, a melting point higher than that of the setting point of iron (1539°C) is required for a metal to be considered a refractory. Stricter definitions put the cut off temperature at 2200°C and also require the metal to have a body centered cubic (BCC) structure.

Table 2.1: Basic properties of some refractory metals.

Element	Melting Point (°C)	Density (g/cm ³)	Elastic Modulus (GPa)
Niobium	2468	8.57	103
Molybdenum	2617	10.22	324
Tantalum	2996	16.654	185
Rhenium	3186	21.02	469
Tungsten	3410	19.25	400

The variety of properties that refractory metals host allow them to be used in a number of applications, some of the more common are as follows:

1. Alloying elements in steel and superalloys, especially as carbide formers
2. Use in specialized glasses, NbO has a particularly high refractive index
3. Lighting applications, with some early incandescent bulbs using Mo or T and fluorescent bulbs using Nb
4. The processing of sapphire requires high temperature capable (refractory metal) crucibles
5. Refractory metals present some superconducting properties useful in medical/radiation applications
6. Some refractory alloys are already used in aerospace applications, such as Nb C103 for rocket nozzles.

One of the challenges that faces when working with refractory materials is the need to evolve the processing procedures as the purity of available materials increases. This becomes obvious when a common property that defines these materials is their strong chemical reactivity, especially when exposed in oxygen containing environments. The tendency for these materials to spontaneously form strongly adherent and protective oxide films is a benefit in some areas of use, such as cathode/anodes [4]. The widest use of refractory metals is seen for Mo due to the ability to alloy for specific properties, either by strengthening through carbides, diffusion inhibition, or dispersed phases. Though Nb has the lowest density, the highest thermal expansion coefficient and is stable in a wide variety of normal and corrosive environments, its use is limited due to its ability to dissolve O₂ and form several oxides.

2.2 OXIDATION OF Nb AND Nb-BASED ALLOYS

As a refractory metal niobium has a high melting temperature at 2,469°C, among the refractory metals it has the lowest density and is the most ductile. However, despite the advantages of relatively

high strength and inherent heat resistance among others, the major drawback has been the low resistance to oxidation at moderate and high temperatures. Since the 1950s the alloying of niobium to produce oxidation resistance has been undertaken [5], but recent efforts have shown improvements though usually at the sacrifice of mechanical properties.

The most accepted behavior of niobium oxidation was presented by Kofstad [6], showing that the niobium lattice becomes saturated with oxygen to form the various oxides as temperature increased. The time needed for oxygen saturation within the lattice decreases after 500°C with NbO and NbO₂ forming along grain boundaries once 600°C is reached. Further temperature increases will cause the NbO₂ to form Nb₂O₅ at 650°C. The rapid oxidation of NbO₂ to form non-protective Nb₂O₅ above 700°C is noted to correspond to a maximum linear rate constant. In the interest of the high temperature study, the polymorphs of Nb₂O₅ become increasingly important [7]. The low temperature variant of the oxide takes an orthorhombic structure and mid-range temperatures demonstrate a base-centered monoclinic lattice that has been noted to be the cause of bulky catastrophic oxidation in several studies, at high temperatures the monoclinic lattice is stabilized.

To mitigate the oxidation that is inherent to the pure system the goal is often to reduce the prevalence of the detrimental Nb₂O₅ oxide. Various alloying elements have been added to the system in order to either adjust the primary oxides that are formed or to attempt to develop protective layers to prevent oxygen diffusion to the base material. Some success with the alloying of Cr has been found in the development of the Cr₂Nb Laves phase. The oxide formed from this phase is that of CrNbO₄ which is more protective than the niobium oxides. The protection afforded by the CrNbO₄ is limited to at most 500 hours at 1100°C due to the volatilization of Cr₂O₃ that forms alongside it [8].

In the interest of forming a protective layer the most desirable oxide is that of SiO₂ for its low oxygen permeability. Such successes in Mo-Si-B based alloys is promising [9, 10], though dependant on the volatile MoO₃. In the cyclic oxidation of Nb-base in situ composites it has been found that in

order to achieve a continuous SiO_2 layer that the silicides in the alloy must exceed 34% volume percent [11]. To obtain the protection of the SiO_2 in Nb-base alloys is difficult to achieve due to the non-volatile nature of Nb_2O_5 that forms in conjunction with SiO_2 during silicide oxidation.

2.3 DEVELOPMENT OF THE Nb-Cr-Mo-Si-B SYSTEM

The development map of the Nb-Cr-Mo-Si-B alloy system is available in Figure 2.4. Previous studies in the Nb-Cr-Mo-Si-B system have shown that improvement over non-boron containing alloys can be achieved with up to 15B concentration. Initial studies in this system included those by Ventura with the Nb-20Cr-20Mo-15Si-5B alloy [12]. Ventura showed that after the alloy was subjected to oxidation in air in the temperature range of 700 to 1300°C the alloy tended to show a thin powdery scale at low temperatures (700 and 800°C) while at 900 and 1000°C a thin scale was developed. At temperatures 1100°C and above the scale is bulky and contained a large amount of Nb_2O_5 in conjunction with CrNbO_4 in a SiO_2 matrix. The chromium content of the alloy was increased to 25 at.%, which was noted as an upper limit before complications were introduced into the casting procedure in an alternate study [13].

The evaluation of the effect of small boron additions in the alloy was examined against a non-boron containing alloy [14], such that the results of study were an increased resistance to oxidation at high temperatures with small concentrations. Portillo's short term oxidation study found that the scale was dominated by Nb_2O_5 at low temperatures with porosity due to the vaporization of MoO_3 . The study was also the first in this series of alloys to show the development of an intermediate oxidation layer in the boron containing alloy at temperatures 1000°C and above. This preliminary study predicated the investigation of three alloys of this research with the intent to investigate the effects of reducing the presence of the solid solution through Mo content modification and to promote borosilicate formation through B/Si ratio modifications.

The Nb-25Cr-20Mo-15Si-10B alloy was one of three Mo-modified alloys studied initially by Portillo [15]. Of the three alloys, the 10B preformed the best in the short term oxidation experiment with discontinuous scales formed below 900°C and a scale of CrNbO₄, Nb₂O₅, and SiO₂ at 1000°C and above. The 10B alloy was the only of the three to be subjected to the week-long cyclic oxidation at 700°C as the alternate compositions suffered catastrophic pest oxidation after 24 hours exposure. The increase in boron content showed the best response in the cyclic study across all temperatures. Despite the relatively high boron content, the presence of a borosilicate layer could not be established prompting the increase in Boron content to 15 at.% in Rangel's work [16]. In both the short and long term oxidation the 15B preformed similarly with only a slight increase in resistance. However, low temperature pesting was suppressed. The survival of the samples after one week prompted the question of the length of time the alloy could survive at high temperatures.

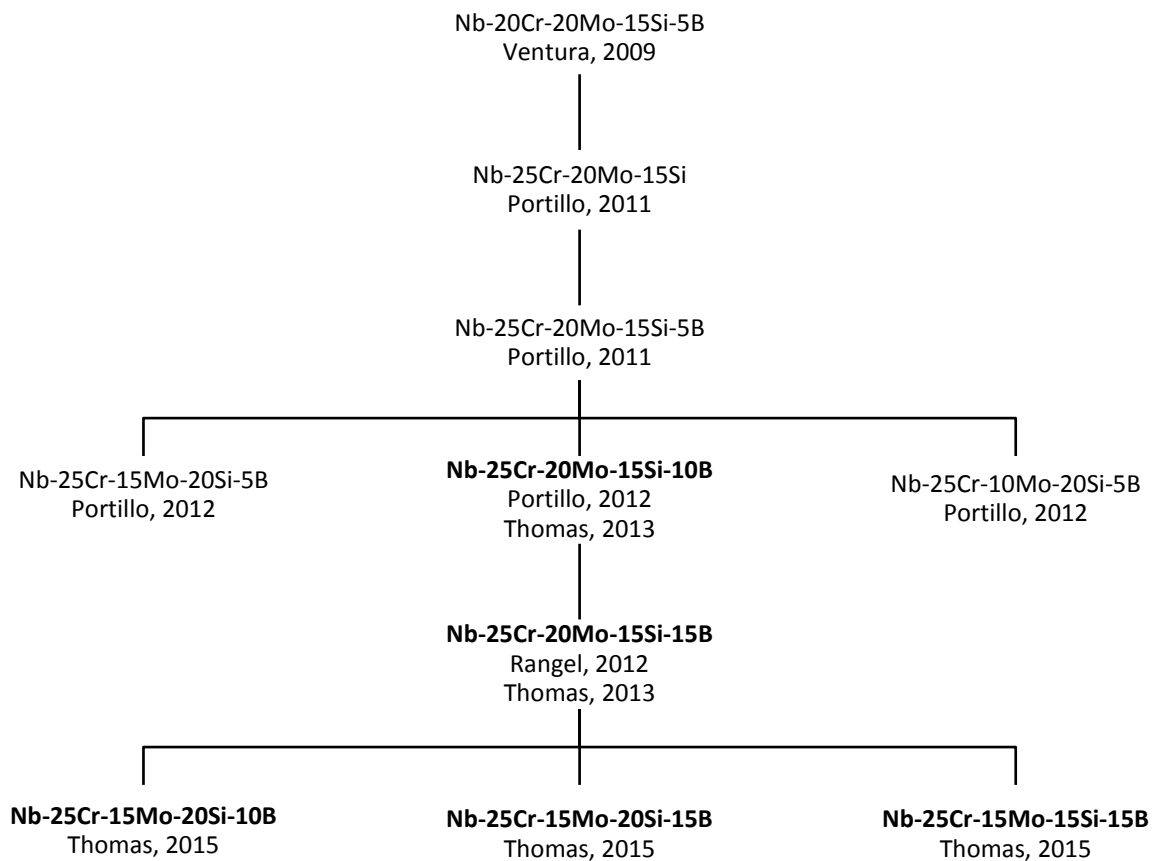


Figure 2.1: Alloy development map, bolded compositions are those utilized in this study.

2.4 ALLOY PHASES

The properties and general information of the pure components of the alloy are listed in Table 2.3. The three primary components of the alloy, Niobium (Nb), Chromium (Cr) and Molybdenum (Mo) are all refractory metals due to their high melting points. The other two components, Silicon (Si) and Boron (B) are commonly recognized as metalloids.

Table 2.2: Selected properties [17] of the pure components of the alloys under investigation.

Element	Symbol	Atomic Weight (amu)	Atomic Radius (nm)	Density of solid, 20°C (g·cm ⁻³)	Crystal Structure (at 20°C)	Melting Point (°C)
Niobium	Nb	92.91	0.143	8.57	BCC	2468
Chromium	Cr	52.00	0.125	7.19	BCC	1875
Molybdenum	Mo	95.94	0.136	10.22	BCC	2617
Silicon	Si	28.09	0.118	2.329	Dia. Cub.	1412
Boron	B	10.81	0.085	2.34	Rhomb.	2300

The Laves phase is one of the most common intermetallic compounds with over 360 binary combinations of the approximate AB₂ formula and is a topologically close-packed system [18]. In both the current alloy system and in the Ni-base superalloys the use of Cr is mainly for the improvement of oxidation resistance. The Nb-Cr system contains two eutectics bounding a congruently melting intermetallic—the NbCr₂ Laves phase—which has a low temperature and high temperature form. Intermetallic compounds have some of the lowest diffusion coefficients and the highest activation energy for diffusion to occur. In the interest of the Nb-Cr-Mo-Si-B alloy system the focus is on the NbCr₂ Laves phase which commonly includes two of the three polytypes. The low temperature C15 cubic structure with space group *Fd3m* has the prototype structure of Cu₂Mg. The high temperature C14 phase has a hexagonal structure with space group *P6₃/mmc*, prototype structure MgZn₂. The NbCr₂ Laves phase has a relatively low density (7.7 g/cm³), high melting temperature (1770°C), and good mechanical properties at high temperatures, maintaining strength and creep resistance [19, 20]. Finally,

there is the C36 structure, with the MgNi_2 structure. The three polytypes and the arrangement of A and B atoms are shown in Figure 2.2 with the tetrahedrons formed by the B atoms detailed in Figure 2.3.

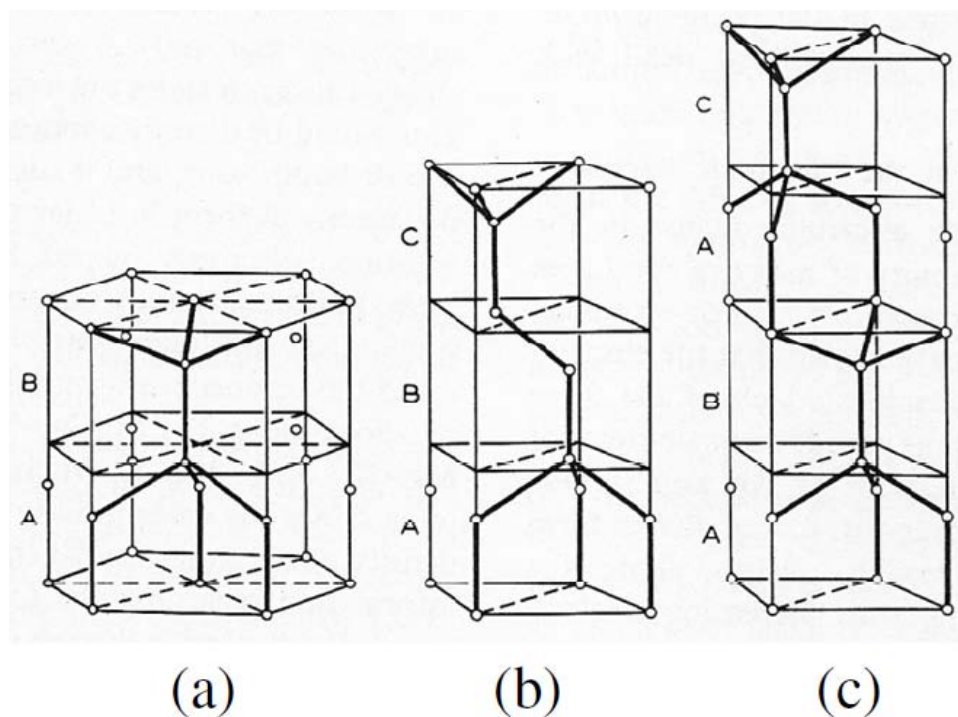


Figure 2.2: The three lattice arrangements for the Laves phase (a) C14, (b) C15, and (c) C36, adopted from [21].

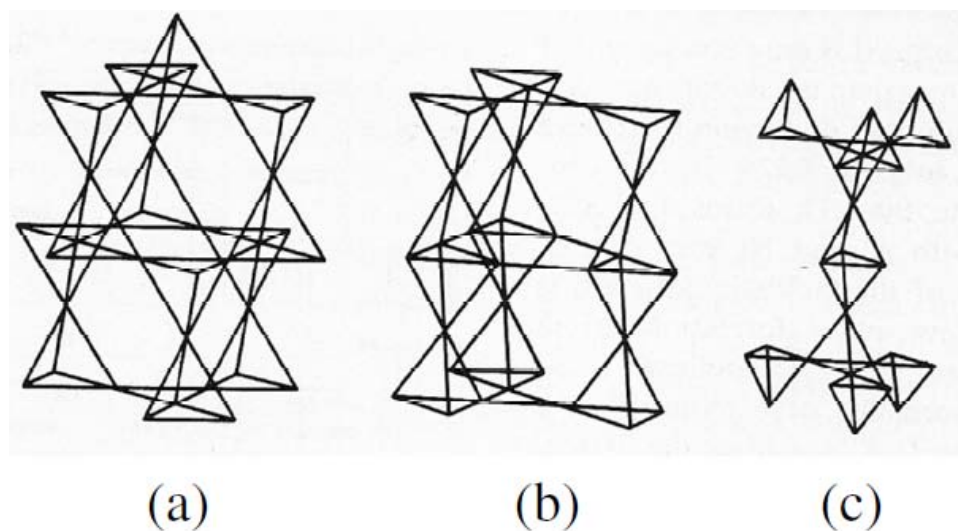


Figure 2.3: Tetrahedron formed by the B atoms in the three lattice arrangements for the Laves phase (a) C14, (b) C15, and (c) C36, adopted from [21].

While the oxidation resistance afforded by the addition of the Laves phase is desirable, the downside is that the phase retains low temperature brittleness. The effects of adding molybdenum to the Laves phase include the formation of a dual C14-C15 containing alloy with improved high-temperature deformation capabilities [22]. It may be possible to say that the same deformation capabilities would occur with a Mo-modified C14 phase. The amount of silicon needed to stabilize the C14 structure below the transformation temperature of 1585°C can range from 6 to 26 percent [23] without the phase becoming the ternary CrNbSi phase. It has been reported in several studies [11, 24] that the inclusion of the Laves phase increases the oxidation resistance of the alloy. The solubility of Cr in the α -Nb₅Si₃ is 10–12%, and it can substitute for Nb in the lattice of β -Nb₅Si₃ to form Nb₃Cr₂Si₃ at high temperatures [25, 26]. Even though the complex crystal structure of Laves phase helps to enhance the oxidation and creep resistance, the outward diffusion of chromium at higher temperatures presents a problem [27].

From the various binary systems there are a few noteworthy observations. In the Cr-Mo systems there exists a continuous solid solution at high temperature, however in the Cr-Mo system it has been suggested that a solid miscibility gap exists at temperatures below 860°C [28]. The Mo-Si and Nb-Si systems are similar, there exist several intermetallic phases which can improve the mechanical behavior of the alloys when they are present, these silicides have been the focus of several studies [9, 29]. Both systems include a 5-3 silicide which is of interest in the development of Nb-base or Mo-base refractory metal alloys. The melting temperatures of the silicide phase are notably higher than that of the Laves phase with Nb₅Si₃ at 2526°C and Mo₅Si₃ at approximately 2180°C. Due in part to their similar atomic sizes and complete solid solubility [30] the Nb and Mo atoms can replace each other in the respective silicides with no limitation. In the interest of this study the preferred silicide is that of the high temperature β -Nb₅Si₃. In the pure transformation of β -Nb₅Si₃ to α -Nb₅Si₃ involves a contraction of the lattice from the initial D8₁ structure (space group I4/mcm, Cr₅B₃ type) with lattice parameters a=0.652 to c=1.1884 to the D8₈ structure (I4/mcm, W₅Si₃ type) with lattice parameters a=1.0018 and c=0.5072.

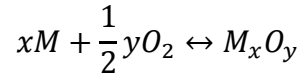
While slow transformations of $\beta\text{-Nb}_5\text{Si}_3$ to $\alpha\text{-Nb}_5\text{Si}_3$ that occur at high temperatures can allow the presence of the later phase at room temperature the substitution of Mo into the Nb_5Si_3 lattice to form $(\text{Nb}, \text{Mo})_5\text{Si}_3$ has the benefit of stabilizing the $\beta\text{-Nb}_5\text{Si}_3$ phase [31, 32] by creating chains of Si-Mo-Si which have much stronger bonds than Si-Si bonds. The $\beta\text{-Nb}_5\text{Si}_3$ compound is stabilized to room temperature through the substitution of the alloying element Molybdenum (Mo) within the $\alpha\text{-Nb}_5\text{Si}_3$ lattice. In the application of such phases at high temperatures the effects of thermal expansion must be taken into account, in the case of the Mo_5Si_3 there is a large anisotropy in the coefficients of thermal expansion (CTE) along it's a and c axis. The magnitude of anisotropy can be reduced [33] with the introduction of Nb into the Mo_5Si_3 lattice such that microcracking is reduced when the material is heated. The increase in Mo also improves the sinterability of the oxide [34], reducing the rate of diffusion of oxygen to the base metal. Some Nb-Mo-Si-B alloys [35] indicate the formation of non-protective layers of Nb_2O_5 and SiO_2 , along with an intermediate oxidation layer similar to the initial Nb-Cr-Mo-Si-B research [14]. The $\text{Nb}_{55}\text{-Nb}_5\text{Si}_3$ combination adds structural benefits while the silicide forms a non-volatile Nb_2O_5 oxide that can be present in a SiO_2 matrix.

In regards to boron, while initially added to the Nb-Cr-Mo-Si system to affect the viscosity of the developed SiO_2 as seen in Mo-Si-B alloys, it has rather increased oxidation through suppressing the formation of the solid solution and eliminating it completely at high contents (10-15 at.%) [15]. While the elimination of the solid solution has improved oxidation of the alloy, it increases room temperature brittleness. The $\alpha\text{-Nb}_5\text{Si}_3$ has a large solubility of boron [36], between 11 and 26 at.%, ranging from the pure Nb_5Si_3 to near the stoichiometry of Nb_5SiB_2 and solubility in the high-temperature phase is assumed to be similar. The Mo_5Si_3 is expected to have a comparatively low solubility (~5 at%) according to some studies [37]. The addition of boron can create either the T_1 $(\text{Nb}, \text{Mo})_5\text{Si}_3\text{B}_x$ or T_2 phase $(\text{Nb}, \text{Mo})_5\text{SiB}_2$ and at higher concentrations the $D8_8$ phase of $(\text{Nb}, \text{Mo})_5\text{Si}_3\text{B}_x$. No boride phases are expected in the alloys for the boron contents studied.

The solid solution of niobium as previously discussed is very susceptible to pest oxidation after 500°C. However, it is desirable from a mechanical standpoint as a ductile phase. Isothermal studies up to 100 hrs for several developmental Nb-base alloys have found large weight gains with a strong dependence of the volume fraction of the Nb_{SS} [38, 29]. In multiphase alloys the solid solution is preferentially attacked to form un-protective Nb₂O₅ [14]. Likewise the percentage of the α -Mo structure needs to remain low in order to provide oxidation resistance as the phase tends to oxidize rapidly into volatile MoO₃.

2.5 OXIDATION MECHANISMS AND KINETICS

The oxidation of metals is a corrosion process that takes place at room temperature for all metals or alloys. As the temperature of the system is raised the rate of the reaction will increase rapidly to the point where only a few minutes are required to come to completion. Under equilibrium conditions the oxide-metal reaction is highly likely to occur and therefore the focus turns to determining the rates of a reaction. The basic chemical formula for the oxidation reaction is:



The driving force, ΔG , or Gibbs free energy change for the reactions to occur can be calculated using the chemical activity (a) of the reactants and products from the chemical equation such that:

$$\Delta G = \Delta G^\circ + RT \ln \left(\frac{a_{M_xO_y}}{(a_M)^x (a_{O_2})^{\frac{y}{2}}} \right)$$

Where ΔG° is the standard free energy, R is the gas constant, and T is the absolute temperature of the system. If $\Delta G < 0$ the reaction will occur spontaneously, if $\Delta G = 0$ the system is in equilibrium, and if $\Delta G > 0$ the reaction is thermodynamically unfavorable. It is generally assumed that the activities of the

metals and the oxide are equal to 1 and the partial pressure of oxygen (p_{O_2}) can be substituted for the activity of oxygen allowing the equilibrium equation to be written as:

$$\Delta G = RT \ln p_{O_2}$$

$$p_{O_2} = \exp\left(\frac{G}{RT}\right)$$

Resources such as the Ellingham diagram can be useful in determining which reaction is more favorable even if the diagrams generally only involve the oxidation of pure elements. For alloy systems the activity of the element under consideration is reduced and the associated free energy of the reaction will change, which precludes a change in the necessary partial pressure of oxygen required for the reaction.

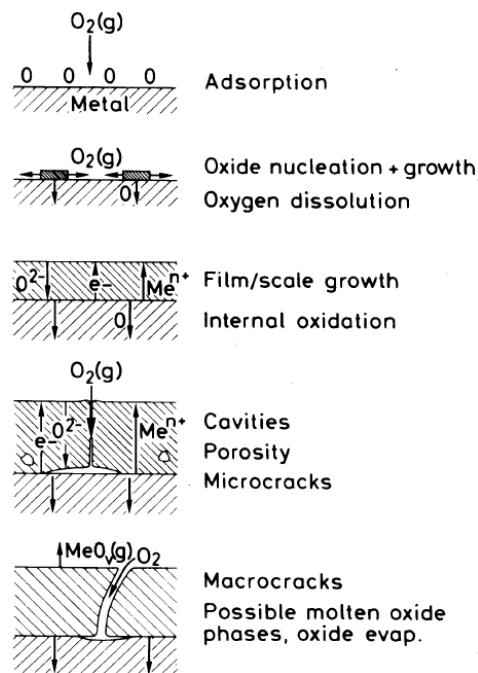


Figure 2.4: The adapted metal-oxygen reaction schematic [6].

The gas-solid reaction occurs in several steps as Kofstad proposed and is illustrated in Figure 2.4. The oxygen within the atmosphere is first adsorbed on the metal surface. Oxide nuclei develop on the surface grow laterally across the surface in thermodynamically favorable locations. As the film develops, the diffusion of oxygen proceeds through the scale unless a barrier to the penetration is

developed, some classic examples of barrier or passive oxides are Cr_2O_3 , Al_2O_3 , and SiO_2 . The oxygen penetration into the base metal can develop internal oxidation if the activation energies of the metal components are low enough. Concurrently the metal ions will diffuse towards the surface of the developing scale, during this period they may combine with the inwardly diffusing oxygen. The oxides that are formed in this period may be stable or may volatilize to form internal pores within the scale. The stresses developed in the scale by either differences in coefficients of thermal expansion between oxides or the oxide-metal interface and the pressure exerted by gas filled pores can cause cracking in the scale yielding a path for direct interaction between the atmospheric oxygen and the heated metal surface.

As a general rule of thumb that can determine whether the oxide will be protective or not is the Pilling-Bedworth Ratio. The ratio compares the atomic weight and density of the oxide to the substrate which can be simplified to a comparison of the volumes.

$$PB \text{ Ratio} = \frac{A_o \cdot \rho_m}{n \cdot A_m \cdot \rho_o} = \frac{V_m}{V_o}$$

The Pilling-Bedworth ratio for a protective oxide is approximately 1. For values less than one a porous scale is developed and for those that exceed a value of 2 the oxide will flake away, or spall off. The consideration of the volumes of the substrate and the oxide lead to the need for similar coefficients of thermal expansion which would prevent large changes in volume to cause stress formation at interfaces.

To describe the behavior of alloy oxidation there are three rate laws that can be described: linear, parabolic, and logarithmic. A schematic of the behaviors has been adopted in Figure 2.5 to detail the differences in behaviors graphically.

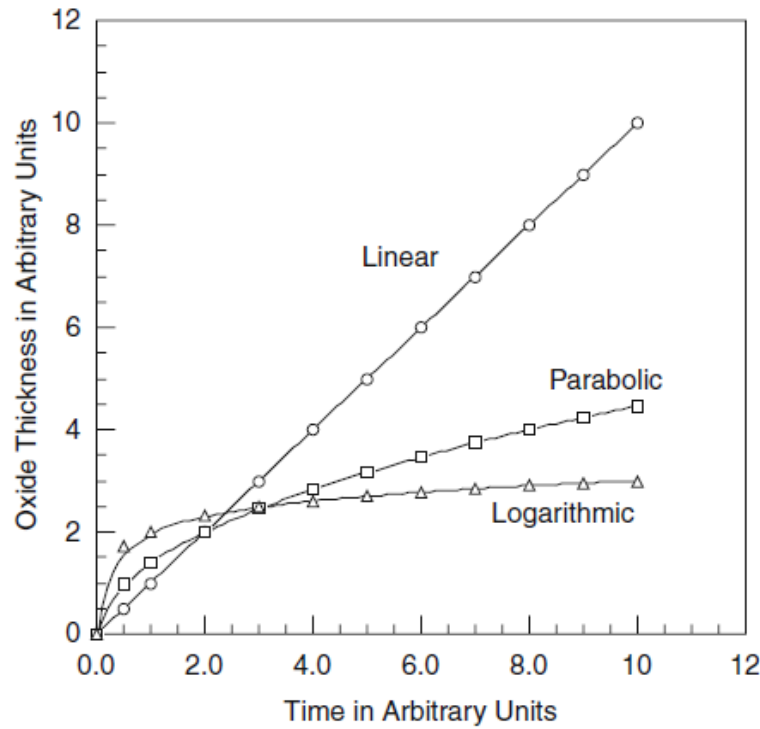


Figure 2.5: Adapted graphical representation of the three rate laws in arbitrary units [39].

If an oxide follows the linear rate law of behavior, the scale is considered un-protective as this suggests continuous contact between the substrate and the reactant (air) through either cracks or pores in the film. The rate of oxidation is constant and is related to the thickness of the oxide versus the time of exposure such that:

$$\frac{dx}{dt} = k$$

The integration of the equation results in the simple linear equation:

$$x = kt + \text{const}$$

The constant can be calculated from experiments, where a clean surface will have $x=0$ at $t=0$. If the thickness is changed to weight through the oxide density, the equation has the same form:

$$w = k't + \text{const}$$

$$k' = k\rho_o$$

The parabolic behavior can be described as the mechanism during which oxygen diffusion to the substrate is reduced as the oxide layer increases or more simply as the scale thickness increases the oxidation rate decreases. The equation to describe this behavior is given:

$$\frac{dx}{dt} = \frac{k'_p}{x}$$

Where k'_p is the parabolic constant, the equation can be integrated such that:

$$x^2 = \frac{k'_p}{2} + \text{const}$$

Where x is the thickness of the oxide and t is the time of oxidation. This is the rate law that corresponds to the development of protective oxides and suggests that the controlling method is through the diffusion of ions/electrons through the scale.

For very thin scales ($x \leq 1,000\text{\AA}$) or at lower temperatures the logarithmic rate law is utilized to describe oxidation.

$$x = k'' \log (ct + 1)$$

Where k'' is the logarithmic constant, c is determined through experimental data, and t is the time of oxidation. In this case it is generally thought that the rate is controlled by electron transfer across the film.

In addition to the energy of formation the oxidation rate constant is also temperature dependant, following an Arrhenius-type equation:

$$k = k_o \exp\left(\frac{Q}{RT}\right)$$

However, simply the change in activation energy is not sufficient to explain the change in oxidation mechanisms, as other time/temperature mechanisms may be involved, such as self-diffusion of ions within the oxide scale.

As can be gathered from the requirement of different laws to explain general behavior, there are many considerations involved to completely describe oxidation mechanisms in alloys. The complexities of alloy oxidation stem from a variety of topics, such as the differing activation energy of the elements, various diffusivities of the alloying elements, and the existence of ternary or complex oxide, to name a few. There have been several models proposed for alloy oxidation and in the case of single-phase alloys Wagner's model has sufficed. However, for multi-phase alloys there must be some extension of the theory. Theoretical studies [40, 41, 42, 43] have focused on the treatment of an alloy consisting of two phases, an oxide forming element M rich matrix and an M rich precipitate. Gesmundo *et al.* summarized the findings and presented the various forms that the corrosion of two-phase alloys may take according to the findings presented as a schematic in **Error! Reference source not found..6**.

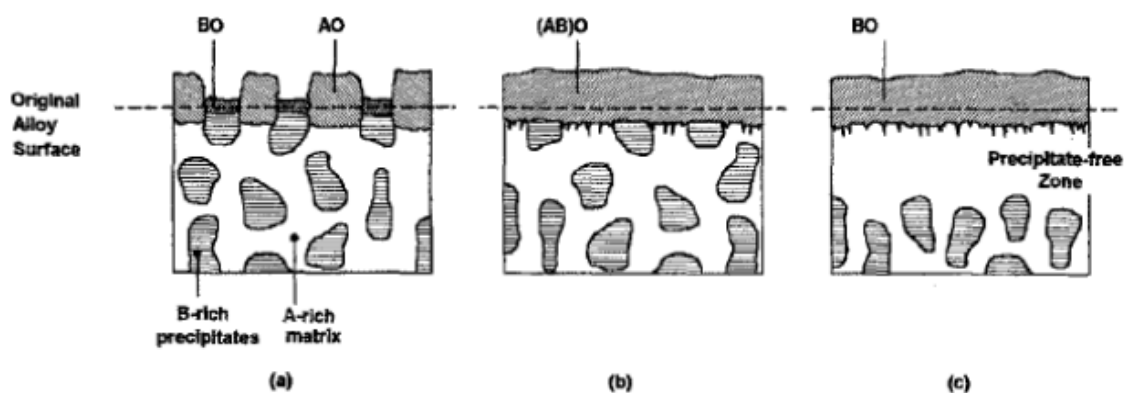


Figure 2.6: Oxidation behavior observed in two phase alloys (a) independent oxidation forming a non-uniform scale, (b) cooperative oxidation forming a uniform scale, and (c) solute rich phase acts a reservoir for growth of solute scale [43].

2.6 OXIDE VOLATILIZATION

The tendency for oxide volatilization becomes an increasingly important consideration as the temperature of a system is raised. In the case of the niobium based systems this is especially important for the additions of Molybdenum as it is reported to lower the anion vacancies in Nb_2O_5 which slows oxygen diffusion and would promote a more protective scale to be developed. Below 550°C Mo oxidation is dominated by $\text{MoO}_2(\text{OH})_2$ in small concentrations of water vapor, then MoO_3 oxide begins

to sublime to a negligible extent at 550°C and is completely volatile above 800°C [44]. The volatilization of MoO₃ is a necessary component in Mo-Si-B alloys to develop a protective layer of SiO₂, however the material loss associated with such a development may not be desirable [45].

Consideration for the volatilization of chromium oxide is also needed as it is believed to be necessary to the formation of CrNbO₄, whereby the binary oxides Nb₂O₅ and Cr₂O₃ calcine [46] together to form the rutile structure that is more protective than pure Nb₂O₅. The presence of Cr₂O₃ at the surface of a scale is unlikely as the chromia typically evaporates as CrO₃ at temperatures above 1000°C and near atmospheric oxygen partial pressure [47, 48]. It is possible that the presence of other oxides on top of a Cr₂O₃ layer may inhibit evaporative losses. The formation of chromia within the scale may be beneficial as it is a protective oxide.

The addition of boron to the alloy system intended for the modification of the silicate to a borosilicate for purposes of creating a protective layer also introduces B₂O₃ volatilization which can begin at temperatures above 1100°C. Boron volatilization could instead lead to near pure SiO₂ formation rather than a borosilicate in the highest temperature regimes [49].

Chapter 3: Experimental Methods

3.1 SAMPLE PREPARATION

The Ames Laboratory of Iowa State University fabricated the alloys through an arc-melt process under a high purity argon atmosphere in a water cooled copper crucible. Component materials were of 99.9% purity for niobium, molybdenum and chromium; silicon and boron had starting purities of 99.5%. Alloys were cast into 50 gram buttons that were re-melted several times to ensure homogeneity. Samples were cut from the buttons through electronic discharge machining (EDM) into 5x5x5 mm cubes. The samples were not subjected to hot isostatic pressing during fabrication. The compositions of the alloys used in this study in both atomic and weight percent are listed in Table 3.1 along with their designation by which they are referred to throughout the study.

Table 3.1: The compositions of the experimental alloys with the weight percent given as indicated by Ames Lab.

Alloy	Composition (at. %)					Composition (wt. %)				
	Nb	Cr	Mo	Si	B	Nb	Cr	Mo	Si	B
10B	30	25	20	15	10	42.648	19.8905	29.361	6.446	1.654
15B	25	25	20	15	15	37.9221	21.2236	31.3283	6.8783	2.6477
1515	30	25	15	15	15	45.6196	21.2762	23.5546	6.8954	2.6542
2010	30	25	15	20	10	40.5247	22.68	25.1087	9.8004	1.8862
2015	25	25	15	20	15	40.146	22.4681	24.8741	9.7089	2.8029

3.2 GIBBS FREE ENERGY MODELING

The software PandatTM [50], developed by CompuTherm, LLC., is a thermodynamic modeling software that utilizes Gibbs free energy curves to develop multi-component phase diagrams. The program is also capable of quantitative analysis of phase composition and calculating phase volume fractions. The program was utilized to develop isothermal sections for each temperature of the investigation (700-1400°C) and a room temperature (25°C) diagram. The psedu-ternary diagrams were

developed by keeping the chromium content constant at 25 atomic percent. Boron is not modeled in the diagrams due to database limitations, discrepancies between the calculated diagrams and the actual microstructures seen in the samples are discussed later.

3.3 OXIDATION

Oxidation was carried out in standard lab air in a range of temperatures from 700 to 1400°C in one hundred degree increments. Furnaces were computer controlled with a ramp rate of 10°/min and all samples were furnace cooled. Samples were weighed after cooling. Four oxidation tests were carried out: Short Term Static Oxidation, Long Term Cyclic Oxidation, Long Term Static Oxidation and Oxide Initiation.

Short term static oxidation involved ramping to the specified temperature and an isothermal hold at temperature for 24hrs. Long term cyclic oxidation (LTO) involved a similar process to the STO experiment, this was then repeated for 7 and 14 cycles. Long term static oxidation (LTS) involved ramping the sample to temperature followed by isothermal holding for 1, 3, 6, 7, 9, 12, and 14 days for the 10B and 15B alloys and 7 days for the 1515, 2010, and 2015 alloys. Oxide initiation or initial oxide scale development experiment was carried out for the 1515, 2010, and 2015 alloys. Half-size samples (5x5x2.5 mm³) were heated in the crucibles to designated temperatures and held for 15 minutes. Samples were then removed from the furnace to air quench in order to maintain the high temperature structures developed.

The initial kinetics of oxidation for select samples was characterized through thermo gravimetric studies carried out in a LabSys evo. Half-sized samples (2.5x5x5mm) were obtained through sectioning the as-received samples. Samples were then placed in an alumina lined crucible and placed into the furnace. Samples were exposed for 4 hours at temperatures 700, 900, 1100, and 1300°C to obtain the kinetics at the start of oxidation.

3.4 X-RAY DIFFRACTION

Samples were characterized by X-ray Diffraction (XRD) in a Bruker D8 Discovery using CuK α radiation ($\lambda=1.5406\text{\AA}$). The parameters for the scans included a $5^\circ/\text{min}$ scan rate, 0.05 measurement increments, use of the 0.2mm slit on the x-ray source, and 8mm slit on the detector. Analysis was taken for the as-cast alloys after removal of the surface markings due to the machining process in order to confirm the phases present. After oxidation, scans were performed on the surface of the resultant oxide scales as removal of the scale without damage to the base metal was not possible. The patterns obtained were characterized by comparison with the ICDD card database.

3.5 SCANNING ELECTRON MICROSCOPY

Scanning electron microscope (SEM) examination was carried out in a Hitachi S-4800 UHR FE-SEM with secondary electron (SE) and backscatter electron (BSE) capabilities. Standard operating parameters during SEM analysis include an accelerating voltage of 15-20kV with a probe current of 15-20 μA and a working distance of $15\text{mm}\pm 2\text{mm}$. Samples were attached to the SEM holder with either double sided copper tape or graphite tape with a piece extending from the sample to prevent charging. As cast samples were mounted in an epoxy resin and polished to a 1200 grit finish to obtain initial microstructure. Oxidized samples were mounted and sectioned prior to polishing to a 1200 grit finish in order to view the cross section of the oxide-metal interface. Samples were coated with a thin layer of gold in a Gatan Precision Etching Coating System (Model 682) prior to SEM observation. The BSE mode was utilized for the phase contrast due to the different atomic weights for the phases, thereby removing the necessity for etching. An EDAX detector was utilized for Energy Dispersive X-Ray Spectroscopy (EDS) and x-ray mapping. The EDS analysis was performed to give a rough quantification of the elemental distribution within the phases. Due to inherent accuracy limitations within the EDAX detector, where sensitivity to atomic numbers below oxygen ($Z=8$) is poor, the quantification of the

amount of boron within specific phases is not possible. Boron detection within the alloy microstructure and associated oxides is taken on a qualitative basis.

3.6 IMAGE ANALYSIS

After sectioning and polishing the oxide samples, the un-oxidized metal remaining for the samples was estimated by comparing the resultant cross-sectional area of the metal to the original cross-sectional area of the samples. In order to determine the phase fractions of the two alloys image analysis was carried out on the as cast microstructures to determine the phase fractions. Calculations are based on the contrast of each phase present in the as-cast condition at 1000x magnification of backscatter imaging.

Chapter 4: Results and Discussion

The modeling and experimental microstructures of the as-cast state of the alloys are presented, differences between the two are analyzed. The initial studies for the alloys focused on the limits of oxidation resistance the Nb-25Cr-20Mo-15Si-(10,15)B could sustain under continuous oxidation. Modification to the composition of the alloy to investigate an increase in the silicon content to promote SiO_2 formation was attempted.

4.1 ISOTHERMAL MODELING OF THE Nb-Cr-Mo-Si SYSTEM

The isothermal sections for the pseudo-ternary Nb-25Cr-Mo-Si System at selected temperatures are calculated using the thermodynamic modeling software PandatTM. As mentioned in Chapter 3, the diagrams do not show the effect of Boron on the equilibrium phases. The room temperature (25°C) diagram is presented in Figure 4.1 with the different alloy compositions indicated along with the calculated equilibrium phases that should be present. Nearest neighboring phase fields are also labeled with expected phases. The isothermal section suggests that under equilibrium cooling conditions the 10B and 15B alloys should obtain a three-component microstructure consisting of a ternary CrNbSi [T3] phase, a solid solution, and the NbCr_2 Laves phase with a C14 structure at room temperature. The 1515, 2010, and 2015 alloys should obtain a similar microstructure with the addition of a second ternary phase, CrNbSi [T3]. However, due to the non-equilibrium cooling inherent in the arc-melt process of casting the alloys, these equilibrium structures are not possible unless secondary heat treatments are carried out at low temperatures ($T > 500^\circ\text{C}$) the time of which to complete is unfeasible for industry practices. To obtain the equilibrium microstructures would require extensive heat treatment ranging in excess of 100 hours at temperature [51]. Due to its high reactivity in air, niobium must be annealed in either a vacuum or inert atmosphere in order to prevent oxidation in these processes.

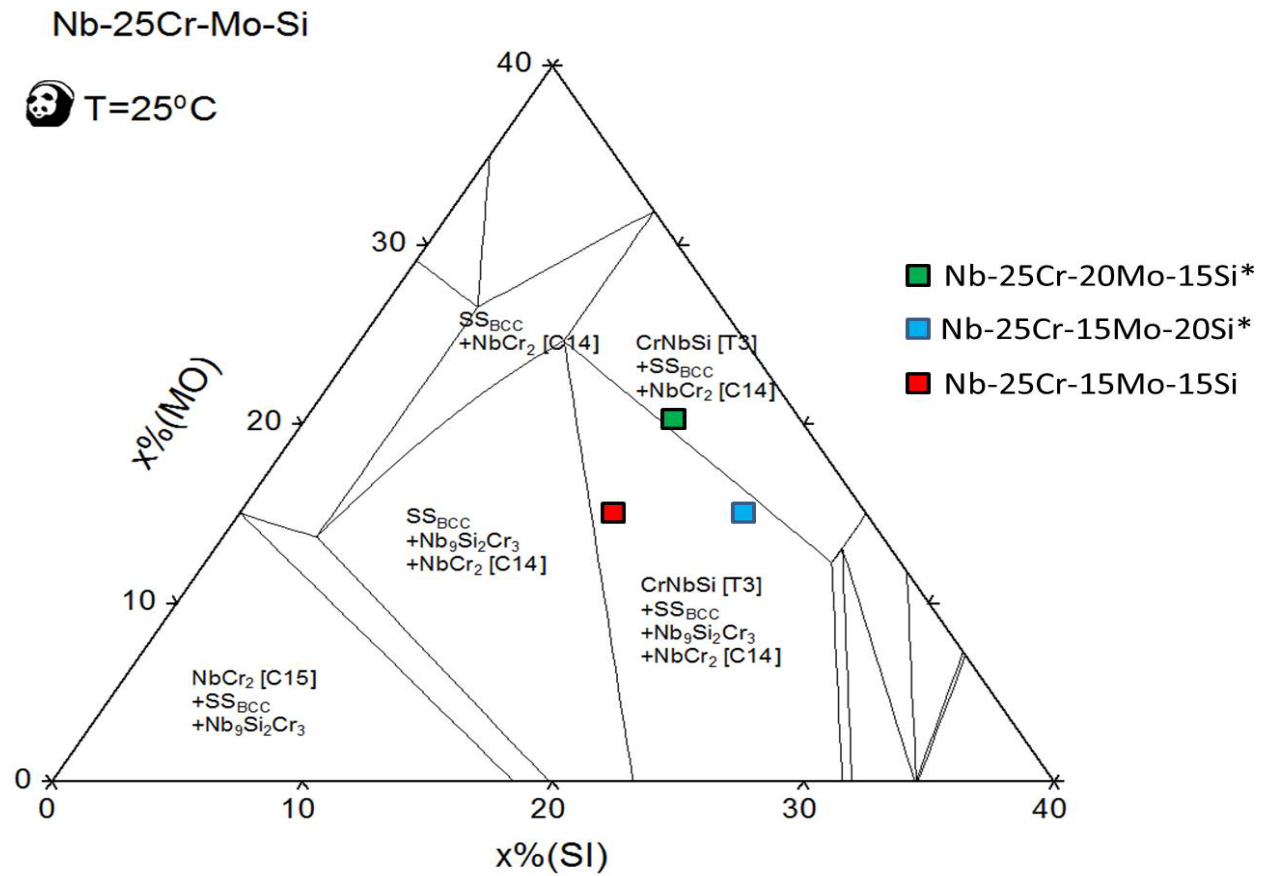


Figure 4.1: The Nb-rich portion of the isothermal section calculated at room temperature (25°C) for the Nb-Cr-Mo-Si System, where * indicates for both 10 and 15% B concentrations.

Isothermal sections were calculated for all the temperatures at which the alloys have been exposed, selected diagrams are presented in Figure 4.2. For the 10B, 15B and 1515 alloys the diagrams suggest that the equilibrium structure the alloys will remain in a three phase region containing the solid solution, Nb_5Si_3 , and NbCr_2 Laves phase with the C14 structure. The 2010 and 2015 alloys remain in the same phase region up to 1300°C after which the alloys enter a four-phase region containing an additional Mo_5Si_3 .

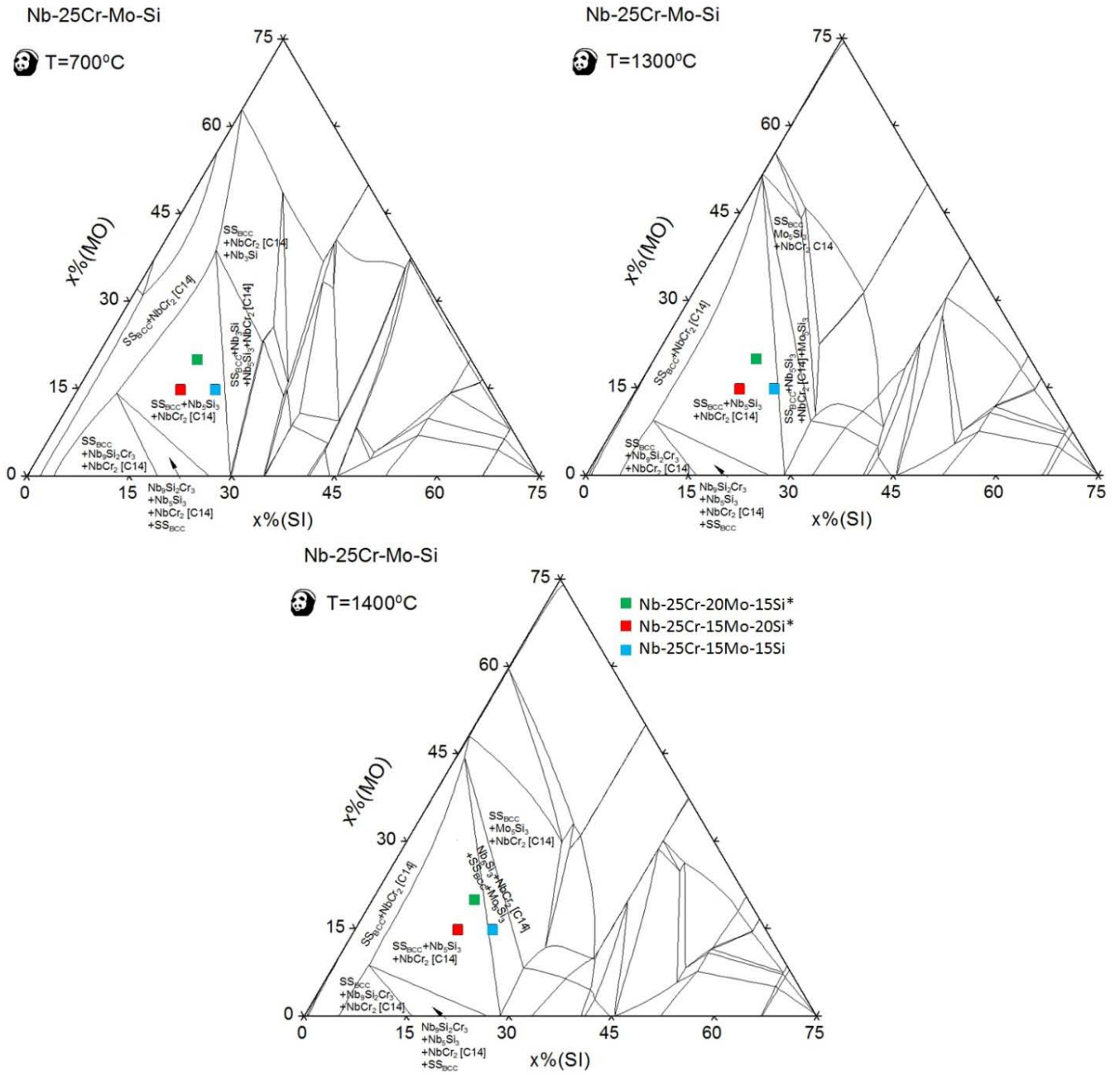


Figure 4.2: Isothermal sections for the Nb-25Cr-Mo-Si system at selected temperatures to model the phase changes expected in the system.

The phase fraction data is developed for each alloy to show the presence of any transformations during cooling, the simulations are presented in Figure 4.3. The simulations show similarities in the phases formed from the liquid state: initially Mo_5Si_3 is formed followed by the solid solution. As the solid solution is not present in the as-cast microstructures it is possible that the addition of boron

suppresses the formation to lower temperatures or eliminates its formation in promoting silicide formation. The next phase to form is the NbCr₂ Laves phase, this increases rapidly at first and as the samples cool, it becomes the dominate structure. The solid solution and Nb₅Si₃ silicide decrease in volume as the NbCr₂ Laves phase increases. Below the temperature range studied, the ternary phases are predicted to be stable, however due to non-equilibrium cooling they are not obtained in the as-cast alloy state. The following equations show the progression of transformations:

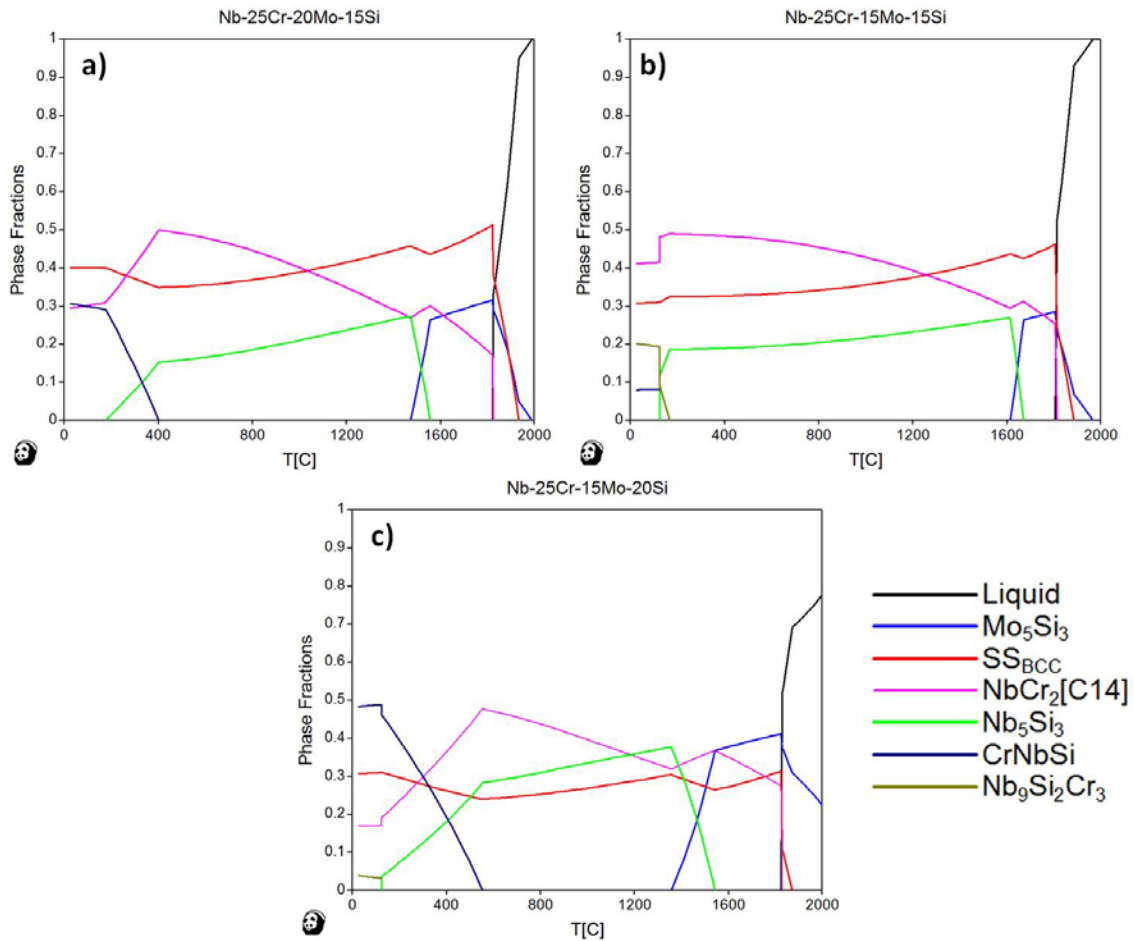
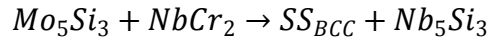
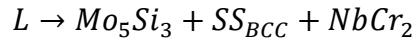
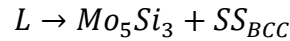
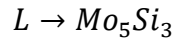


Figure 4.3: Phase fraction curves developed for (a) 10B & 15B, (b) 1515, and (c) 2010 & 2015 alloys.

Investigating the sections of the phase fractions related to the temperature range studied, shown in Figure 4.4, the microstructural changes can be predicted to follow similar trends of decreasing Laves phase and an increase in the solid solution and 5-3 silicide. The 15B and 2015 alloys are the only ones to indicate a predicted fourth phase with an increase in Laves phase at the highest temperatures.

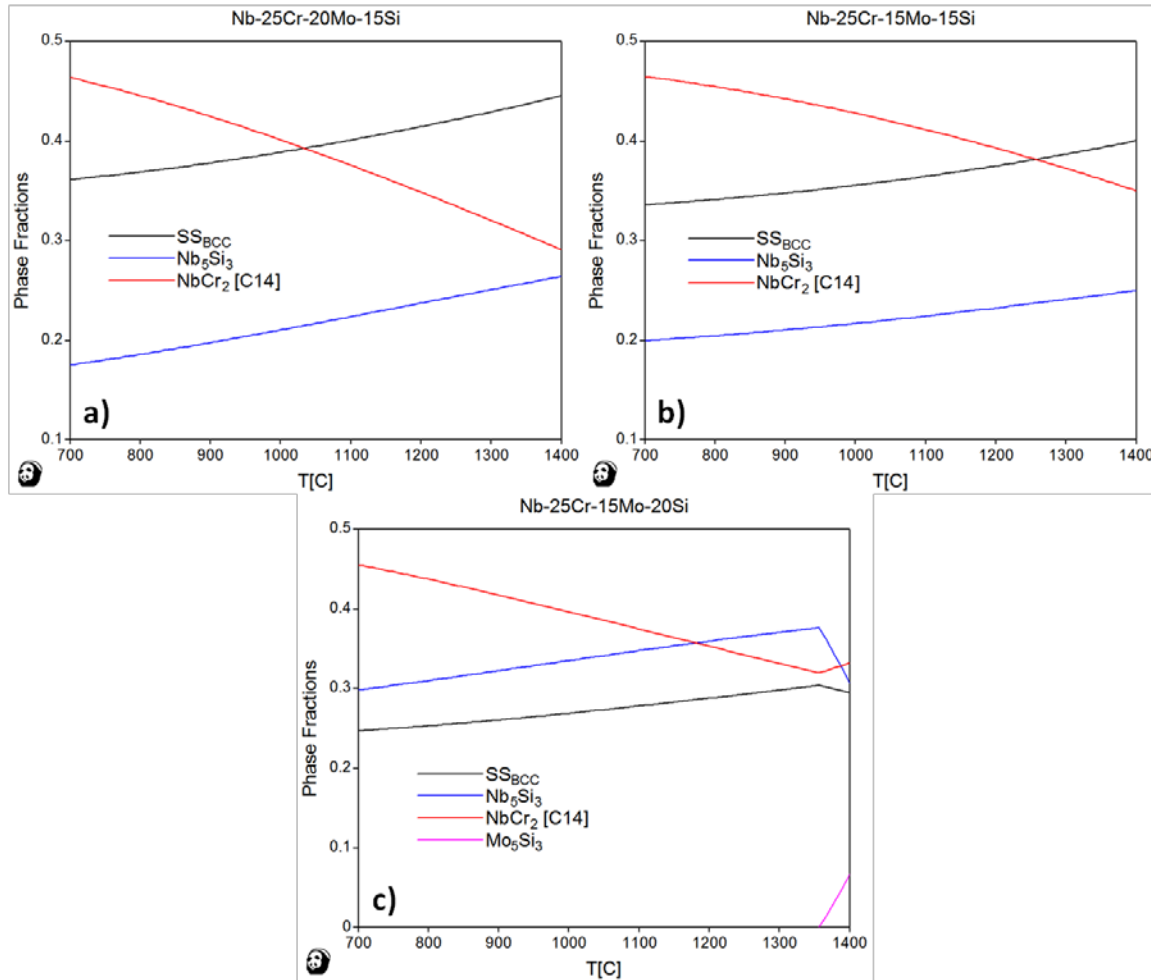


Figure 4.4: Phase fraction curves developed for the (a) 10B & 15B, (b) 1515, and (c) 2010 & 2015 alloys from 700 to 1400°C.

4.2 OXIDATION OF Nb-25Cr-20Mo-15Si-(10, 15)B

Results of previous studies [16, 15] indicated a favorable oxidation response for the two alloys when exposed to elevated temperatures for up to a week. Samples were exposed to cycles of one day for a two week period to determine whether the samples would continue to show the favorable oxidation

response. To examine the changes in the growth of the oxide over the two week period, samples were exposed statically for successive periods of time. Further investigations of a three week long period of exposure were completed to determine further limits of oxidation resistance in the two alloys.

4.2.1 As-cast Characterization

The results for the x-ray diffraction of the as-cast alloys are presented in Figure 4.5. Neither of the alloys showed reflections for a solid solution of either niobium or molybdenum, nor the ternary phases predicted in the room temperature isothermal section. Both alloys were identified to have the NbCr_2 Laves phase with the C14 structure and the $\beta\text{-Nb}_5\text{Si}_3$ silicide.

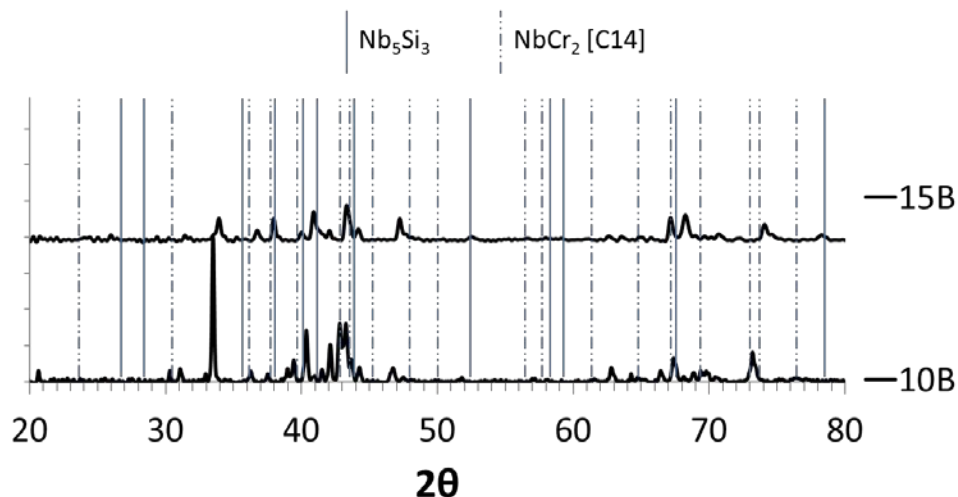


Figure 4.5: XRD results for the as-cast state of the 10B and 15B alloys.

Figure 4.6a and b show the microstructure observed for the 10B alloy at 250X and 1000X magnification. The as-cast microstructure consists of two phases, the light grey corresponds to 5-3 silicide and the dark grey region is the NbCr_2 Laves phase. A negligible amount of α solid solution in the 10B sample was identified. The increased boron addition appears to be unfavorable to the formation of the eutectic like structure found in previous studies [14]. Note that the existence of the 5-3 silicide is assumed to be that of $(\text{Nb},\text{Mo})_5\text{Si}_3$, as the atomic radii of the two metals are similar ($\text{Nb} - 0.143\text{nm}$, $\text{Mo} - 0.136\text{nm}$) allowing for inter-substitution. This is confirmed by high molybdenum content in some

regions with up to 25 atomic percent in select areas, for the ease of analysis the phases are collectively referred to as the 5-3 silicide. For the 15B alloy Figure 4.7a and b show the microstructure observed at 250X and 1000X magnification. The as-cast structure for the 15B alloy is similar to that of the 10B alloy. No trace of solid solution is present in the 15B alloy. The Laves phase appears to be the matrix phase and the 5-3 silicide the secondary phase, the mechanical properties are expected to be poor for this alloy due to the hard matrix/softer second phase make up.

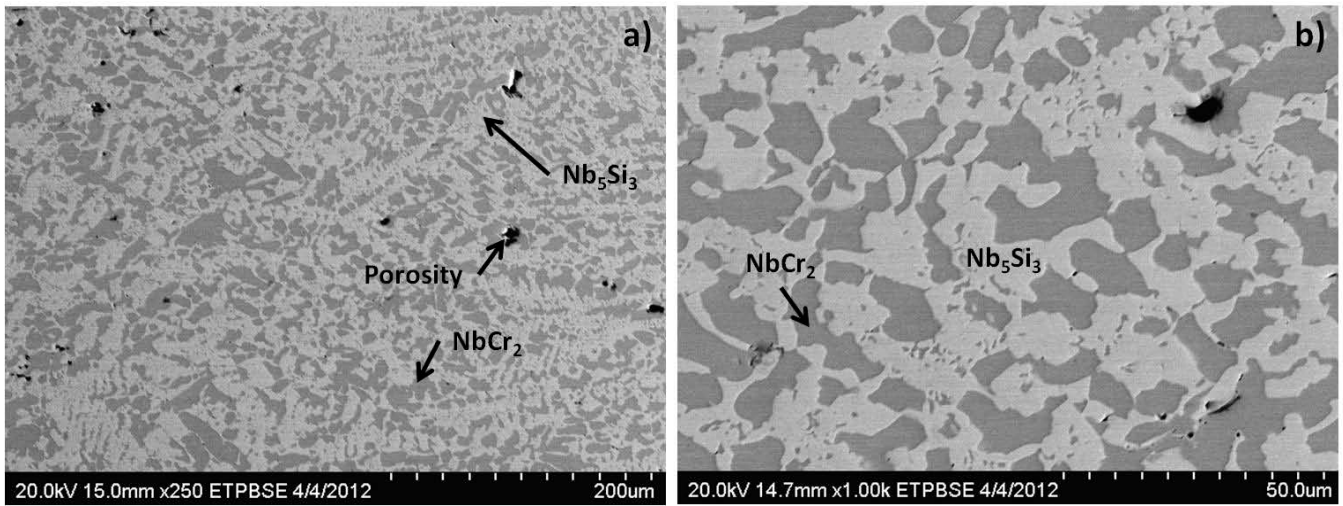


Figure 4.6: As-cast microstructure of the 10B alloy at (a) 250X and (b) 1000X magnification.

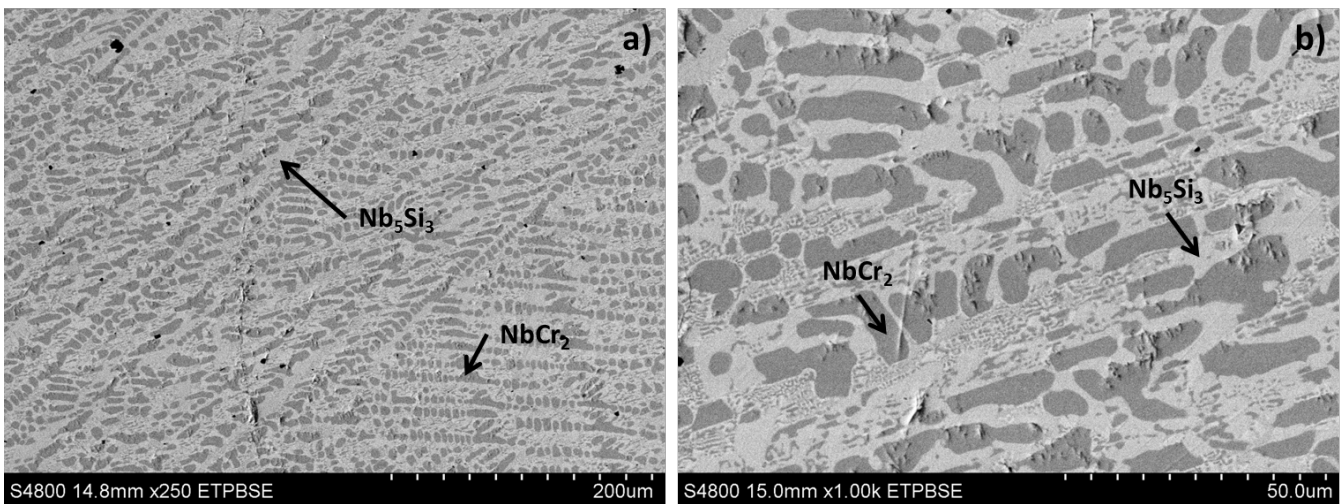


Figure 4.7: As-cast microstructure for 15B alloy at (a) 250X and (b) 1000X magnification.

Image analysis was carried out on the as cast microstructures to determine the phase fractions, results are presented in Table 4.1. Calculations are based on the contrast of each phase present in the as-cast condition at 1000x magnification of backscatter imaging. The 10B shows a difference of 10 points in the ratio of Laves phase to silicide while the 15B contains a nearly even distribution the Laves phase and the 5-3 silicide.

Table 4.1: Phase fractions calculated for as-cast state of 10B and 15B alloys at 1000X.

Alloy	NbCr₂	Nb₅Si₃
10B	46	54
15B	51	49

4.2.2 Two Week Static and Cyclic Oxidation

For the exposure at 700°C, graphs depicting the weight gain per unit area as a function of oxidation time for cyclic oxidation are shown in Figure 4.8 for the 10B and 15B samples. All samples at 700°C exhibit a small initial weight loss after the first 24 hours of exposure after which the 15B samples and the 10B cyclic sample show a gradual weight gain. The 10B samples exposed at 700°C started to develop pest oxidation at the fifth exposure day of cyclic testing. During static testing, pest oxidation developed in the 10B samples after 9 days. The pest product of the 10B samples is visible in the crucible images for the two 14-day samples in Figure 4.9, the sample under static exposure suffered greater pest oxidation than the cyclically exposed sample. There was no appreciable pest product formed in the 15B samples. The oxide products were examined by XRD, the results of which are found in Figure 4.10, both alloys show patterns for CrNbO₄ and Nb₂O₅. While no crystalline form of SiO₂ or B₂O₃ could be identified, however, presence of Si is confirmed by EDS and SEM results, location of boron can only be determined qualitatively as is discussed later. While molybdenum oxide (MoO₃ or Mo₁₃O₃₃) is expected to present at 700°C, peaks corresponding to the pattern were not distinguishable from Nb₂O₅.

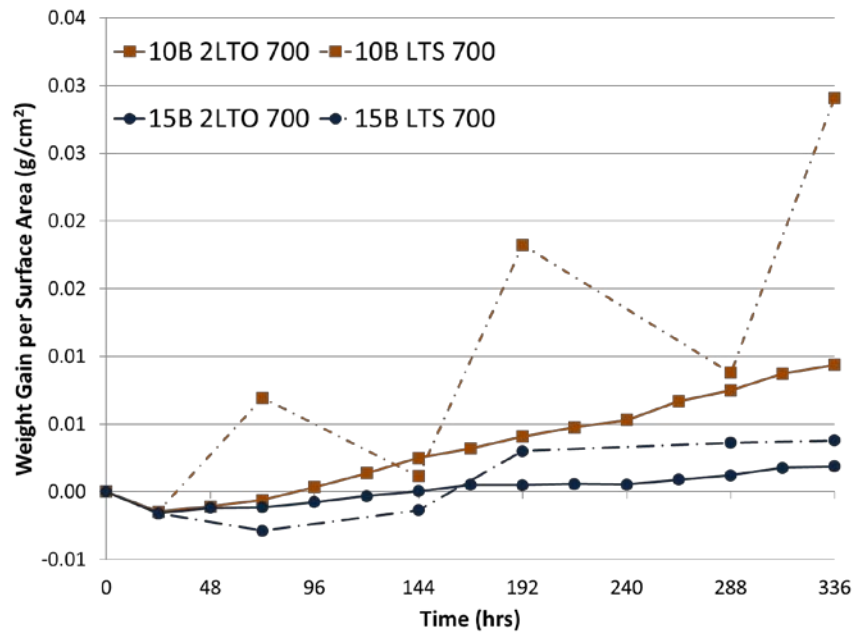


Figure 4.8: Oxidation curve developed for the 10B and 15B alloys at 700°C during two weeks of cyclic oxidation and the curve developed during static oxidation.

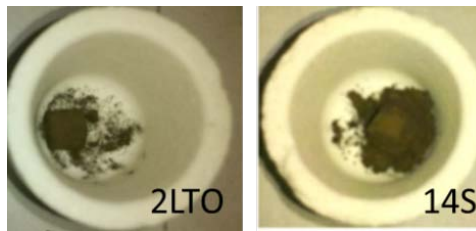


Figure 4.9: Macro images of the pest oxidation exhibited by the 10B samples after 14-days of exposure at 700°C in cyclic (2LTO) and static (14S) modes.

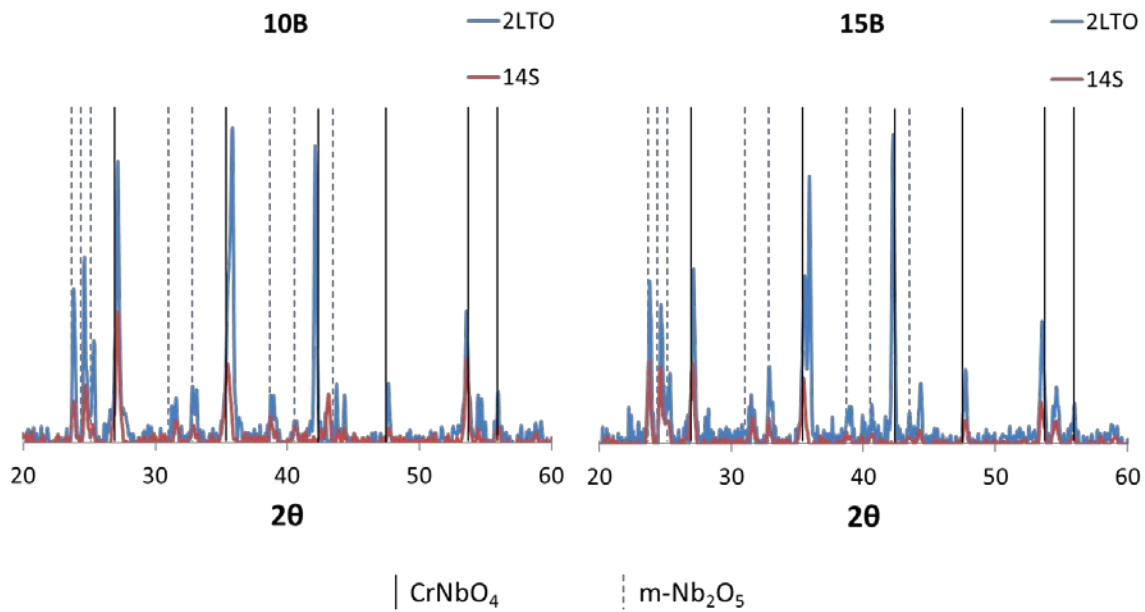


Figure 4.10: X-Ray diffraction results for 10B and 15B alloys after two weeks of cyclic and static oxidation at 700°C, scans of the 14S sample is characteristic of those found for the successive static exposures.

Samples were sectioned in order to examine the metal remaining and investigate the oxide-metal interface developed during exposure. The micrographs in Figure 4.11 show the changes in the 10B microstructure during the static test compared with that of the two week cyclic sample. After 3 days of exposure there is little change in the 10B microstructure from the as-cast structure. After six days of exposure there appears to be a eutectic like formation in the inter-dendritic regions of the Laves phase, by nine days of exposure, the eutectic can be resolved to contain three regions of contrast: a white phase, the dark grey Laves phase, and the light grey 5-3 silicide. Through EDS analysis the white phase was identified to be a Mo-rich solid solution. The Mo-rich solid solution is likely part of the reason for the extensive pest oxidation at 700°C, especially in the static samples. The cyclically exposed sample did not show the formation of the eutectic, accordingly it had also suffered less pest damage. The lack of the eutectic formation may be due to the interruption of the diffusion process of the atoms by the nature of the test as the changes in the static samples were not visible until a six day continuous exposure had occurred. Recall that annealing times to acquire equilibrium structures in niobium alloys take 100 hours.

Metal remaining for the 10B sample after 14 days of exposure was estimated to be at 70-80% for the static sample and 90-95% for the cyclic sample.

The micrographs of the 15B alloys microstructure in Figure 4.12 exhibited little variation from the as-cast state across the different static exposure periods with only isolated instances of the eutectic found in the 14-day static sample. Likewise the cyclic sample did not show any microstructural variation from the as-cast. The high boron content within the samples assists in maintaining the two-phase structure of the NbCr₂ Laves phase matrix with 5-3 silicide plates, the method by which this is done would require further investigation. Metal remaining for the 15B samples was estimated to be 90-95%.

Macroscopic images of the results for the static 10B and 15B samples are shown in Figure 4.13, showing the extent of pest damage in the 10B sample. The oxide metal interfaces developed static testing are found in Figure 4.14 and the interfaces developed after cyclic oxidation are found in Figure 4.15. For all samples the scale is comprised of Nb₂O₅ with some un-oxidized particles of NbCr₂. While neither scale appears to be well-adherent to the surface no pest product was observed in the crucible for the 15B alloy suggesting that the scale cracked during the sectioning and polishing. The results of the 700°C exposure suggest that with higher boron content, the low temperature pest oxidation can be reduced, if not eliminated completely, however a fragile scale is formed at low temperatures. The lack of a protective oxide formation may be attributed to the predominance of Nb₂O₅ in the scale.

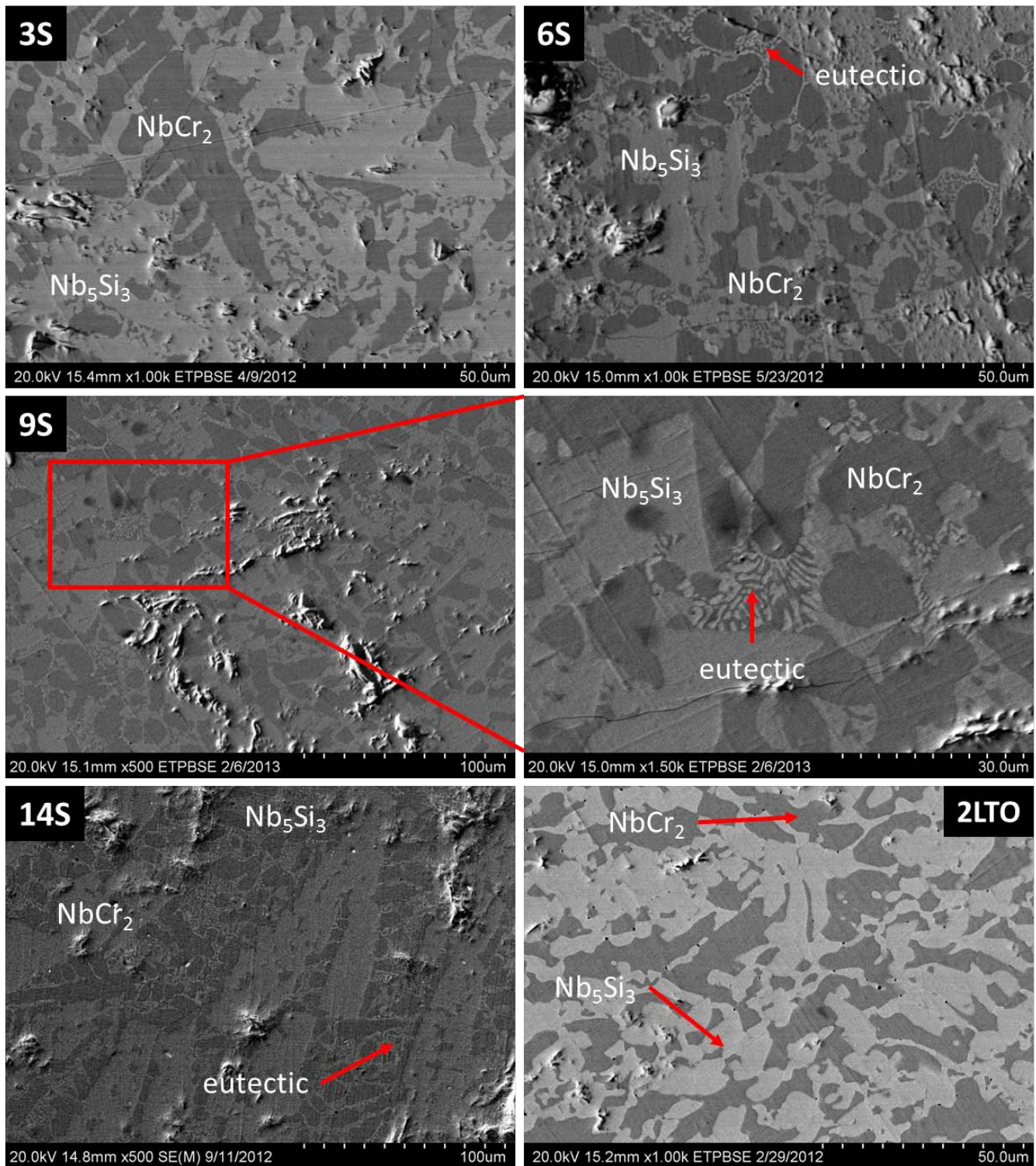


Figure 4.11: Microstructure morphology for the 10B sample during static testing compared with the cyclic sample.

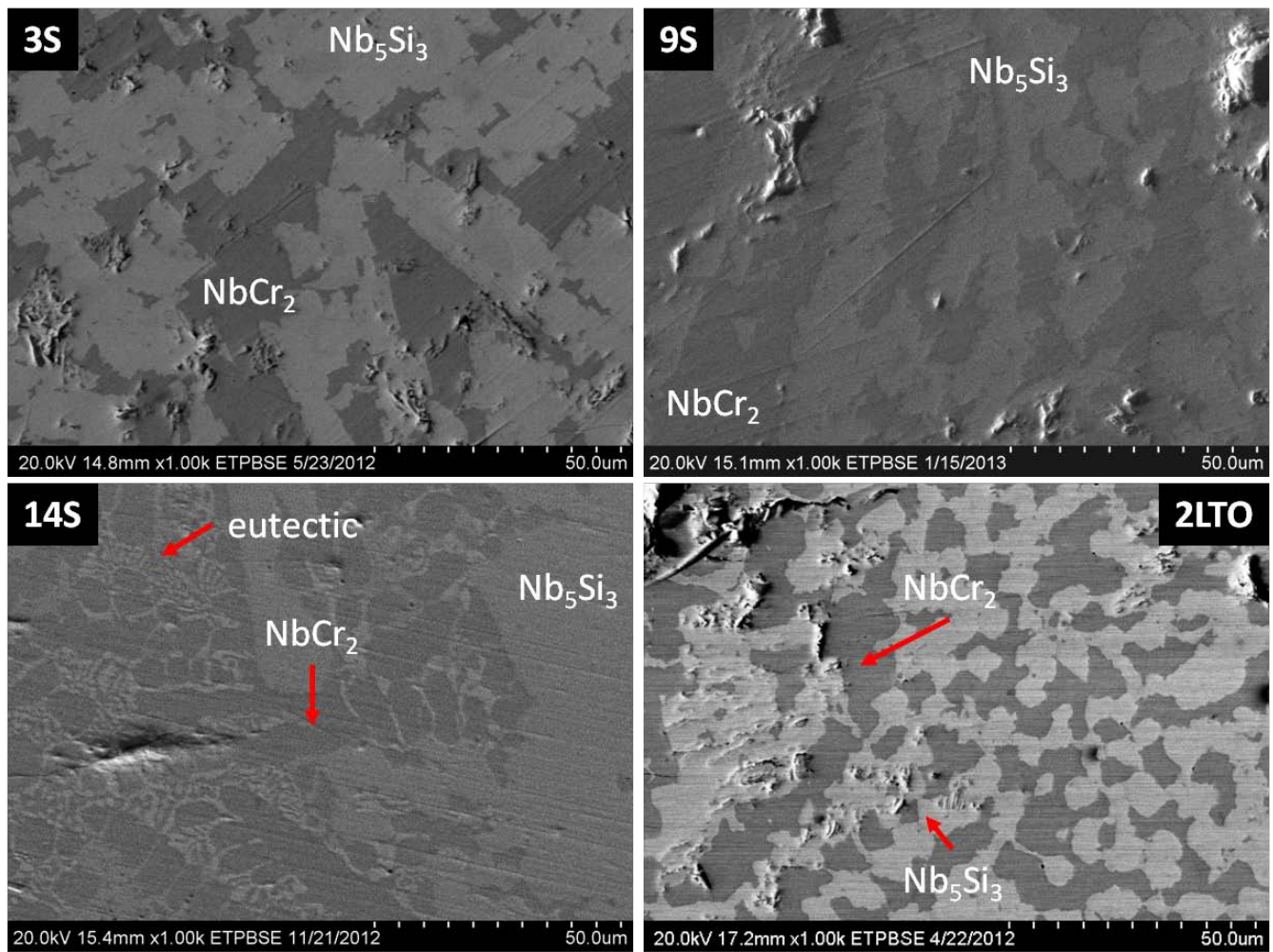


Figure 4.12: Microstructure morphology for the 15B sample during static testing compared with the cyclic sample.

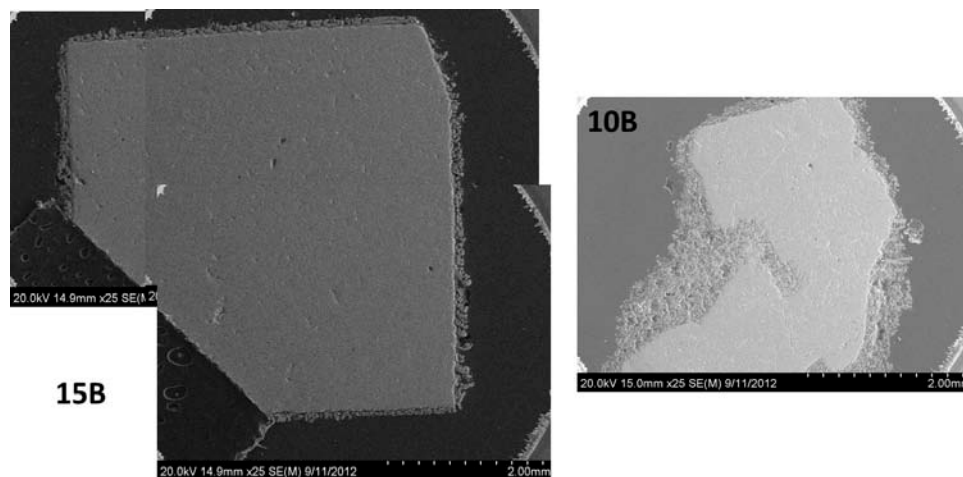


Figure 4.13: Low-magnification images for the cross sections of the 10 and 15B alloys after two weeks of static exposure.

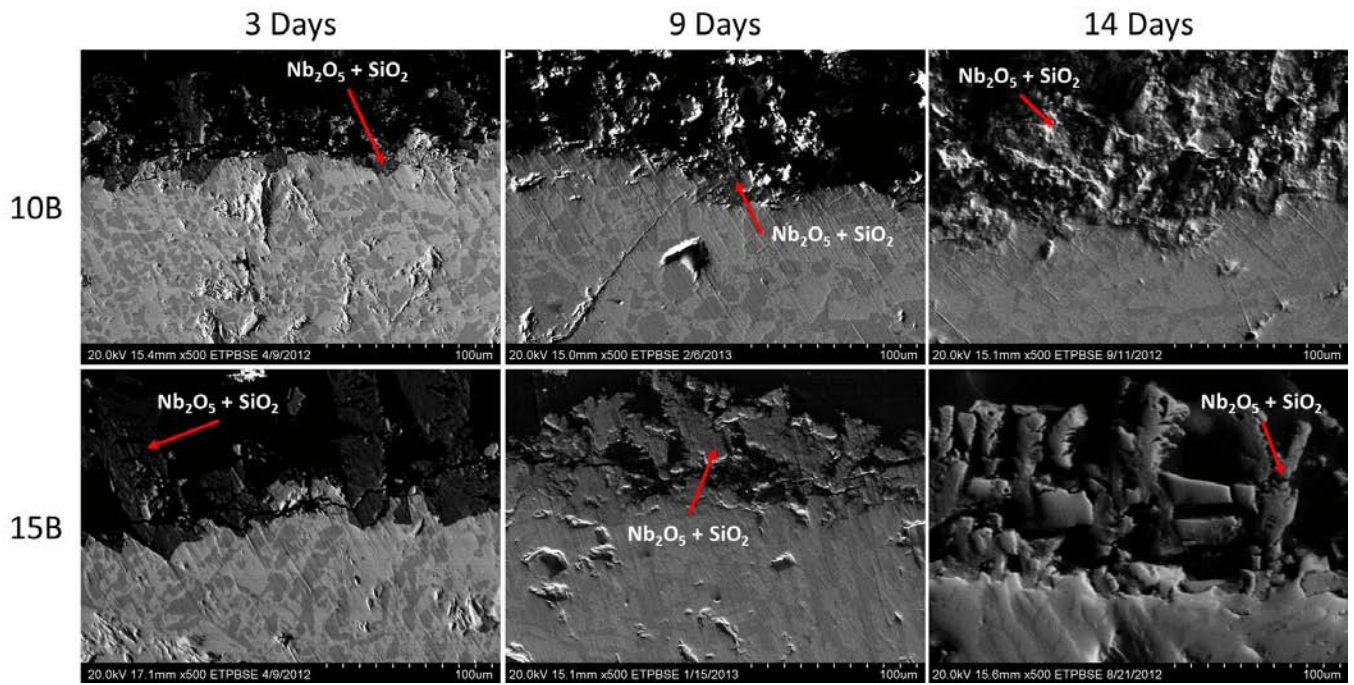


Figure 4.14: Oxide-metal interface developed during static exposure at 700°C after stated period of days for the 10 and 15B alloys.

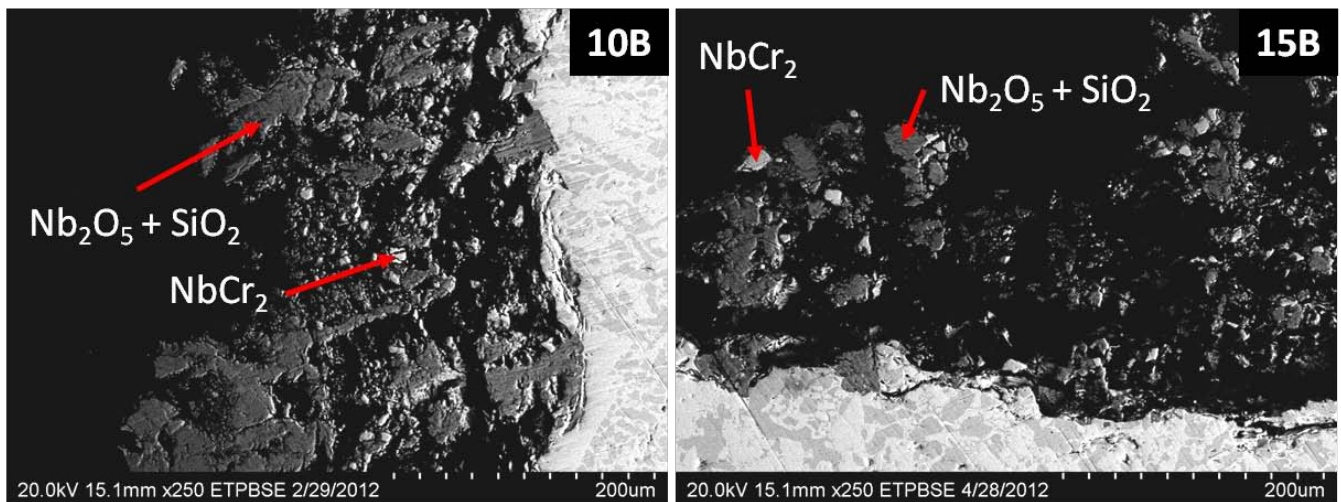


Figure 4.15: Oxide-metal interface developed during cyclic exposure at 700°C for the 10 and 15B alloys.

Gravimetric curves developed for the samples exposed at 900°C are shown in Figure 4.16. There is a higher oxidation resistance for all samples from the 700°C exposure and most notably for the 10B static sample. All samples showed an initial weight loss, likely due to volatile oxides. No pest

product was observed for any sample at this temperature. After sectioning, all samples were estimated to have 95-99% metal remaining.

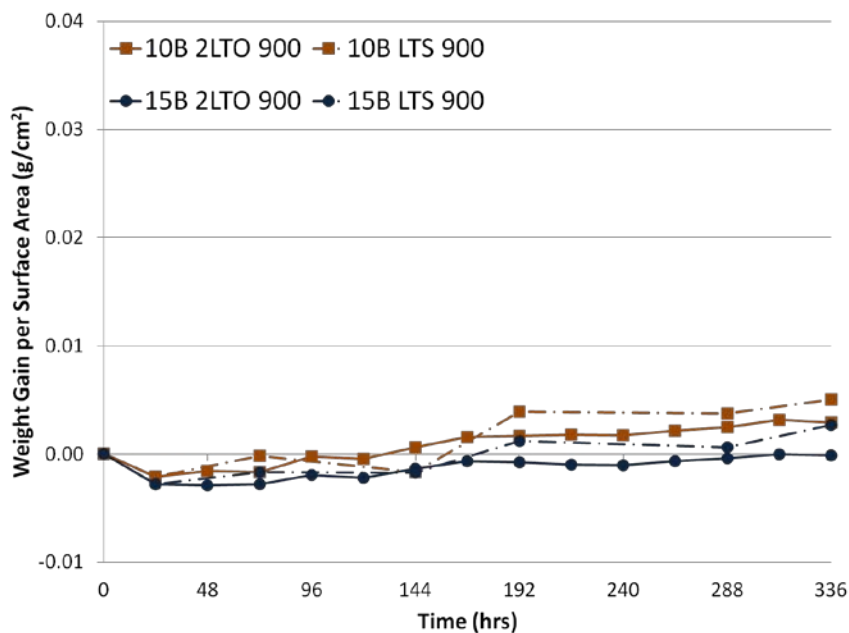


Figure 4.16: Oxidation curve developed for the 10B and 15B alloys at 900°C during two weeks of cyclic oxidation and the curve developed during static oxidation.

Microstructural morphology for the samples exposed at 900°C are presented in Figure 4.17 for the 10B alloy and Figure 4.18 for the 15B alloy. Similar to the exposure at 700°C there is the formation of a eutectic like structure in the inter-dendritic regions of the 10B samples, additionally within 3 days of exposure there is the development of needle like precipitates within the Laves phase. Through EDS analysis these are identified as being Mo-rich, likely a formation of the solid solution. This result is similar to findings in the short term oxidation studies [15]. Both the eutectic and the Mo precipitate persist in the microstructure up to the full 14 days of exposure and are also visible within the cyclically exposed samples. The 15B alloy showed no variation from the as-cast state in either the static or cyclic exposure, even after the 14 days of continuous exposure.

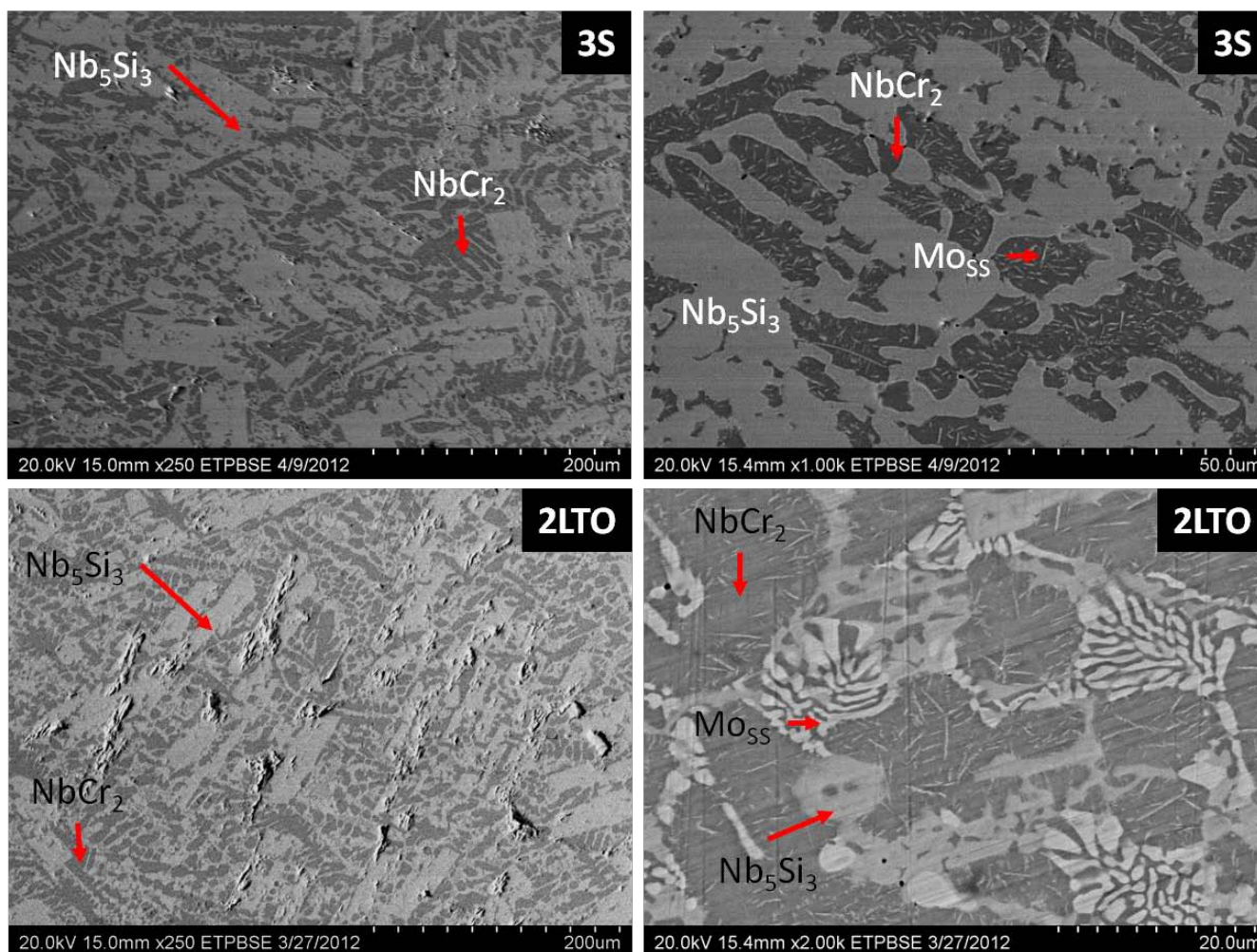


Figure 4.17: Microstructure morphology for the 10B sample during static testing at 900°C compared with the cyclic sample.

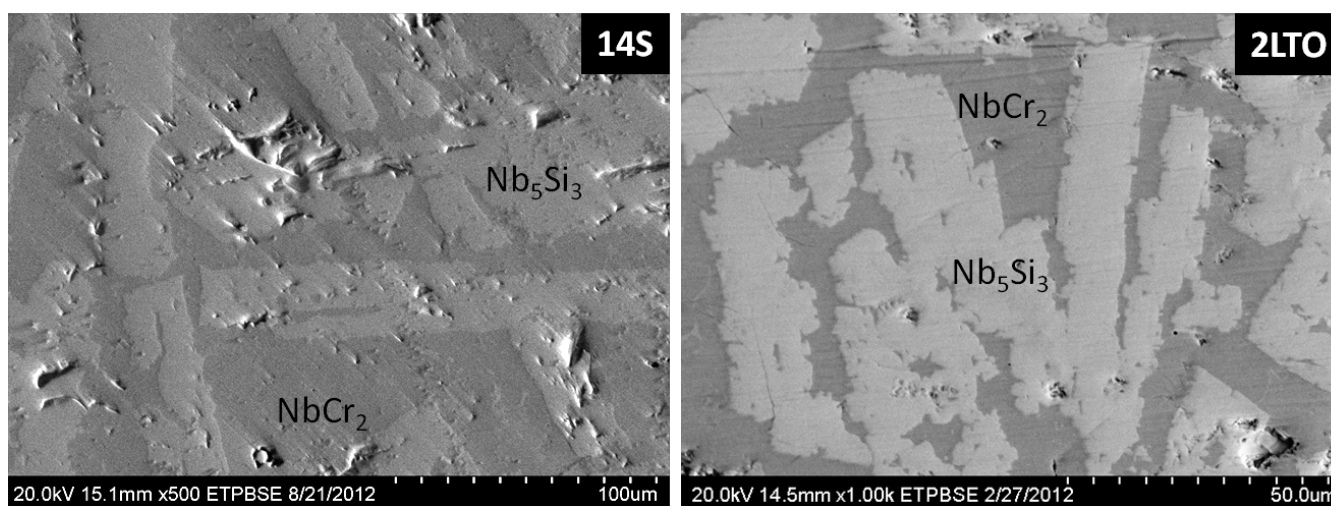


Figure 4.18: Microstructure morphology for the 15B sample during static testing at 900°C compared with the cyclic sample.

As shown in Figure 4.19 the XRD patterns suggest that at 900°C the oxide is primarily composed of Nb₂O₅ and CrNbO₄ for the 10B alloy and the cyclic 15B sample, while the 15B static sample tends to only show the CrNbO₄ pattern.

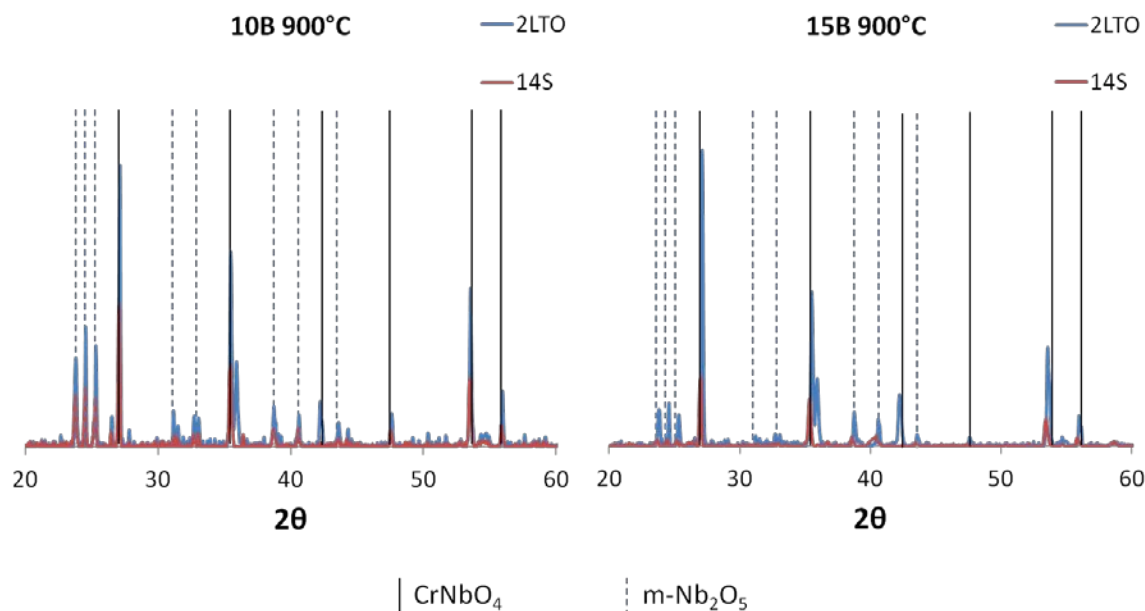


Figure 4.19: X-Ray diffraction results for 10B and 15B alloys after two weeks of cyclic and static oxidation at 900°C, scans of the 14S sample is characteristic of those found for the successive static exposures.

The oxide metal interface developed during static testing of the 10B alloy at 900°C is shown in Figure 4.20. Initially the primary oxides formed are the columnar like growths of Nb₂O₅ and SiO₂ formed from the 5-3 silicide with some surface oxidation of CrNbO₄. With the extended periods of exposure the oxidation of the Laves phase and outward diffusion of Cr form a CrNbO₄ layer that extends around the base of the Nb₂O₅ oxide. The oxide developed for the 10B alloy (Figure 4.21) during cyclic testing shows much the same response with the magnified view of the oxide metal interface shows the layering of CrNbO₄ and SiO₂ within the scale. At 900°C the 10B shows the most dependence on what phase(s) are being oxidized to form the scale, if the Laves phase and eutectic region were being oxidized, only a thin layer is formed; if the phase at the surface is the 5-3 silicide then the large volume Nb₂O₅ forms and the oxidation of the silicide occurs at a faster rate, allowing a path for oxygen to diffuse

through. In the case of the eutectic region and the Laves phase; CrNbO_4 forms much more quickly as it does not have to wait for the Cr to diffuse from another phase, SiO_2 forms concurrently, filling the pores left by the volatilizing MoO_3 .

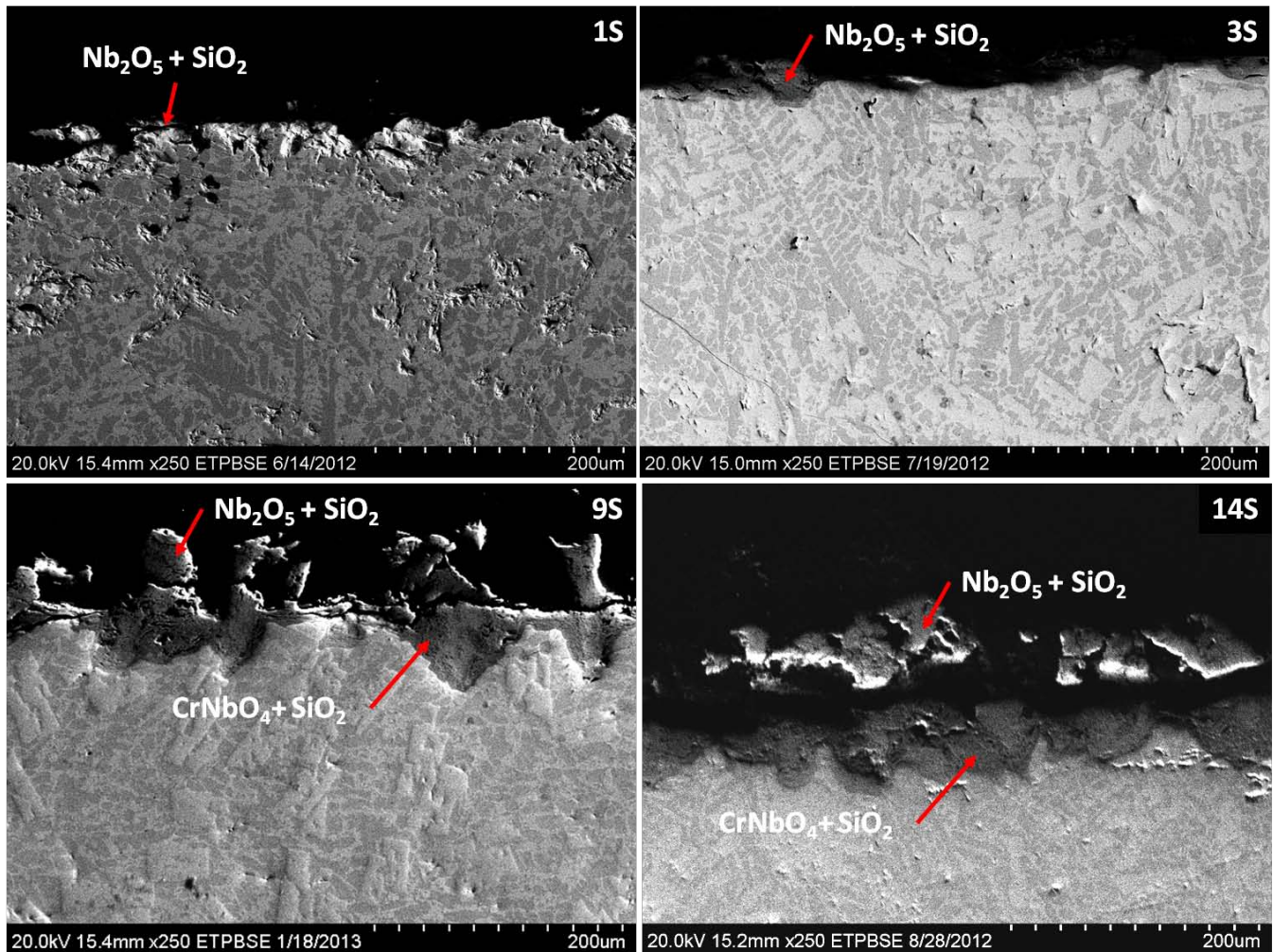


Figure 4.20: Oxide-metal interface developed during static exposure at 900°C after indicated period of days for the 10B alloy.

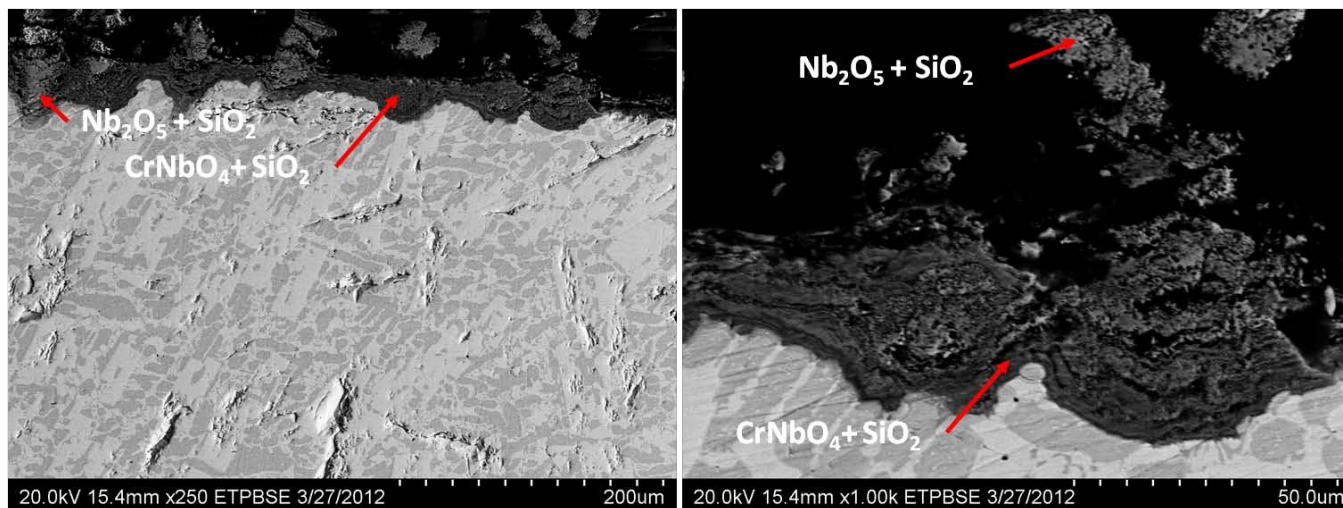


Figure 4.21: Oxide-metal interface developed during cyclic exposure at 900°C for the 10B alloy.

The oxide scale developed for the 15B alloy during static and cyclic oxidation at 900°C has similar features to the scale developed by the 10B alloy as shown in Figure 4.22. After the first day of static oxidation there is only a very thin scale of primarily CrNbO_4 and SiO_2 with negligible amounts of Nb_2O_5 . The successive exposure periods reveal more development of the CrNbO_4 and SiO_2 oxide with Nb_2O_5 located near the oxide metal interface. In both the 10B and 15B samples a thin Cr depletion layer is found at the oxide metal interface, the layer is detailed by the EDS map of Cr for the two samples in Figure 4.23.

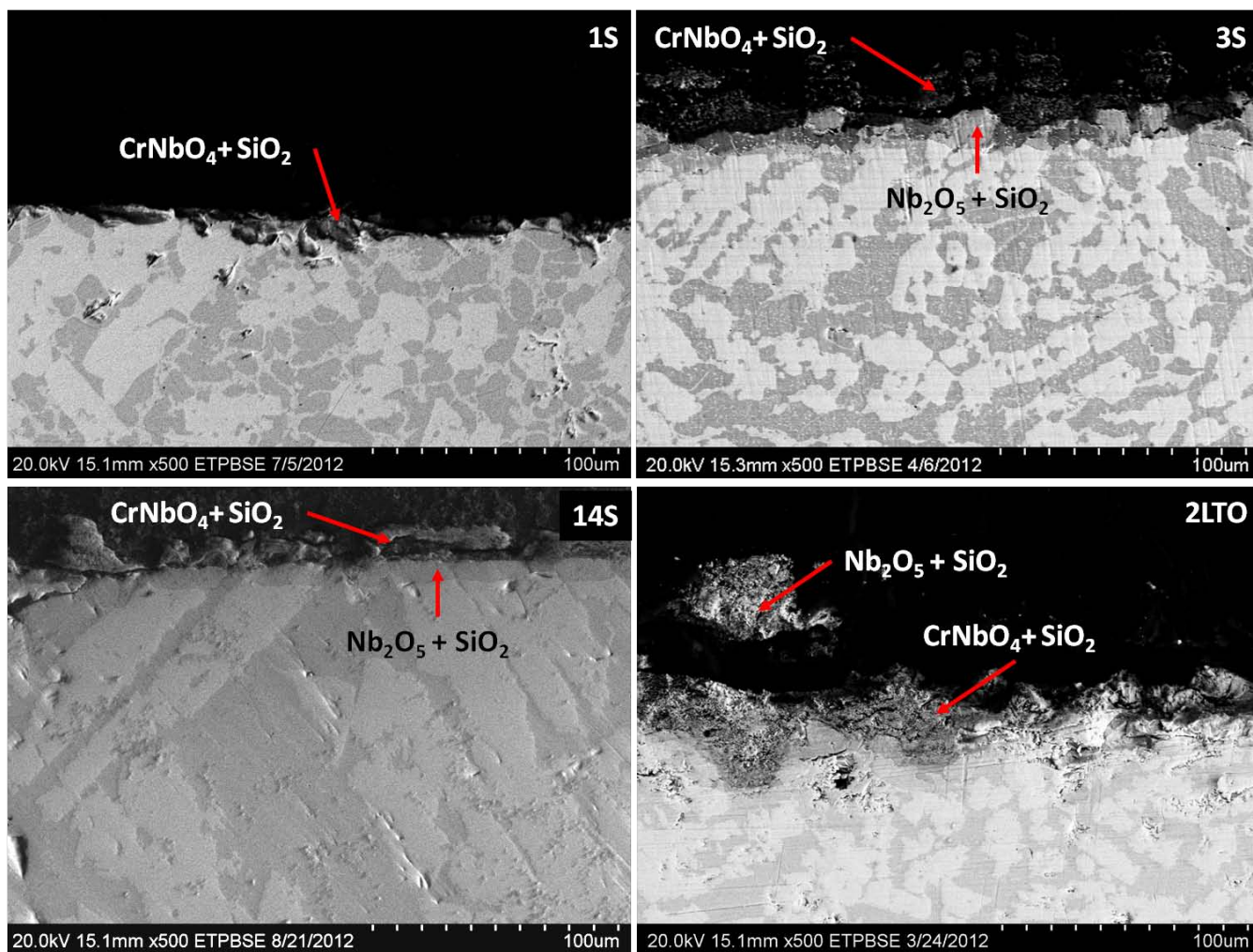


Figure 4.22: Oxide-metal interface developed during static exposure at 900°C after indicated period of days and oxide developed during cyclic testing for the 15B alloy.

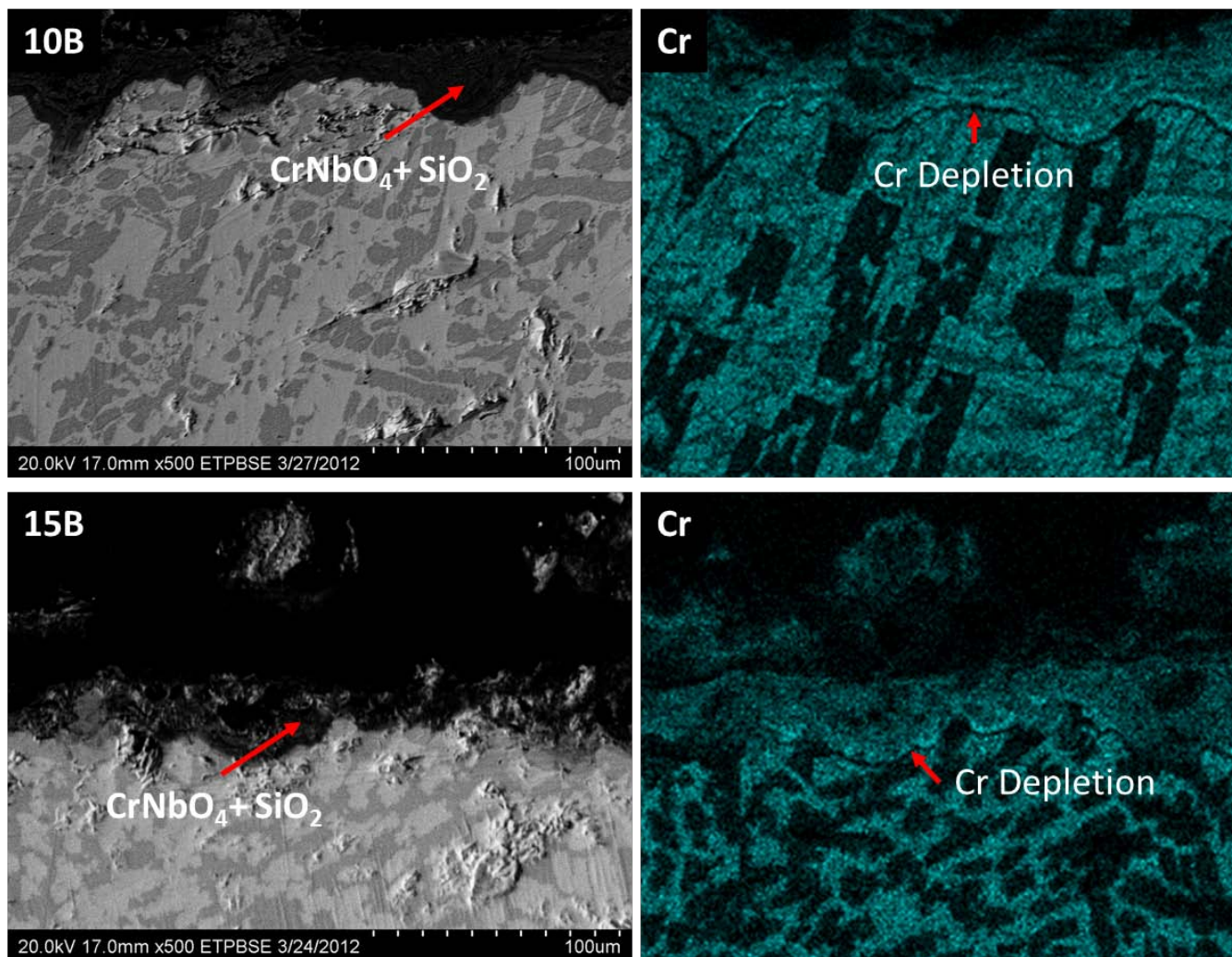


Figure 4.23: EDS map of Cr showing thin depletion layer developed in both the 10 and 15B samples during cyclic testing.

Gravimetric curves developed for the samples exposed at 1100°C are shown in Figure 4.24. The 10B sample at 1100°C begins to show a rapid increase in weight gain after the seventh day of exposure in both static and cyclic modes, developing a swollen oxide. Upon sectioning it was found that for the 10B cyclic sample approximately 20% metal remained in the cyclic sample exposed for 14 days and 10% remained for the cyclic sample due to the formation of a dense non-protective scale that inwardly consumed the base material. For the 15B sample, the weight gain per surface area appears to level off after twelve days of exposure and retained 95-99% of the base material after all exposure periods.

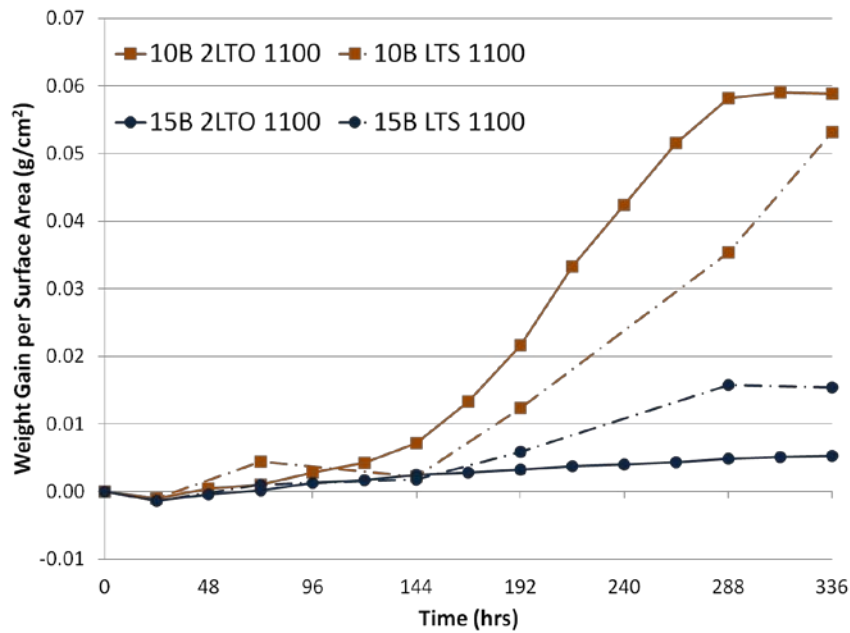


Figure 4.24: Oxidation curve developed for the 10B and 15B alloys at 1100°C during two weeks of cyclic oxidation and the curve developed during static oxidation.

The morphology of the microstructures for the samples during static and cyclic testing is shown in Figure 4.25 for the 10B samples and Figure 4.26 for the 15B samples. The 10B continues to develop the Mo_{SS} precipitate within the Laves phase and the eutectic like structure, as seen at 900°C. The 15B sample also develops the Mo_{SS} during static testing after 14 days, but does not develop it in the cyclic samples. The bulky oxide that develops in the 10B sample may be related to the larger percentage of solid solution that is present within the eutectic like structure that the 15B samples lack.

After oxidation the developed oxides were analyzed by XRD, the results of which are found in Figure 4.27. Like previous exposures the two oxides identified are the monoclinic Nb_2O_5 and CrNbO_4 . However, in the case of the 15B samples, a peak corresponding to cristobalite- SiO_2 was identified suggesting that at this temperature rather than an amorphous structure, the silica has some crystallinity.

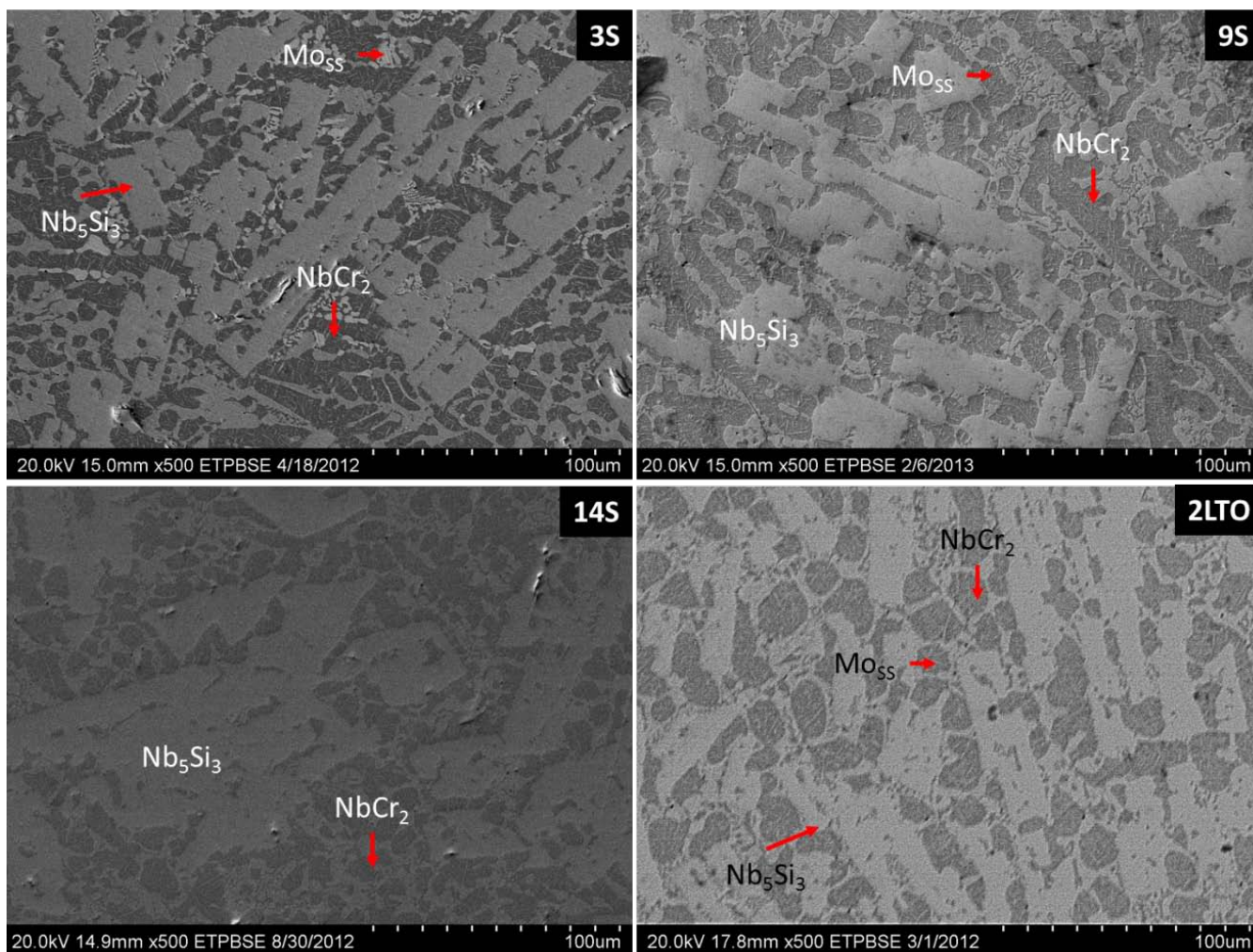


Figure 4.25: Microstructure morphology for the 10B sample during static and cyclic testing at 1100°C.

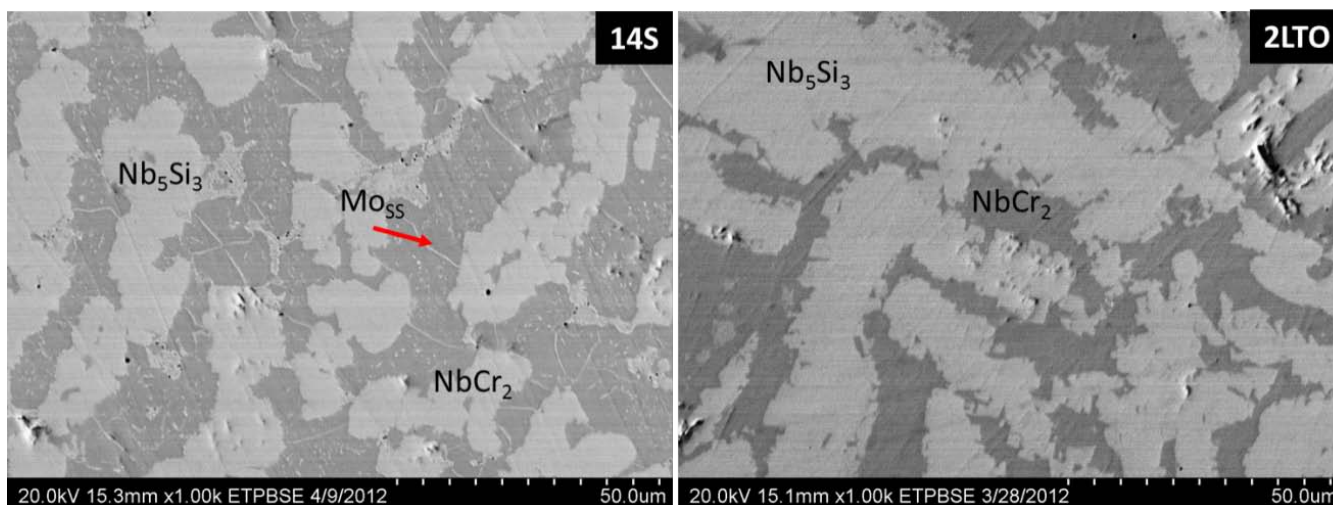


Figure 4.26: Microstructure morphology for the 15B sample during static and cyclic testing at 1100°C.

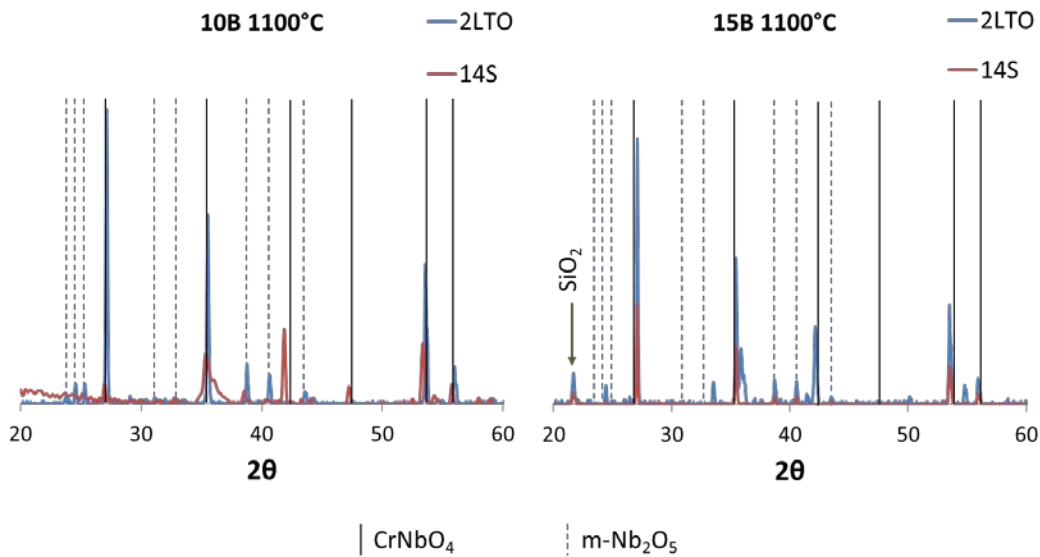


Figure 4.27: X-Ray diffraction results for 10B and 15B alloys after two weeks of cyclic and static oxidation at 1100°C, scans of the 14S sample is characteristic of those found for the successive static exposures.

Oxide metal interfaces developed during static testing for the stated period of days for the 10B and 15B alloys are found in Figure 4.28. Up to nearly a week of exposure at 1100°C the 10B and 15B alloys maintain similar oxidation behavior merely showing the development of a thicker oxide layer than was developed previously at 900°C, with some of the same features, as shown in the left most micrographs. As is seen in the 9 and 14 day exposure images, the oxide develops a great deal of micro-porosity in a thick layer of CrNbO_4 and SiO_2 , interspersed with some isolated Nb_2O_5 . The developed oxide is fairly compact, with porosity coarsening near to the outer surface of the scale. Low-magnification images of the cross section for the 10B alloy samples after two weeks of exposure at 1100°C are shown in Figure 4.29 to show extent of oxidation of the samples. Details of the oxide-metal interface with the associated EDS maps are shown in 4.30. The sample exhibits a thick scale with porosity due to volatile oxides, such as MoO_3 and B_2O_3 . The 10B samples, the scale exhibits CrNbO_4 and SiO_2 with needle like features of Nb_2O_5 , previously seen in niobium based alloys with 5 atomic percent Boron exposed in air for a 24 hour period [14]. A thin chromium and silicon depletion region is

noted in the micrographs, this is most easily viewed by comparing the SEM image with the EDS mapping.

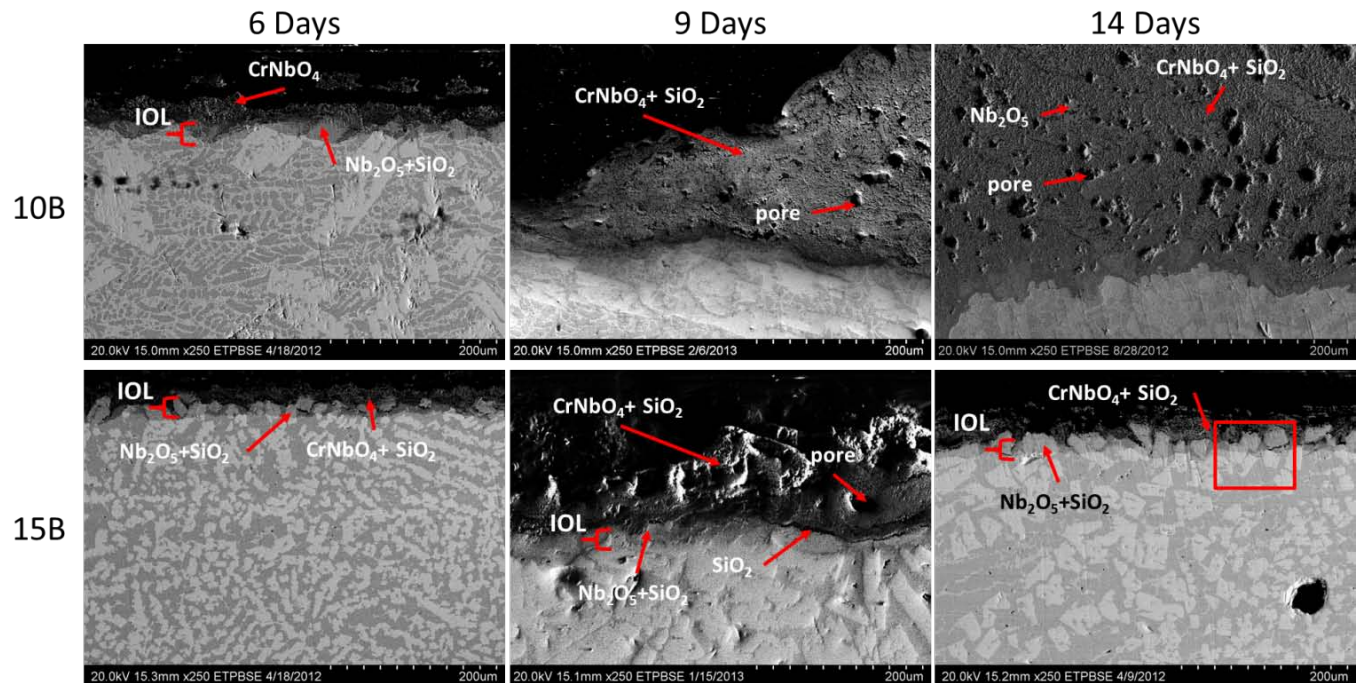


Figure 4.28: Oxide-metal interface developed at 1100°C after stated period of days for the 10 and 15B alloys.

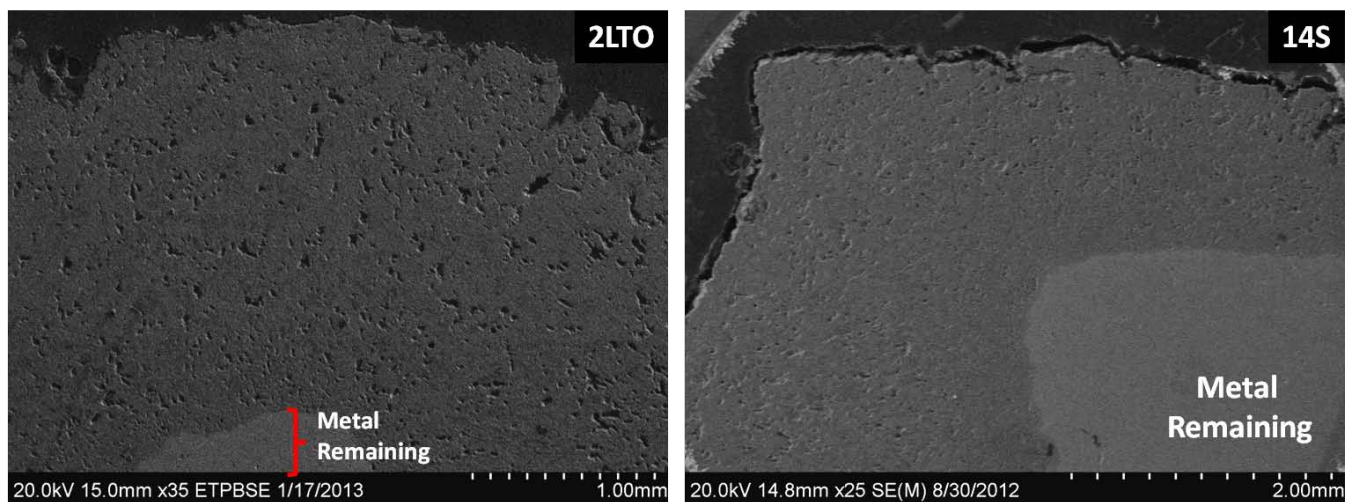


Figure 4.29: Low magnification images of the oxide scale developed for the 10B sample at 1100°C after cyclic and static exposure for two weeks.

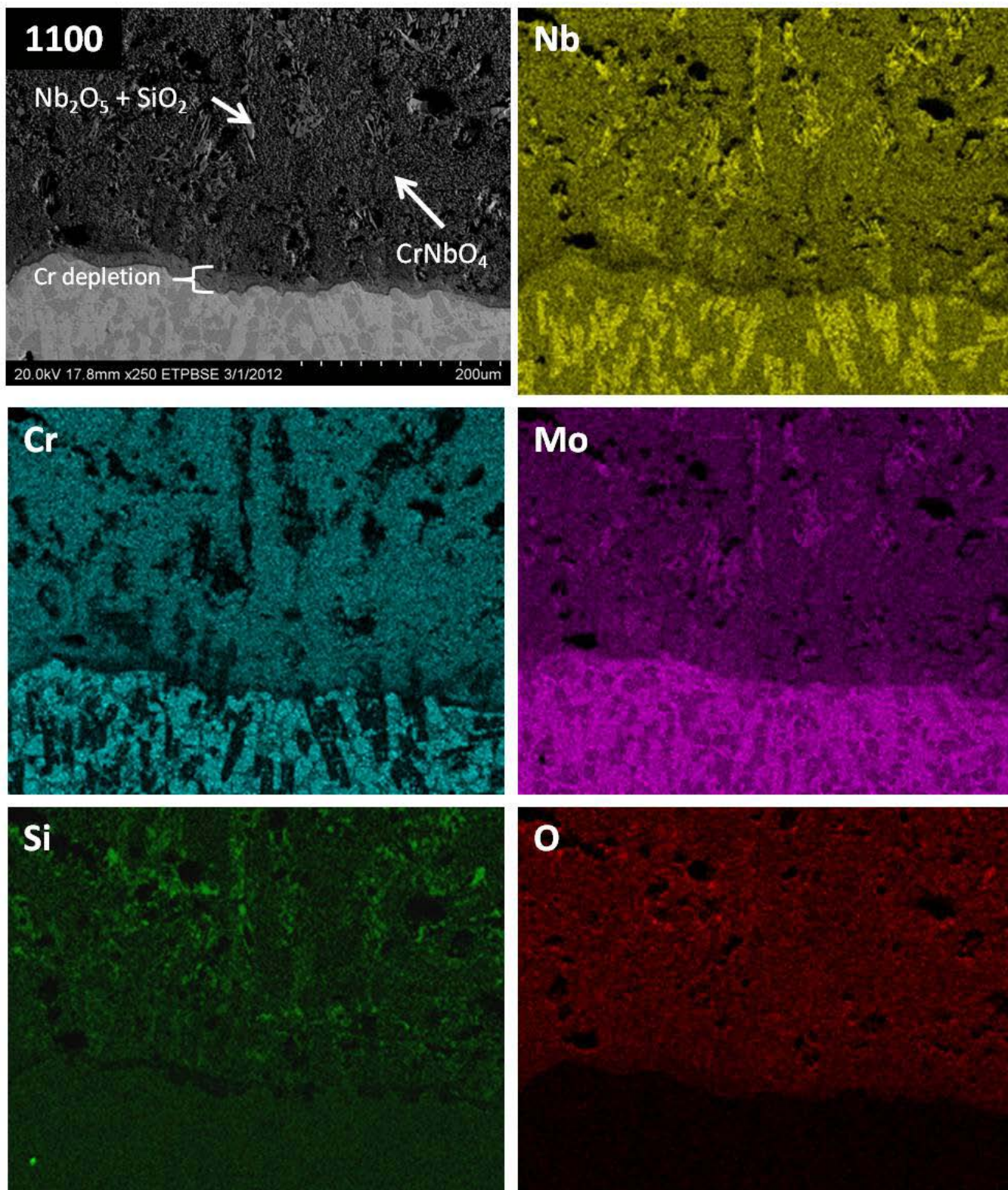


Figure 4.30: EDS mapping of the oxide-metal interface developed in the 10B sample at 1100°C.

The thick scale of the 10B samples is contrasted sharply with the thinner scale of the 15B samples shown in Figure 4.28. The 15B maintains the relatively thinner scale up to the end of the two week exposure; details of the interface formed by 14 days of exposure are further seen in Figure 4.31. The Mo-rich precipitate that is found within the Laves phase oxides into most likely MoO_3 which is primarily located around the edges of Nb_2O_5 . Some internal oxidation has occurred in the sample, forming the small particles of SiO_2 along the 5-3 silicide grain boundaries. The scale has a near uniform thickness which, including the intermediate layer is approximately 100-120 μm thick. The 15B alloy samples had more well-developed intermediate oxidation layer (IOL) than that of the 10B samples, the details of which are presented in Figure 4.32. The IOL includes chromium and silicon depleted regions, which correspond to molybdenum and niobium enrichment, as shown by the x-ray maps. There is a notable chromium rich region adjacent to the SiO_2 layer, which may contain residual Cr_2O_3 , a desirable oxide product that melts at 2330°C and vaporizes at 3000°C. However, surface oxidation of Cr_2O_3 into CrO_3 can attribute to material loss at temperatures 1000°C and above [52, 47].

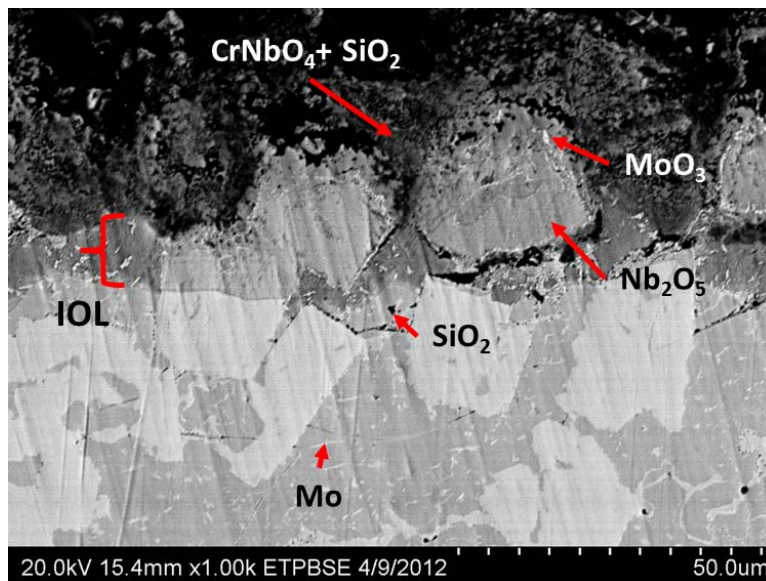


Figure 4.31: Magnification of region indicated in Fig.4.28.

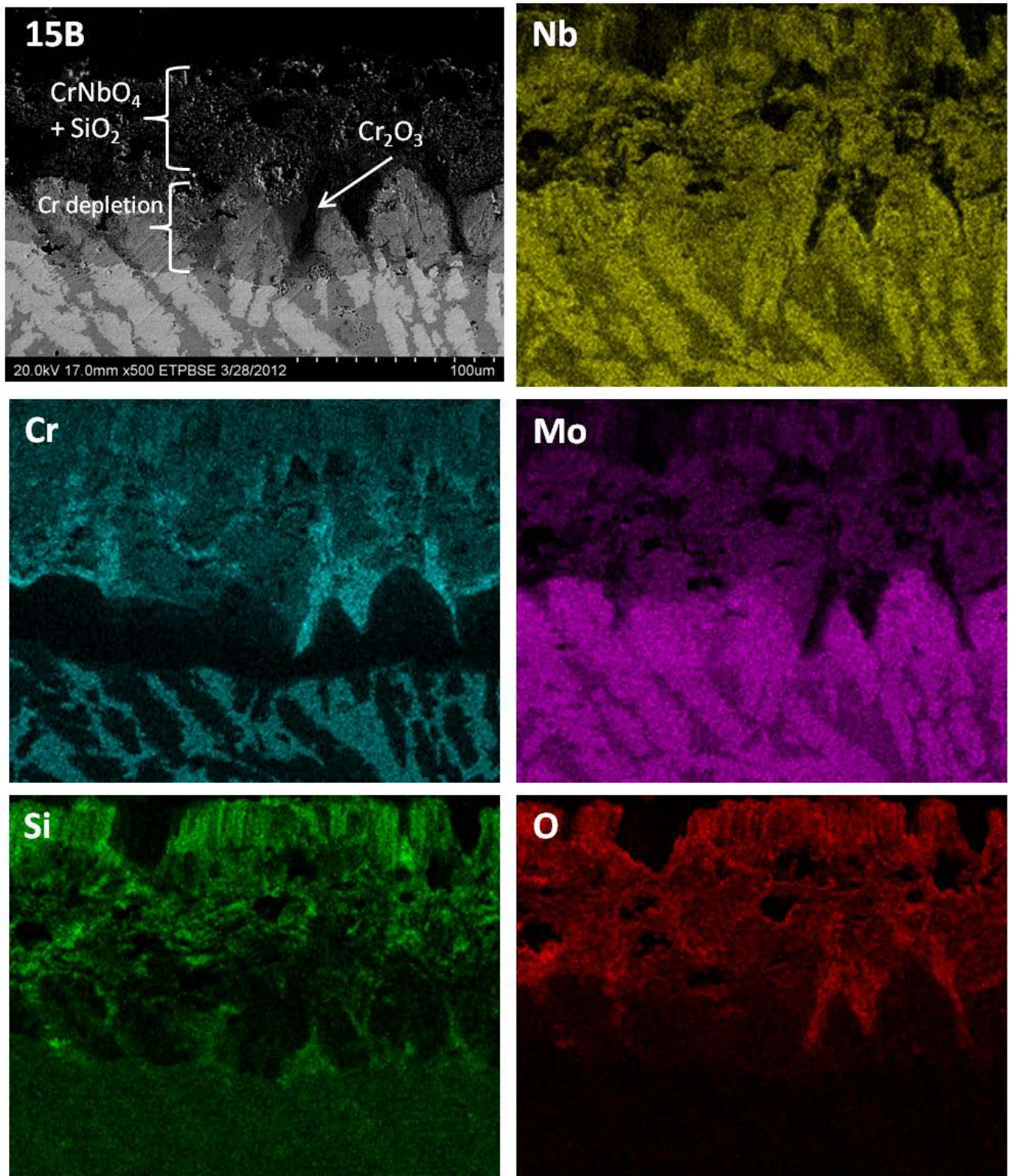


Figure 4.32: EDS mapping of the oxide-metal interface developed in the 15B sample at 1100°C.

Oxidation curves developed during static and cyclic testing at 1300°C are presented in Figure 4.33 for the 10B and 15B alloys. All samples showed a high initial weight gain, suggesting that the formation of non-volatile oxides primarily predominated at this temperature. For the cyclic samples the initial weight gain was followed a near parabolic growth up to 336hrs. Upon sectioning the 1300°C sample, the percent metal remaining is estimated to be 40% for the 10B sample and 85% for the 15B samples. The 10B static sample at 1300°C exhibited an increase in resistance over its cyclic counterpart, with approximately 80% metal remaining along with the indicated lower weight gain. For the 15B alloy, excepting the sample exposed for 12 days that had no metal remaining, the 14 day static sample is estimated to have 60% metal remaining. While the gravimetric results at 1300°C for the 10B and 15B samples would suggest that the 10B had a better oxidation resistance, the metal remaining as determined by the cross sections show that the 10B has less resistance. Likely, greater amounts of volatile oxides in the 10B sample were able to escape into the atmosphere than that of the 15B.

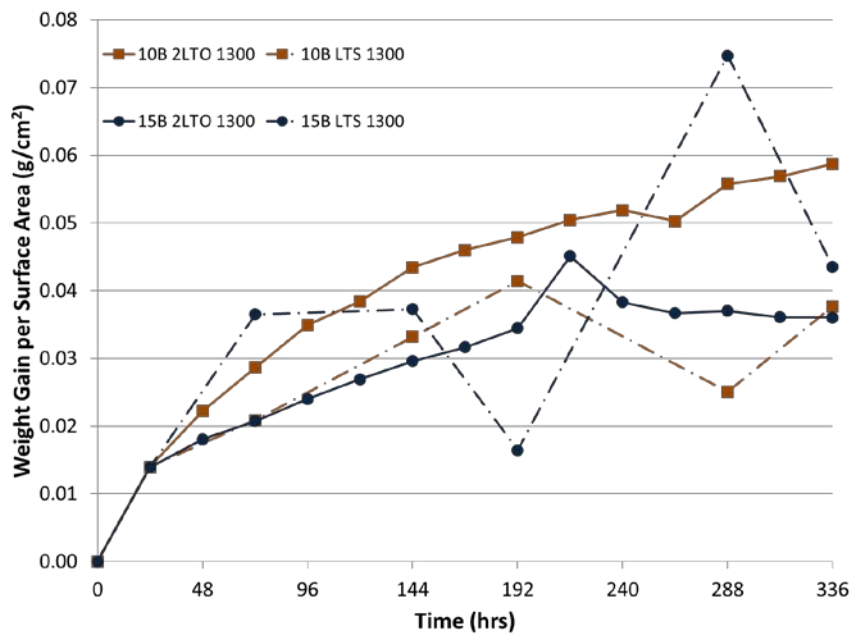


Figure 4.33: Oxidation curve developed for the 10B and 15B alloys at 1300°C during two weeks of cyclic oxidation and the curve developed during static oxidation.

Samples were sectioned and polished to allow for evaluation of any microstructural changes and oxide-metal interface evaluation that occurred during the oxidation. The base metal microstructural morphology is shown for the 10B and 15B samples in Figure 4.34. Minimal variation in the microstructure was seen for the static samples for the shorter time periods. The eutectic like region developed in the 10B samples is most well defined at 1300°C. The needle like precipitates are gone from the structure in both 10B and 15B samples.

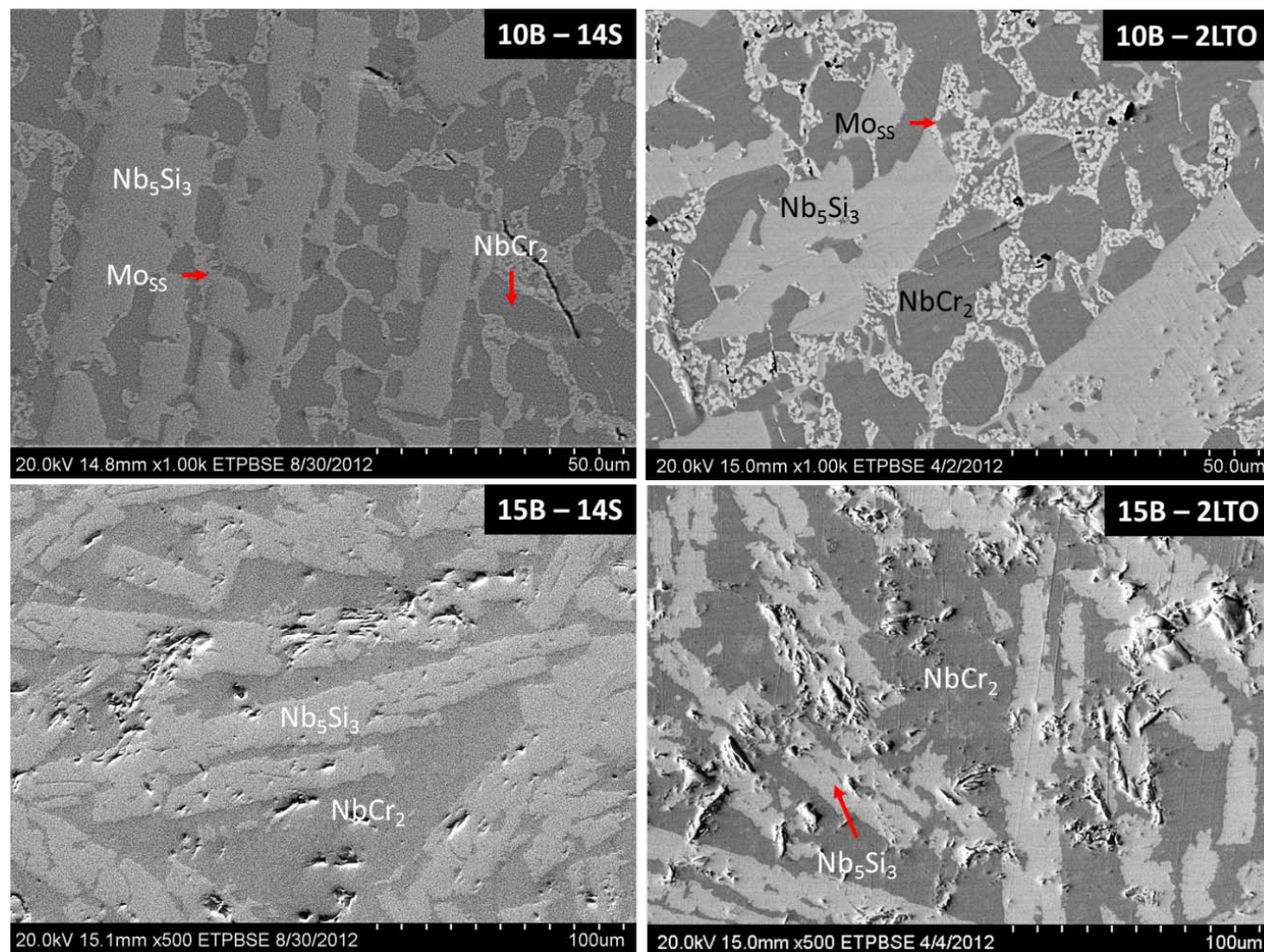


Figure 4.34: Microstructure morphology for the 10B and 15B samples during static and cyclic oxidation at 1300°C after 14 days of exposure.

Like the XRD diffraction patterns developed for the previous exposure periods, the samples at 1300°C reflect the primary oxides of Nb₂O₅ and CrNbO₄ as shown in Figure 4.35. The crystalline peak for SiO₂ is found in both the 10B and 15B samples at this temperature.

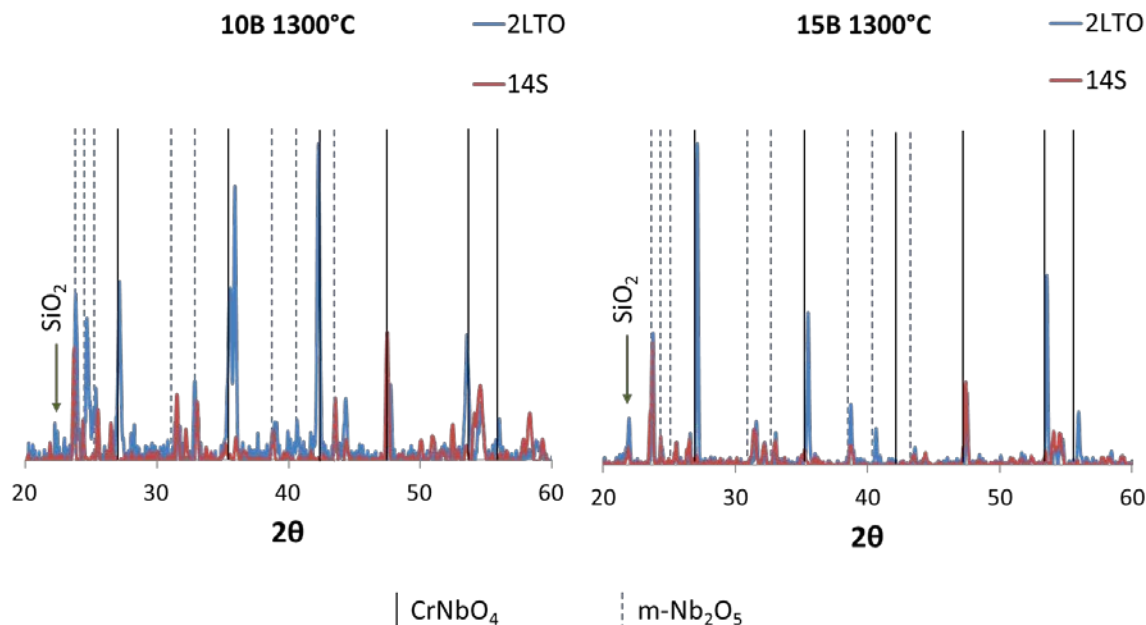


Figure 4.35: X-Ray diffraction results for 10B and 15B alloys after two weeks of cyclic and static oxidation at 1300°C, scans of the 14S sample is characteristic of those found for the successive static exposures.

The scales developed for the 10B and 15B alloy at 1300°C during static oxidation are shown in Figure 4.36 and the scales developed for the alloys during cyclic oxidation is shown in Figure 4.37. Both alloy scales contain CrNbO₄ and SiO₂ with Nb₂O₅ detected closer to the bulk metal at 1300°C. The 10B scale contains a wider IOL which is comprised of primarily Nb₂O₅, which coarsens with increased exposure periods. After 3 days of static oxidation the 15B alloy showed a crack along the interface between the bulk of the oxide and the IOL. The crack may have occurred during the cooling of the sample and be due to differences in coefficients of thermal expansion, however it is not present in the later exposure periods and may instead have been caused during sectioning and polishing. With the 15B addition at this temperature, the development of a near continuous SiO₂ layer is possible, as shown in the low-magnification composite image of the sample in Figure 4.38. The formation of the SiO₂ layer

appears to give the most oxidation resistance out of all the scales seen. The SiO_2 sections likely contain appreciable amounts of B_2O_3 allowing for the silicate/borosilicate to flow and provide a barrier to oxygen diffusion. Oxide thickness after two weeks of exposure for the 10B samples averaged $450\mu\text{m}$ for the static sample and $860\mu\text{m}$ for the cyclic sample.

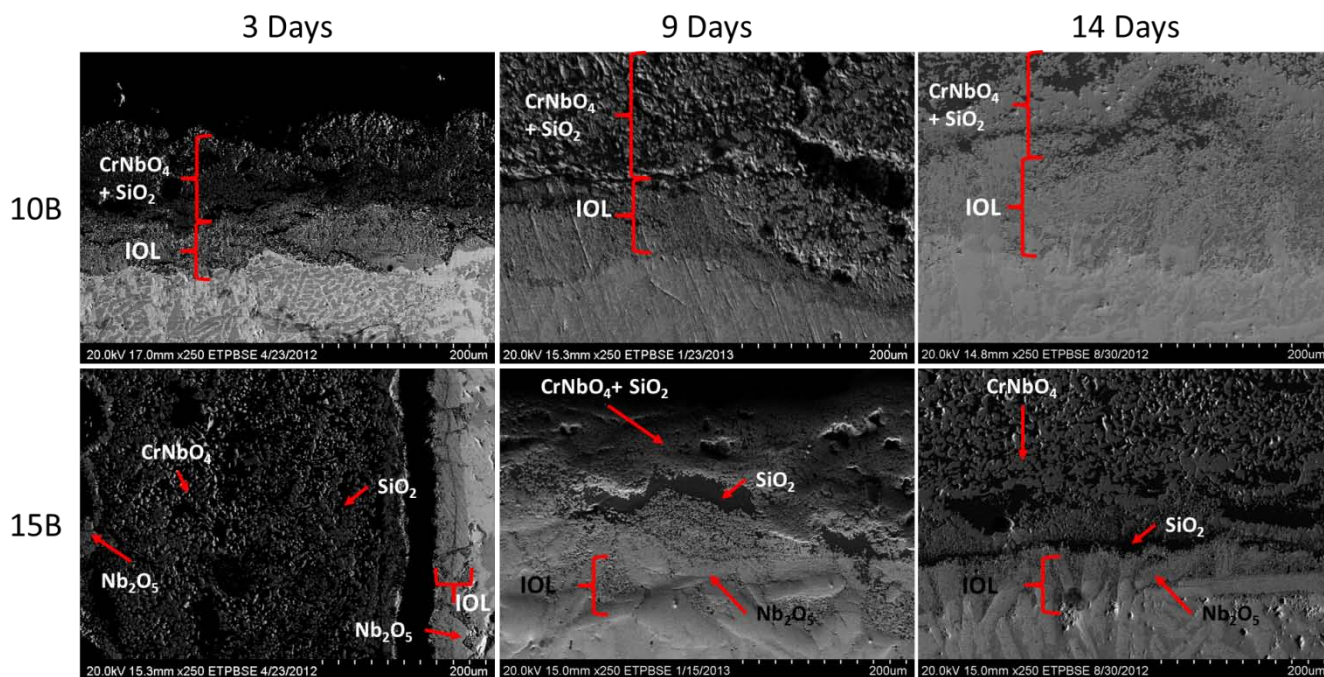


Figure 4.36: Oxide-metal interface developed at 1300°C after static oxidation for stated period of days for the 10 and 15B alloys.

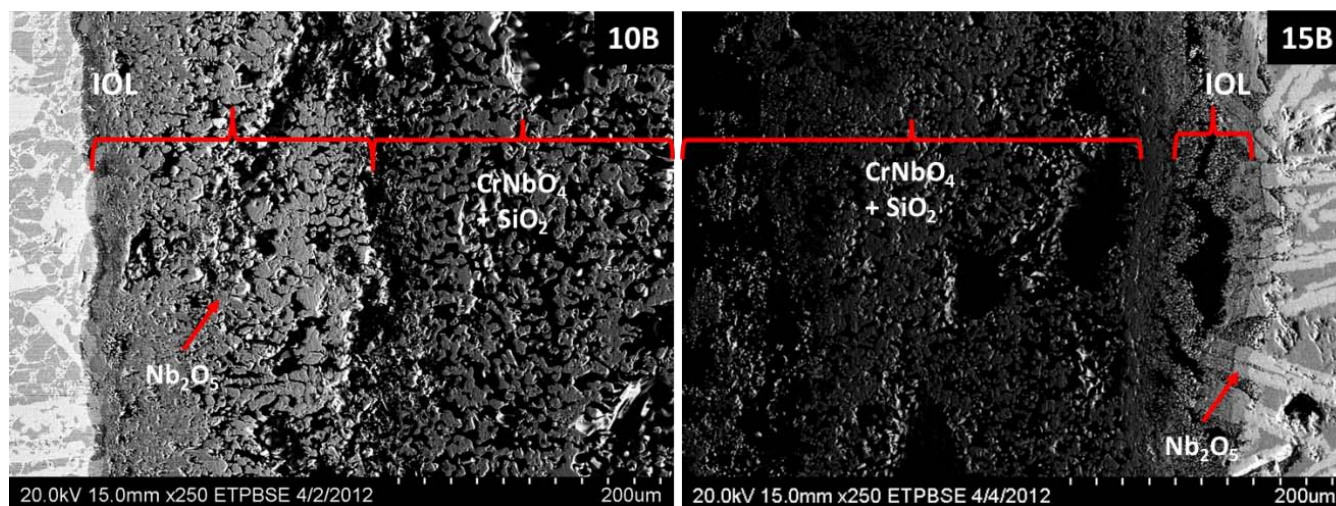


Figure 4.37: Oxide-metal interface developed at 1300°C after cyclic oxidation of 10 and 15B alloys.

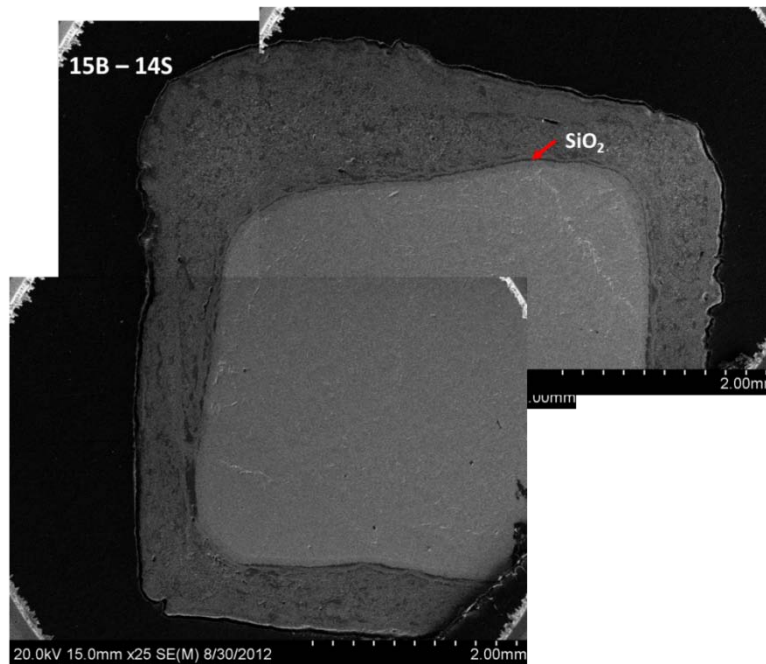


Figure 4.38 Composite images of the oxide developed for the 15B sample exposed at 1300°C after 14 days static oxidation.

A characteristic EDS scan shown in Figure 4.39 indicates the peaks for silicon, oxygen, and boron. While EDS scans cannot give an accurate quantitative measurement of boron content due to being at the edge of the detection window, the presence of the element must be taken into account, leading to the consideration of the layer as a borosilicate. With the larger weight gain achieved by the 10B sample over the 15B sample as previously discussed, the presence of the borosilicate/silicate layer may be one contributing factors in the prevention of further oxidation.

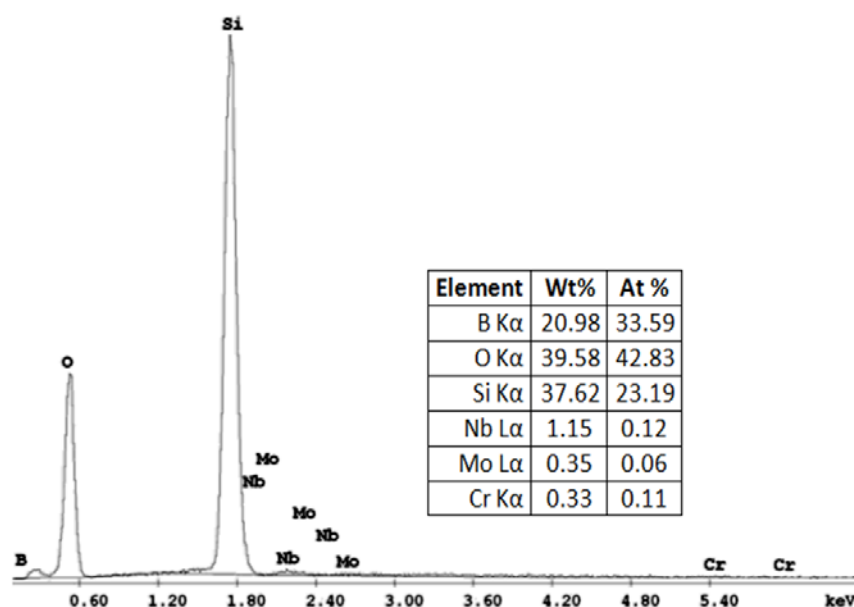


Figure 4.39: Characteristic EDS scan developed for the SiO₂ layer developed in the 15B alloy.

As indicated in the gravimetric results for the 15B sample, the 12 sample experienced catastrophic oxidation. Upon sectioning, no metal could be observed macroscopically. A composite image of the oxide is shown in Figure 4.40, a relatively thick formation of Nb₂O₅ was found at the oxide-air interface, while the majority oxide developed similar features to those found during other exposure periods but without any distinct SiO₂ layer, suggesting that the oxidation resistance of the alloy is dependent on favorable condition for the layers formation. The oxide becomes more porous closer to the center of the sample and, as indicated in Figure 4.41, near the center some un-oxidized NbCr₂ is found.

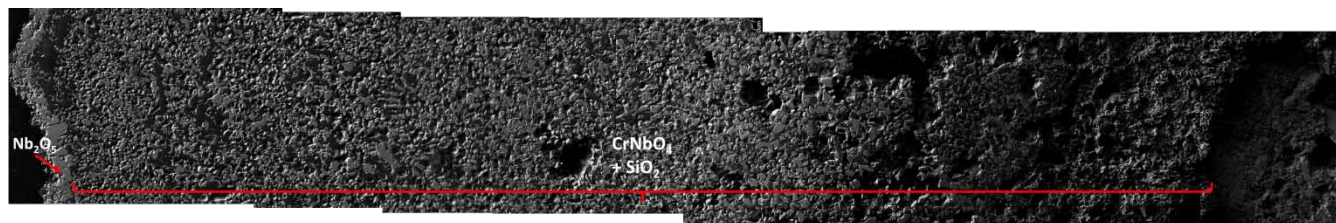


Figure 4.40: Composite image of the oxide developed for the 15B sample exposed at 1300°C after 12 days static oxidation.

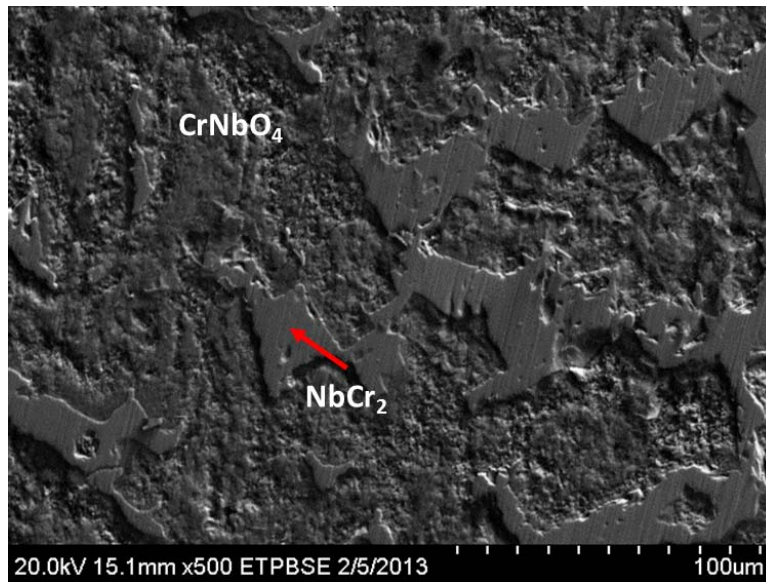


Figure 4.41: Un-oxidized NbCr_2 found near the center of the sample surrounded by CrNbO_4 .

4.2.3 Three Week Cyclic Oxidation

The 10B and 15B alloys were subjected to three weeks of oxidation wherein the samples were exposed in 3 day cycles to temperatures 700, 900, 1100, and 1300°C. The oxidation curves developed are presented in Figure 4.42. At 700°C samples tended to follow a linear oxidation behavior, while at higher temperatures the behavior is more parabolic. The data is consistent with the findings of the two week experiments, except for that of the 10B sample exposed at 1100°C, which shows a substantial increase in oxidation resistance. After sectioning, the base metal remaining showed no difference in morphology change from the samples exposed for two weeks. The 10B samples developed the Mo_{55} precipitates at 900 and 1100°C as well as the eutectic like structure as shown in Figure 4.43. The 15B sample maintained the two phase morphology across all temperatures as shown in Figure 4.44. The XRD data obtained for the alloys remains consistent with all previous exposures, it is presented in Figure 4.45; oxides identified remain as CrNbO_4 and monoclinic Nb_2O_5 .

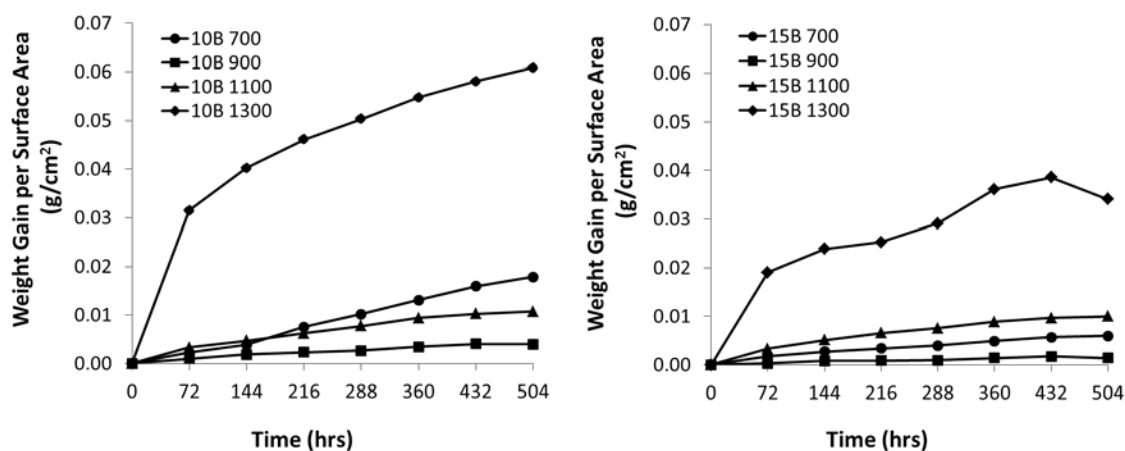


Figure 4.42: Gravimetric curves developed for the 10 and 15B alloy after three weeks of cyclic oxidation.

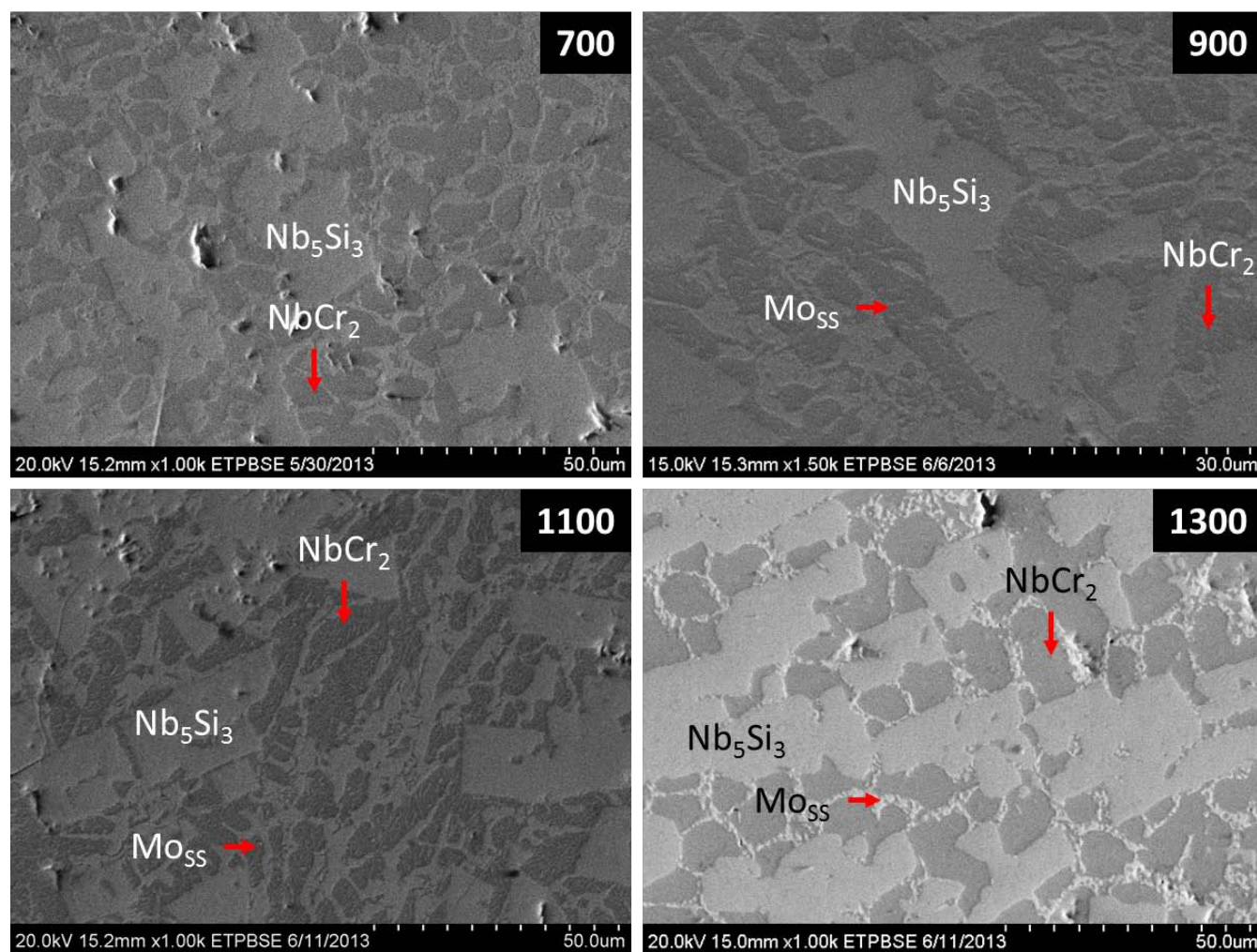


Figure 4.43: Morphology of the 10B alloy with temperature during three week cyclic oxidation.

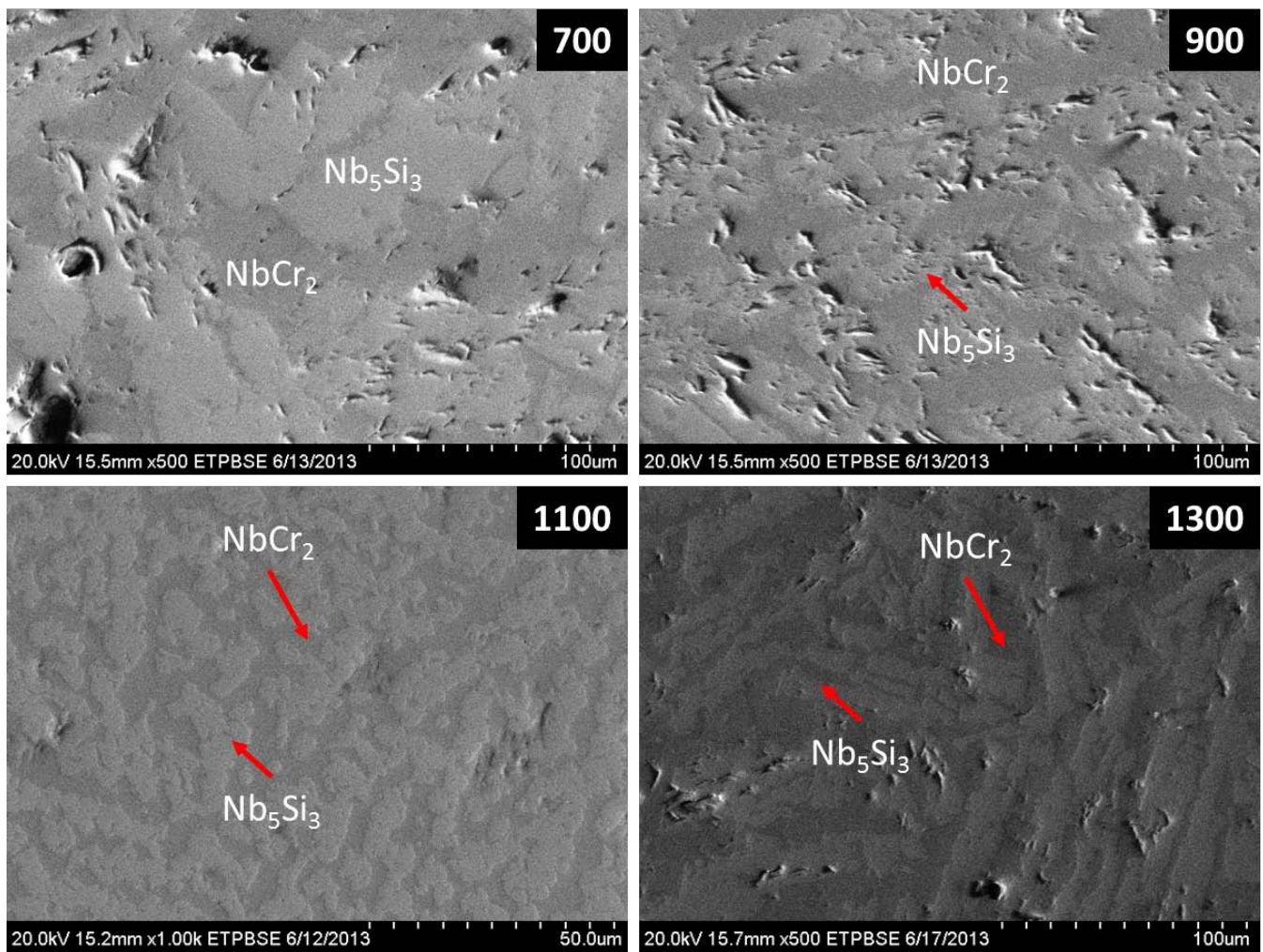


Figure 4.44: Morphology of the 15B alloy with temperature during three week cyclic oxidation.

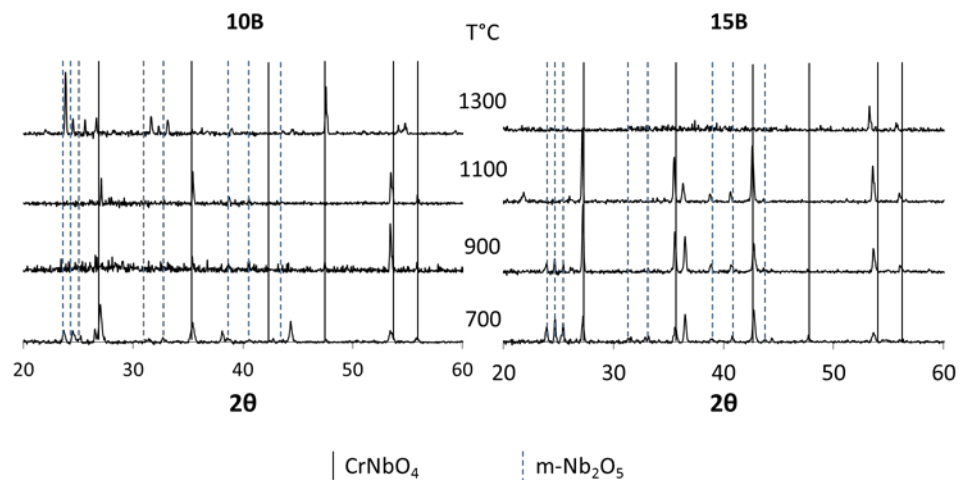


Figure 4.45: XRD patterns developed for the 10 and 15B alloys during three week cyclic exposure.

Upon SEM analysis of the samples, many similar features to the samples exposed in the shorter periods of time were observed. Examination of the oxide surface reveals that for the 10B samples at 700°C a very granular oxide is developed as compared to that of the 15B sample, as shown in Figure 4.46 with the corresponding oxide metal interface, though both are primarily Nb_2O_5 . This difference in surface morphology is reflected in the cross section of the oxide metal interface with the 15B sample showing more compact oxide growths.

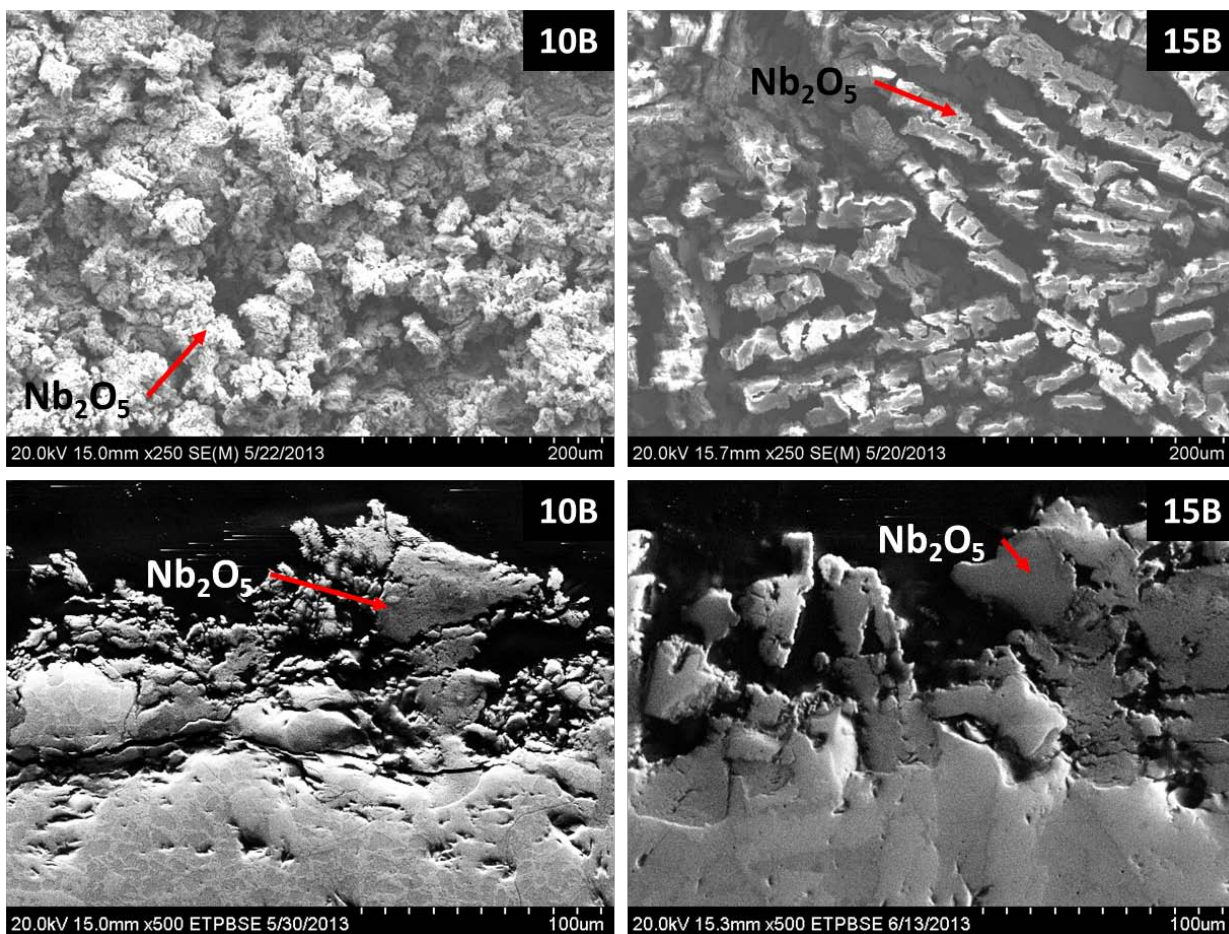


Figure 4.46: Oxide surface and oxide metal interface developed for the 10B and 15B alloys at 700°C.

The surface of the oxides for the samples at 900°C and the oxide metal interface are shown in Figure 4.47. The Nb_2O_5 growths of the 10B sample retain some of the granular like formation as visible in the image at 1000X, though they do not fall away from the surface due to the SiO_2 they form in conjunction with, a layer of CrNbO_4 is present at the surface. For the 15B the surface is detected almost

completely as CrNbO_4 , save for the rod like structures of Nb_2O_5 visible at higher magnifications, these formations are likely very fragile so they do not survive the sectioning and polishing step to be found in the interface.

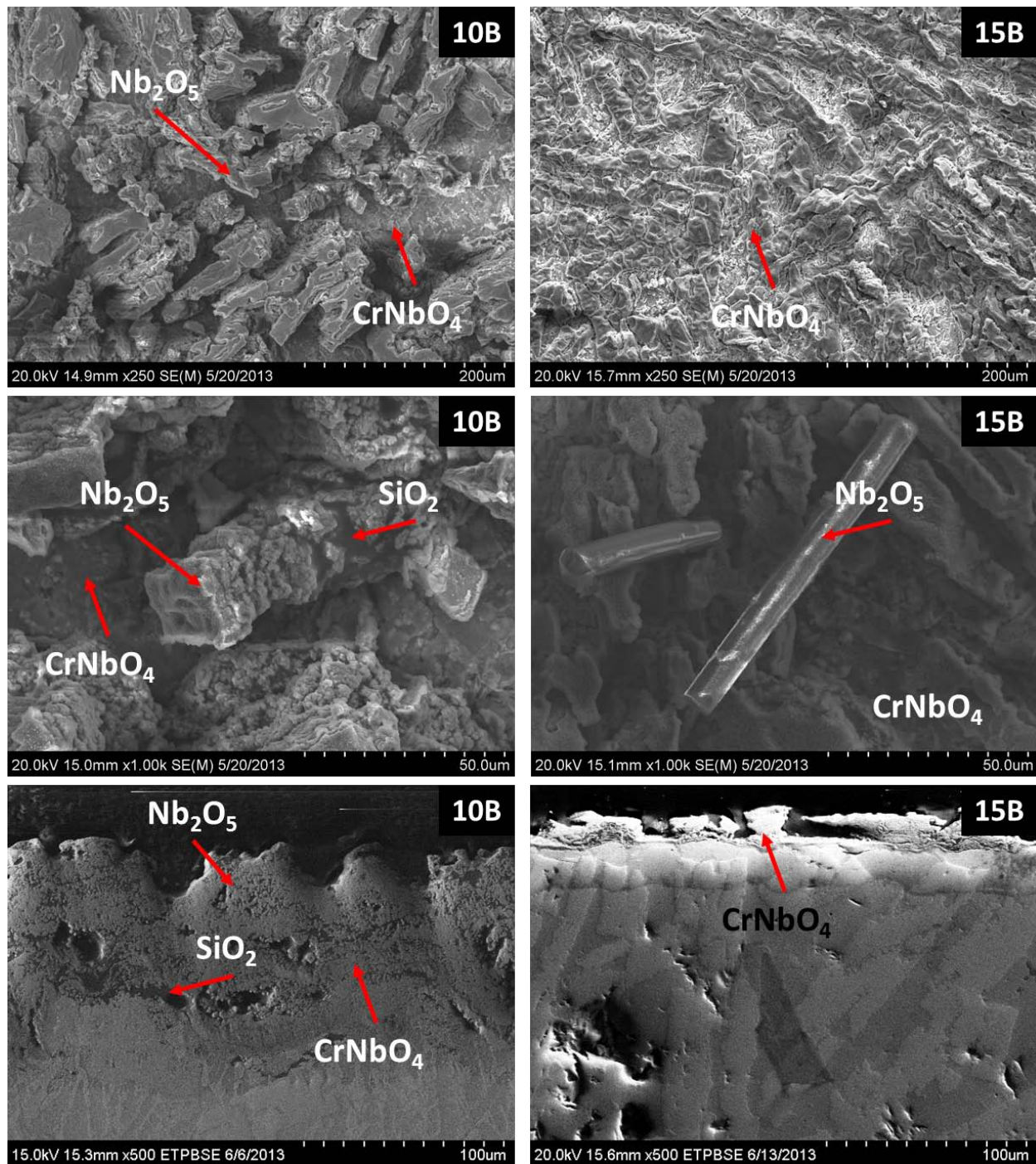


Figure 4.47: Oxide surface and oxide metal interface developed for the 10B and 15B alloys at 900°C.

For the 10B and 15B samples exposed at 1100°C the oxide surface and oxide metal interface are shown in Figure 4.48. The CrNbO_4 of the 10B is more substantial at 1100°C with the addition of small bubbles of SiO_2 , and Nb_2O_5 is still detected at the surface. The surface of the 15B oxide is entirely CrNbO_4 , none of the rod-like formations of Nb_2O_5 are found at the surface. The likely reason for the increase in resistance for the 10B sample at this temperature is found in the oxide-metal interface where the CrNbO_4 forms a near continuous layer as is detailed in the EDS map of Cr. Isolated instances of Cr_2O_3 were detected in the 10B scale, while it was nearly a continuous layer in the 15B scale. The CrNbO_4 is a superior barrier to oxidation than that of Nb_2O_5 as the 15B has consistently shown at this temperature regime. The region of Cr depletion in the 10B sample is very thin compared to that of the 15B sample, which has a fully developed IOL.

For the 10B and 15B samples exposed at 1300°C the surface and full cross section of the scale are shown in Figure 4.49. For the 10B sample the surface of the oxide is identified as only Nb_2O_5 which corresponds to the thick outer layer present in the scale, below which the scale reverts to a bulk of CrNbO_4 and SiO_2 . The 10B scale did not achieve a uniform width, ranging from 350µm to 600µm. The 10B alloy does not form a continuous layer of SiO_2 though there are large isolated regions of it in the scale. At the oxide metal interface for the 10B alloy, Figure 4.50, it can be seen that there is a layer of Mo enrichment, some of which is likely MoO_3 , also visible is the formation of silica within the IOL and in the sub scale. For the 15B sample the oxide surface remains CrNbO_4 as in the 1100°C sample and the bulk of the scale is CrNbO_4 and SiO_2 . At the interface, detailed by the EDS maps in Figure 4.51, the silica layer is near continuous, above which Cr enrichment leads to Cr_2O_3 formation. Below the silica layer, Cr depletion, Mo and Nb enrichment form the IOL, there is no sign of silica formation below the IOL unlike in the 10B sample.

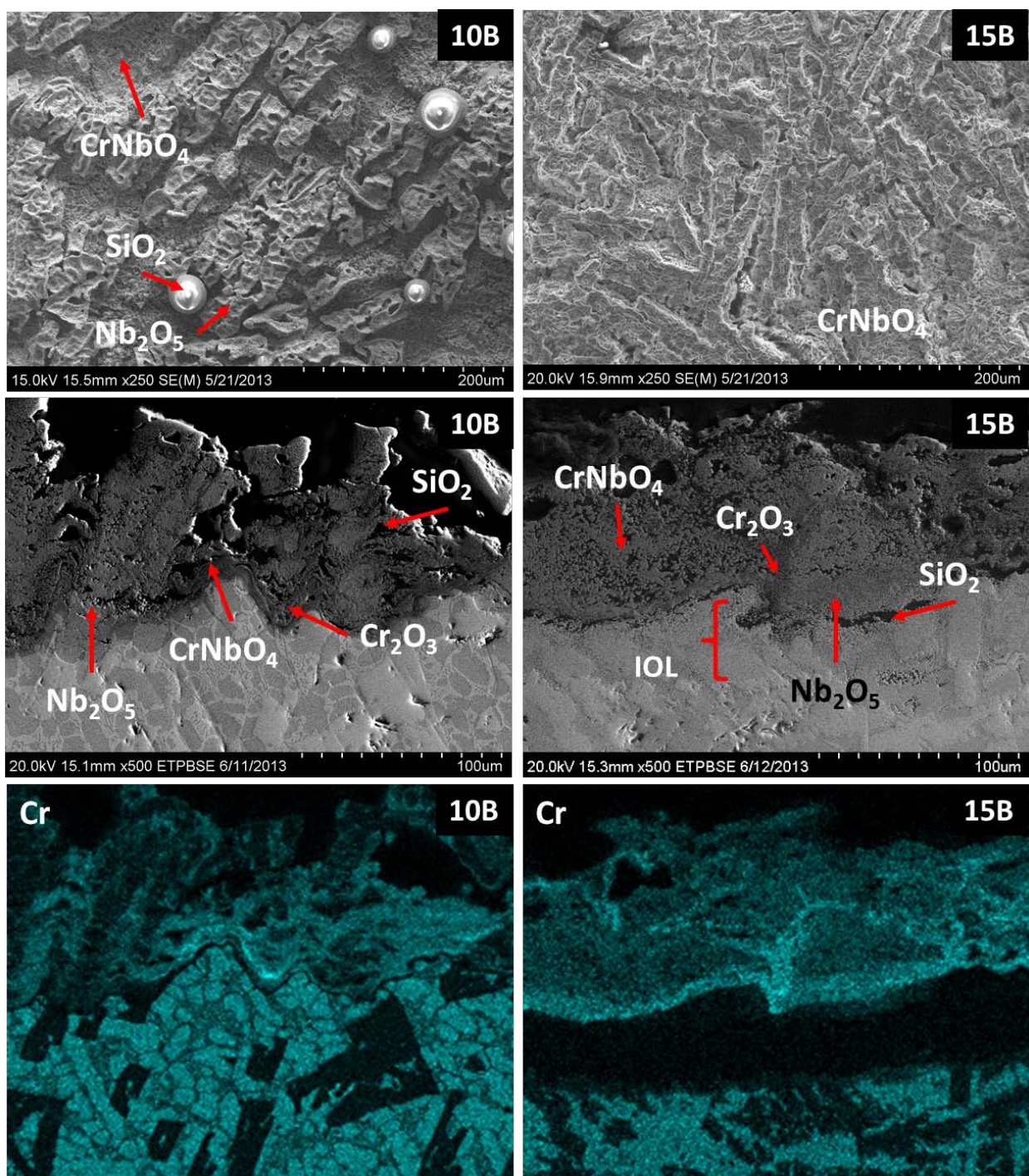


Figure 4.48: Oxide surface and oxide metal interface developed for the 10B and 15B alloys at 1100°C and EDS map of Cr.

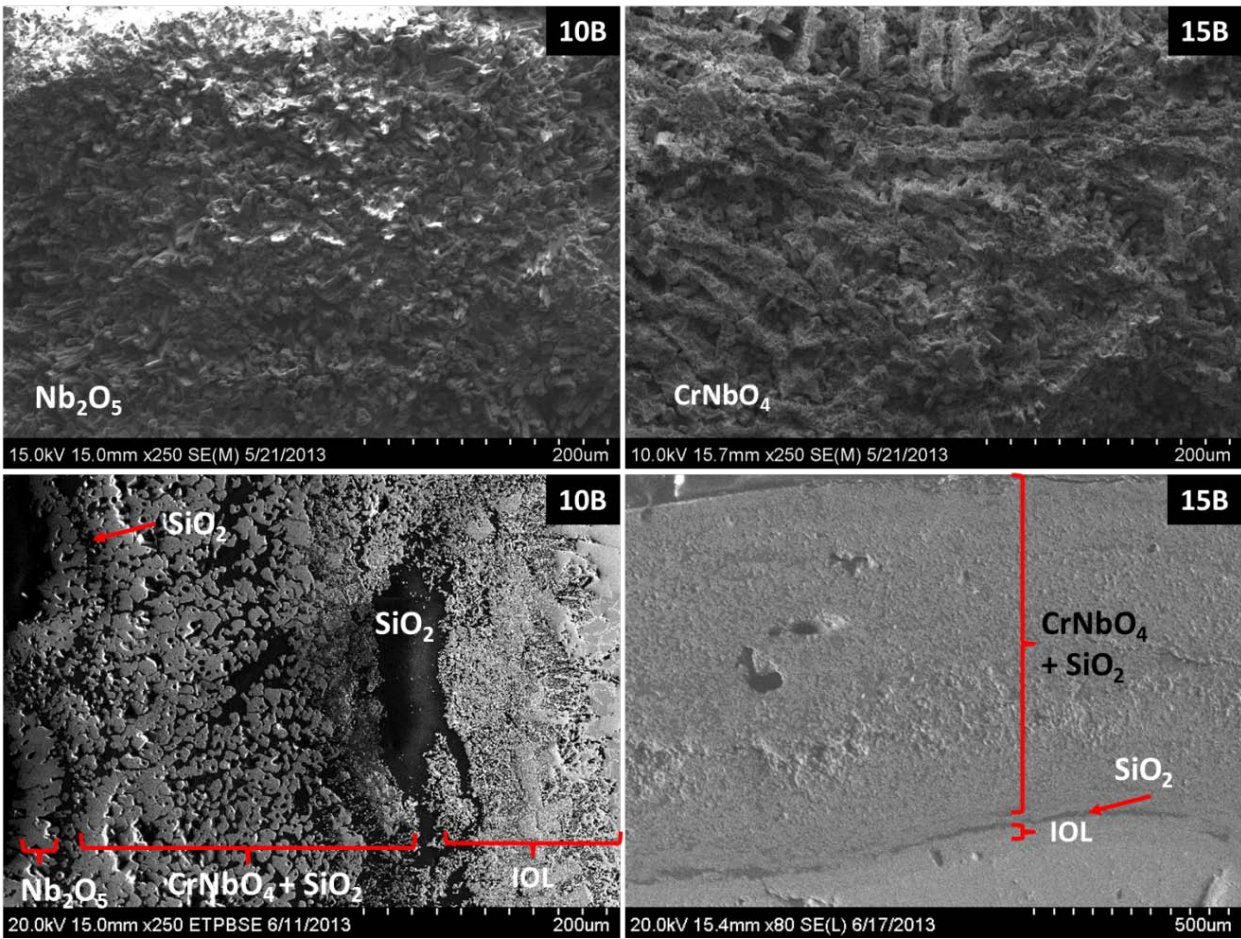


Figure 4.49: Oxide surface and cross sectional micrograph of full oxide scale developed for the 10B and 15B alloys at 1300°C.

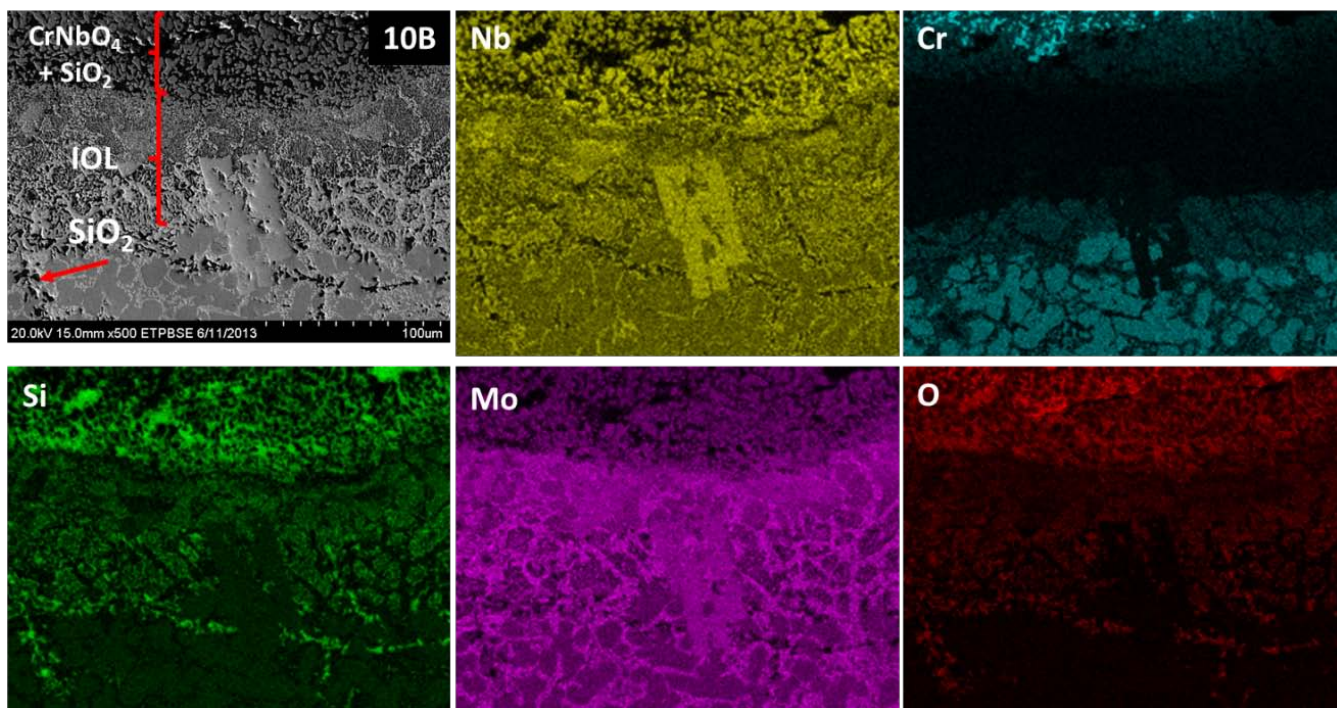


Figure 4.50: EDS map of the oxide metal interface developed for the 10B alloy at 1300°C.

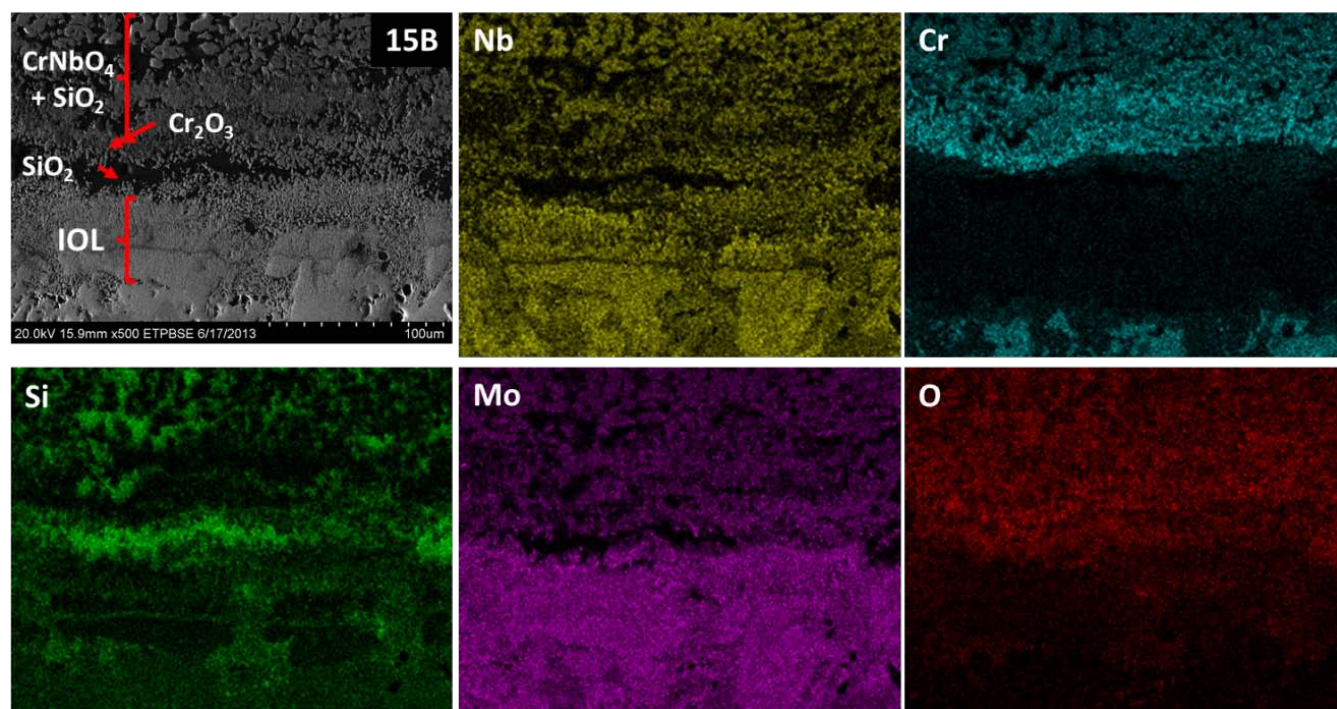


Figure 4.51: EDS map of the oxide metal interface developed for the 15B alloy at 1300°C.

4.3 OXIDATION OF 15Mo CONTAINING ALLOYS

The investigation into the three alloys with compositions of Nb-25Cr-15Mo-15Si-15B, Nb-25Cr-15Mo-20Si-15B, and Nb-25Cr-15Mo-20Si-10B in atomic percent will help to widen the understanding of the oxidation behavior for this system. The alloys here were developed with three questions in mind:

(1) The effect of boron for the Nb-25Cr-15Mo-20Si-xB system where the comparison will be drawn between the 2010 and 2015 alloys and the previously mentioned alloy studied by Portillo. Similar to the work for the Nb-25Cr-20Mo-15Si-xB the creation of a borosilicate layer found in the Mo-Si-B studies by various teams is a desirable result. However, while such a protective layer was not developed in the previous works, the increase in boron had a notable effect on the oxidation resistance of the alloys across the temperature range to a significant extent.

(2) The Mo/Si ratio effect will be studied for the 10 and 15B concentrations, the ratio has been inverted from the current alloys to the new set of alloys such. Raising the Si content is hoped to promote the formation of a more continuous layer of SiO_2 as found in the 15B alloy. The effects of reducing the molybdenum content may relate to the permeability of the scale to oxygen due to vacancy creation and the formation of precipitates within the microstructure.

(3) The Mo effect will be examined for the Nb-25Cr-(15, 20)Mo-15Si-15B alloy to identify whether the silica layer that formed in the high temperature regime could be repeated at a lower Molybdenum content. Molybdenum is the most notable volatile oxide in the study and some porosity still present in the high temperature scales; this can possibly be reduced with the Mo content. With the possibility that it influences the bulk scale to contain vacancies when in a solid solution with CrNbO_4 , vacancy reduction may also be possible to reduce ion mobility within the scale.

4.3.1 As-cast Characterization

The results for the x-ray diffraction of the as-cast alloys are presented in Figure 4.52. Like the 10B and 15B alloys, none of the alloys showed reflections for a solid solution of either niobium or molybdenum, nor the ternary phases predicted in the room temperature isothermal section. Common to the alloys were the NbCr_2 Laves phase with the C14 structure and the $\beta\text{-Nb}_5\text{Si}_3$ silicide. The 2010 and 2015 sample showed peaks for a second silicide, with the structure of Mo_3Si . Like the 5-3 silicide it is likely that rather than being a pure Mo_3Si phase it is rather of a $(\text{Nb}, \text{Mo})_3\text{Si}$.

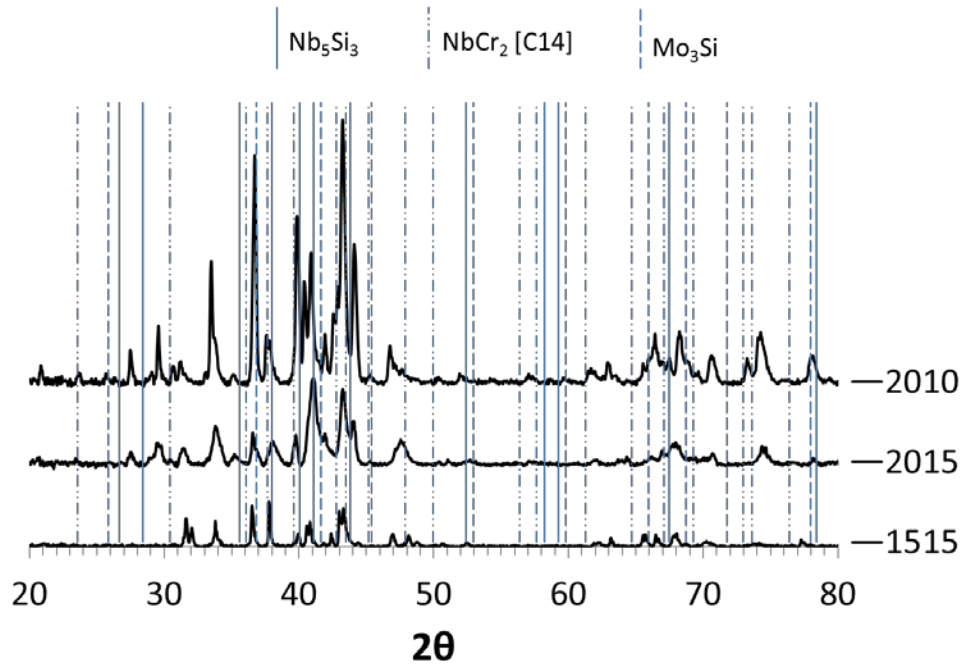


Figure 4.52: XRD results for the as-cast state of the 1515, 2010, and 2015 alloys.

Figure 4.53a and b shows the microstructure observed for the 1515 alloy at 250X and 1000X magnification. The distribution of elements obtained through x-ray mapping (Figure 4.54) enabled identification of the phase regions as the dark grey region corresponding to the NbCr_2 Laves phase. While the bulk of the 1515 alloy is similar to that of the 10B and 15B alloys, the Laves phase is interspersed with what is identified as a Mo-rich Nb_5Si_3 . The reflection of boron is not present in the

EDS maps due to detector limitations. Like the 15B alloy the matrix phase appears to be the Laves phase.

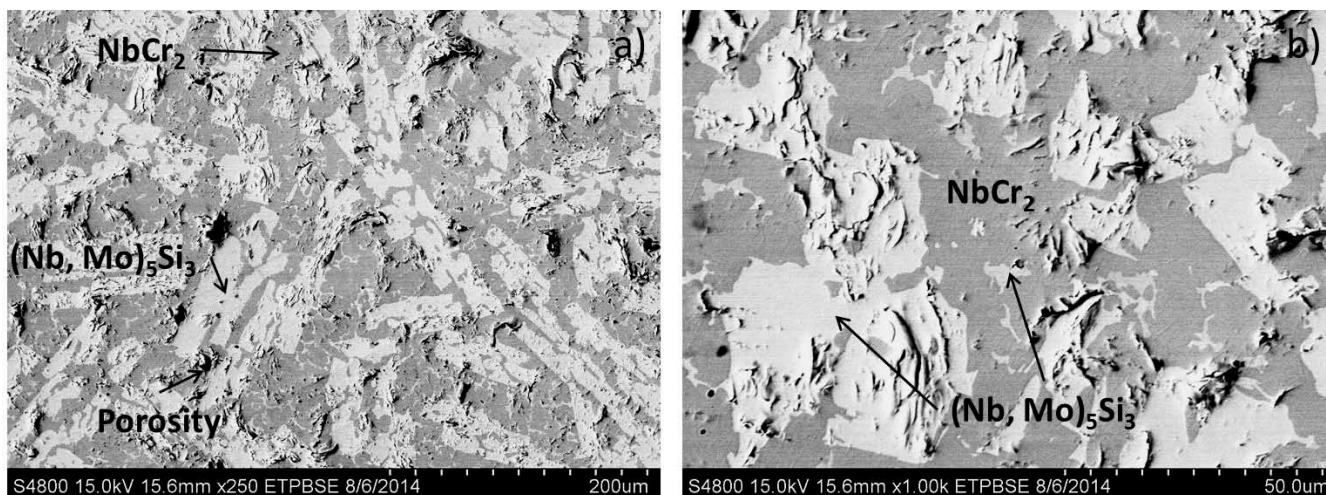


Figure 4.53: As-cast microstructure of the Nb-25Cr-15Mo-15Si-15B alloy at (a) 250X and (b) 1000X magnification.

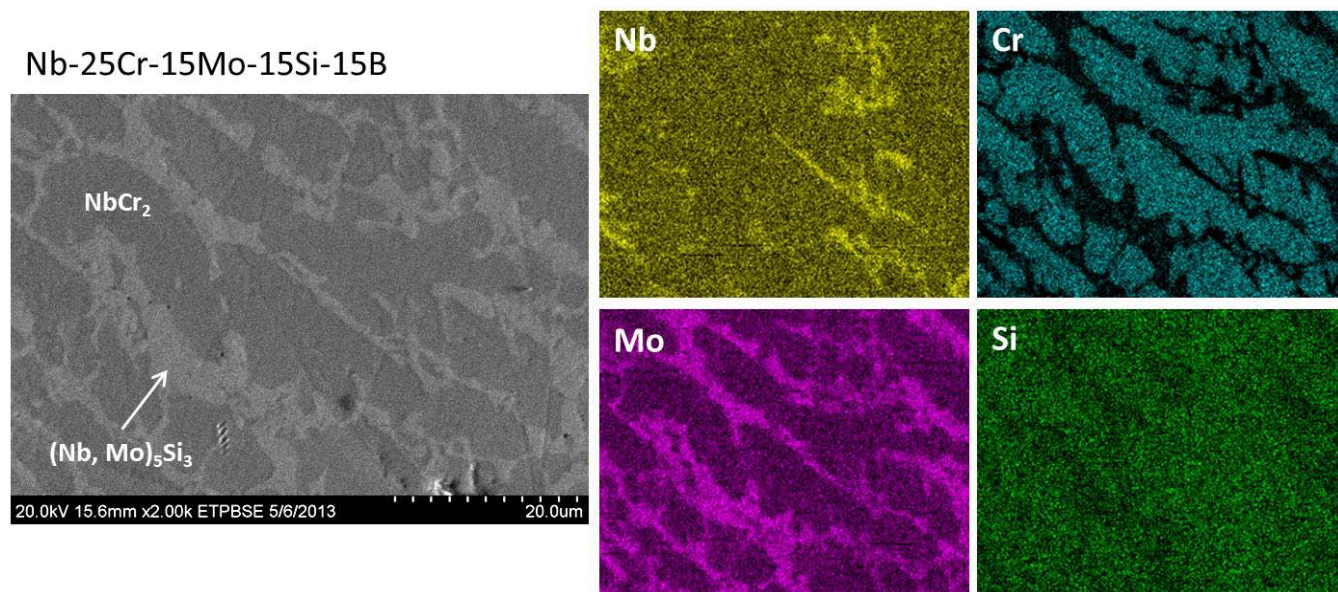


Figure 4.54: EDS mapping of the 1515 alloy.

Figure 4.55a and b shows the microstructure of the 2010 alloy at 250X and 1000X magnification. The microstructure contains three distinct phases as shown in the micrograph with elemental mapping of the sample shown in Figure 4.56. Two silicides are present in the 2010 sample, confirmed by XRD results, previously indicated. The silicides are delineated by their silicon content,

where it is higher in the $(\text{Nb}, \text{Mo})_3\text{Si}$ with a brighter reflection in the EDS maps, which corresponds to the light grey regions in the microstructure. The medium grey areas within the micrograph are the 5-3 silicide for this alloy, unlike the 2015 sample, the 5-3 silicide does not contain as wide a compositional variance. The dark grey region remains the NbCr_2 Laves region. Regarding the increase in boron from the alloys investigated by Portillo, the as cast microstructure has lost the eutectic like structure containing solid solution and silicide for both the 2010.

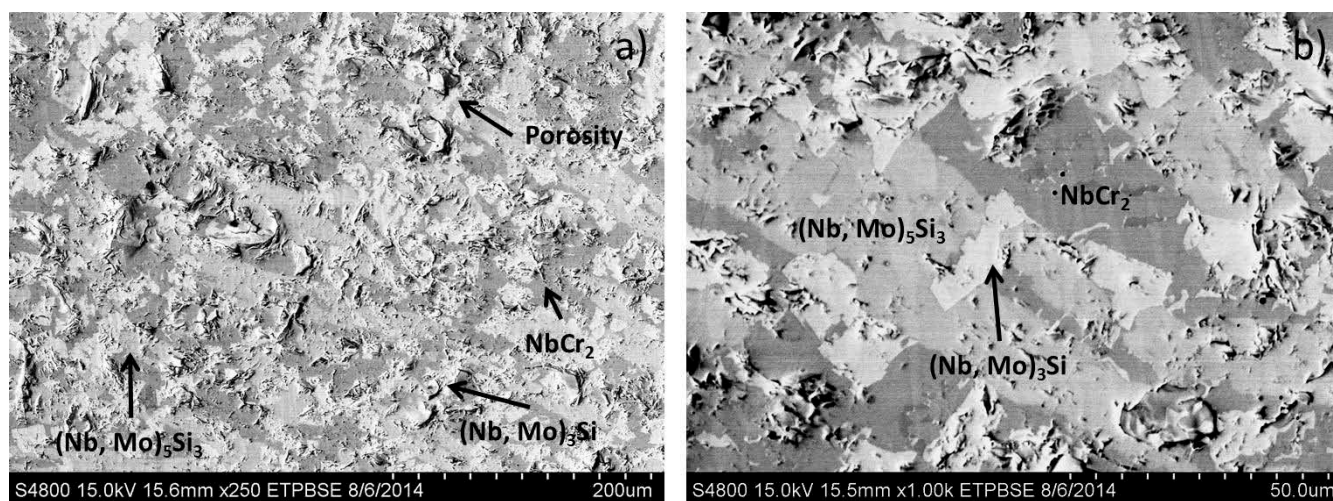


Figure 4.55: As-cast microstructure of the 2010 alloy (a) 250X and (b) 1000X magnification.

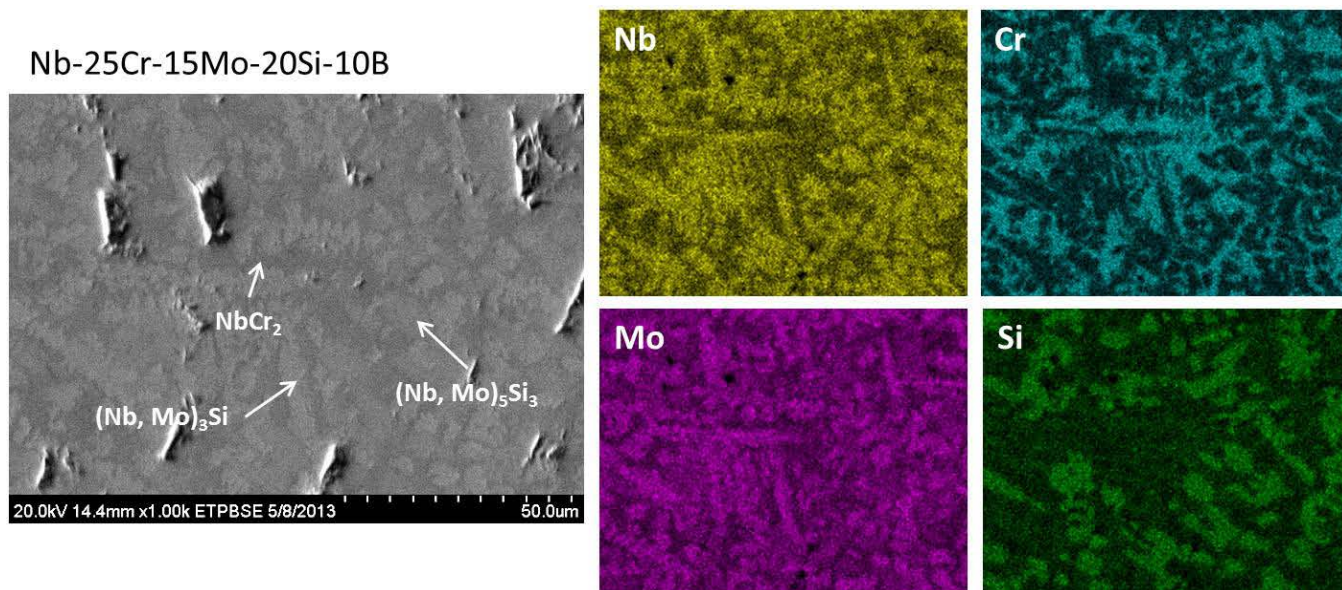


Figure 4.56: EDS mapping of the 2010 alloy.

Figure 4.57a-d shows the microstructure observed for the 2015 alloy. Figure 4.57a shows the fine microstructure obtained for this composition, with the phases indicated in Figure 4.57b. The micrographs of 4.57c and d show a magnified view of 4.57b, detailing the differences in backscatter and secondary. Under secondary imaging, the 5-3 silicide appears as a single phase structure, while in backscattered image the 5-3 silicide appears as a two-phase region. X-ray mapping shown in Figure 4.58 shows that the 5-3 silicide contains a variable amount of niobium, with a higher percentage in the central regions of the grain. A second $(\text{Nb}, \text{Mo})_3\text{Si}$ silicide is present within the microstructure as the light grey region. The 2015 alloy is the only one of the three alloys to contain a eutectic like region in the as-cast state. The dark grey microconstituent within the eutectic like region corresponds to the Laves phase.

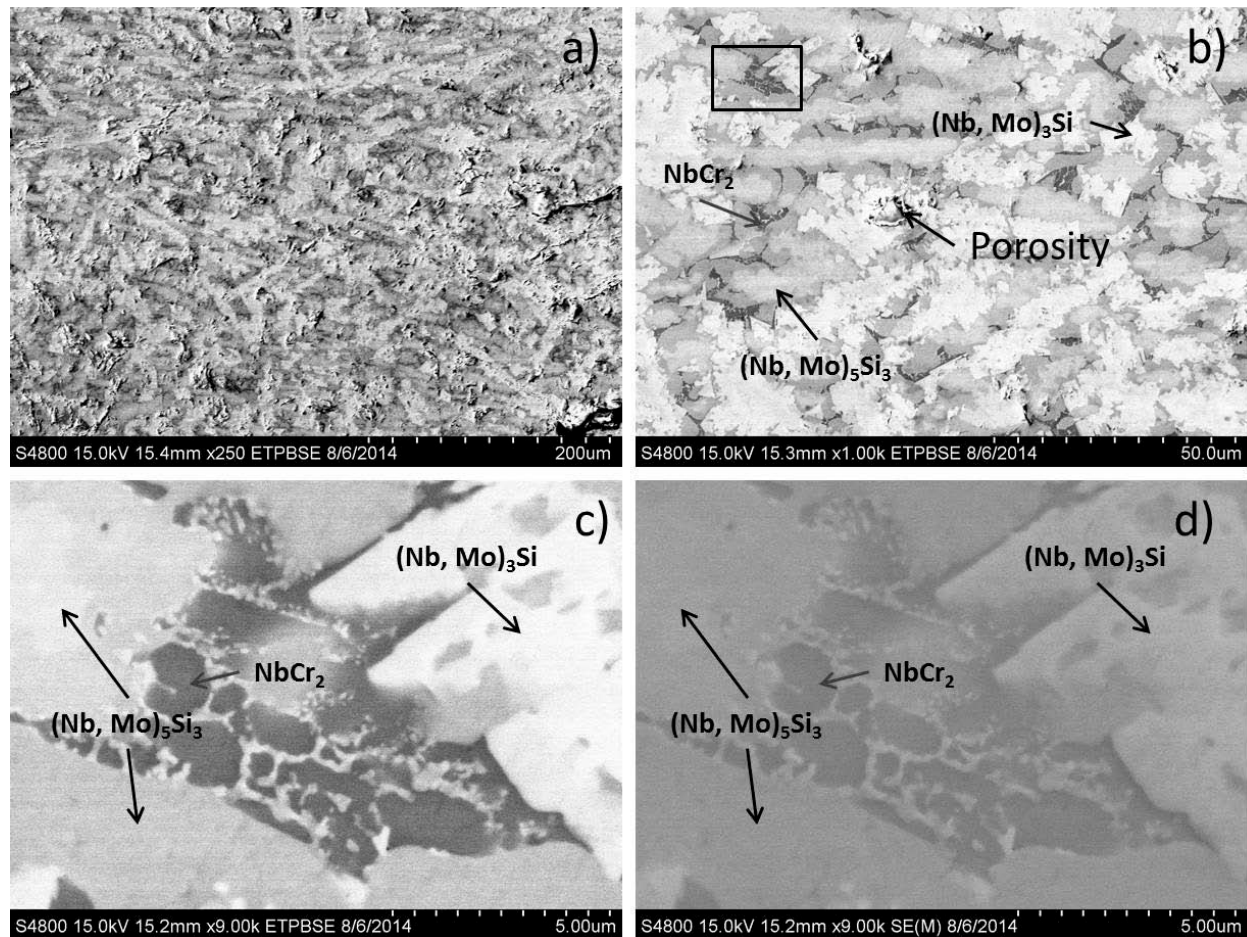


Figure 4.57: As-cast microstructure of the 2015 alloy at (a) 250X and (b) 1000X magnification, magnified view of indicated region in (c) backscatter and (d) secondary imaging.

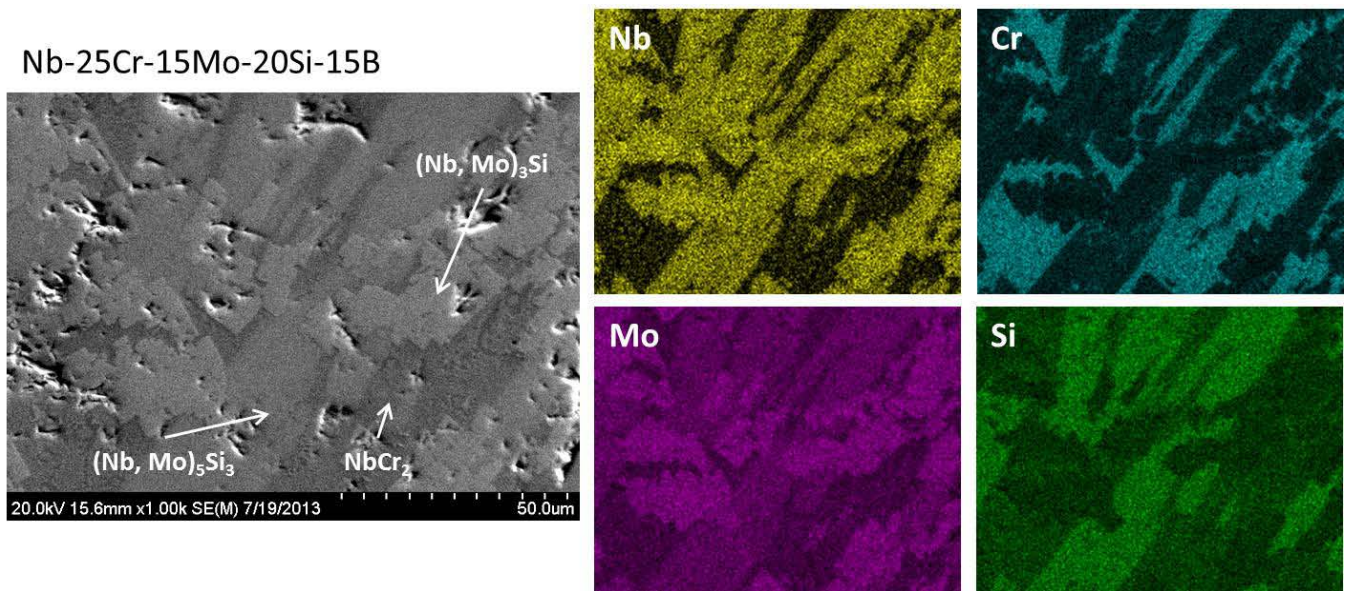


Figure 4.58: EDS mapping of the 2015 alloy.

Image analysis was carried out on the as cast microstructures of the 15Mo alloys to be compared with the 10B and 15B alloys, results are presented in Table 4.3. Similar to the 10B and 15B alloys the 1515 alloy contains a nearly even distribution the Laves phase and the 5-3 silicide. With the error associated with estimating the volumetric ratio from an area, the increase in Laves phase is likely within the margin of error. The 2010 and 2015 alloys however show a large reduction in the amount of Laves phase present within the alloy, this should reflect in an increase in room temperature strength.

Table 4.3: Phase fractions calculated for as-cast state of alloys at 1000X.

Alloy	NbCr ₂ Laves	5-3 Silicide	3-1 Silicide
10B	46	54	0
15B	51	49	0
1515	52	48	0
2010	38	35	27
2015	25	53	22

Considering the increase in silicon from 15 to 20 at% there is a notable increase in the fraction of silicides within the alloy and the presence of the secondary silicide. According to the phase diagram for

Nb-Si [53], Nb_3Si forms from a peritectic reaction from the liquid and $\beta\text{-Nb}_5\text{Si}_3$ and then the low temperature $\alpha\text{-Nb}_5\text{Si}_3$ is developed through the peritectoid reaction between the Nb_3Si and $\beta\text{-Nb}_5\text{Si}_3$ silicides. As previously stated, the addition of Mo and B can stabilize the β -structure, however due to the increase in Si content Nb_3Si is in excess and remains present in the as cast structure. No boride compounds were developed in the alloys despite the high atomic percentage. The boron content does fall within the previously mentioned solubility range of the Nb_5Si_3 silicide and is likely to be stabilizing the β -structure. The reduction in the percent of Laves phase is likely to have a negative effect on the oxidation resistance but an increase in the room temperature strength.

4.3.2 Short Term Oxidation

Results from the short term (24 hour) oxidation are presented in Figure 4.59, including data for the 10B and 15B samples for comparison. The low temperature (700-900°C) samples had very fragile oxides that would result in small granules of oxide remaining in the vial after removal from the crucible. Initial observation of the short term oxidation results indicate that comparable weight gain responses were obtained for all alloys in low to upper mid-range (700-1200°C) temperatures, with the 10B alloy performing slightly better than all others. In all cases pest oxidation was not observed. In the high temperature range (1300-1400°C) the larger weight gains for the 20Si containing alloys is observed while the 15Si alloys show weight loss at the highest temperature exposure. For the effect of B on the Nb-25Cr-15Mo-20Si-xB samples, the response to short term oxidation has improved significantly at 700°C as the 5B alloy studied by Portillo suffered pest oxidation which is not observed in the 2010 and 2015 alloy. This behavior has been achieved through the control of the α -(Nb, Mo) solid solution, which is detrimental to the oxidation resistance of the alloys at low temperatures.

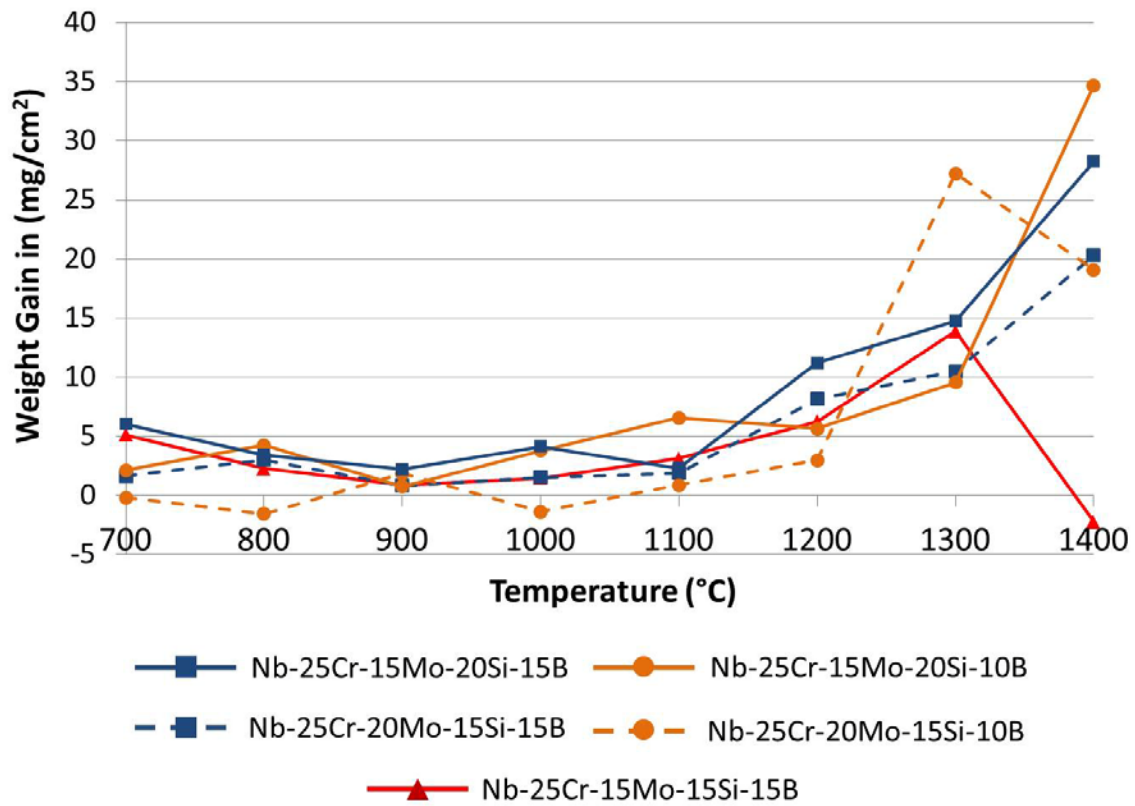


Figure 4.59: Gravimetric curves for short term oxidation of the alloys developed after 24 hours of exposure at each specified temperature.

Macro images of the samples after removal from the furnace are viewed in Figure 4.60, up to 1300°C samples maintained their dimensions, at 1400°C for the 1515 and 2010 samples bulky oxide formation is visible on some sections of the sample. The 1515 sample at 700°C was the only sample to show signs of a powdery oxide, with a minimal amount remaining in the crucible, otherwise the scales of the samples were well adherent in all cases. The 2010 sample at 1100°C contained a surface crack prior to oxidation, which did not initially appear to go all the way through the volume, however when removed from the furnace the sample was in two pieces suggesting that as the sample oxidized the crack was forced open. After sectioning it was observed that nearly 99-100% of metal remains for the exposures up to 1200°C.

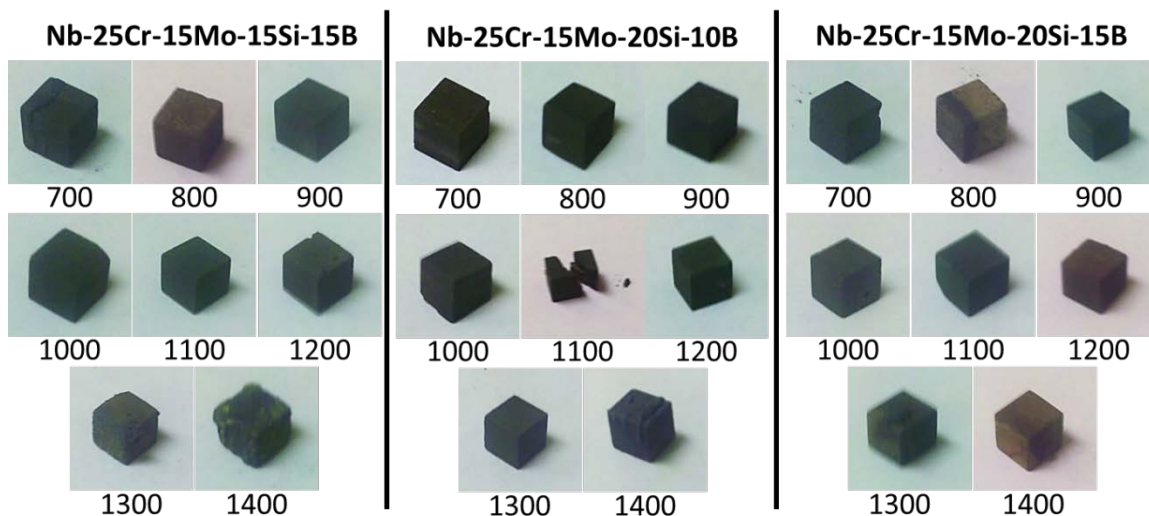


Figure 4.60: Macro images of samples after 24 hours oxidation at indicated temperature.

The results from x-ray diffraction for the alloys after short term oxidation are presented in Figure 4.61. The highest intensity SiO_2 peak is noted, it exists within the scale in its amorphous state at low temperatures therefore the crystalline peaks are only observed in the higher temperature regimes. As has been common for Nb-Cr containing alloys CrNbO_4 is present in all scans and increases in intensity with higher temperatures. From 700-900°C, Nb_2O_5 is detected though the intensity of the reflected peaks is very low compared to that of CrNbO_4 .

No microstructural variations from the as-cast state were observed for the samples after the 24 hour period of exposure. Morphology of the developed scales is similar to the previous alloys, as is shown in Figures 4.62 and 4.63. At low temperatures (700-800°C) the scale contains large growths of Nb_2O_5 and SiO_2 and a thin layer of CrNbO_4 , the 1515 alloy shows some un-oxidized NbCr_2 that has separated from the bulk of the metal. As the Nb_2O_5 forms from the silicides, the size of the growths is dependent on the grain size, as is visible in comparing the 1515 and the 2015 to the 2010 sample. From 900 to 1000°C CrNbO_4 forms a thin continuous layer. From 1100 to 1400°C the oxide scales develop a continuous CrNbO_4 and SiO_2 layer that coarsens as temperature increases Nb_2O_5 is present at the oxide-

metal interface. The scale contains porosity in the higher temperatures. What can be related to the IOL that is formed in the 10B and 15B is found in the samples exposed at 1400°C.

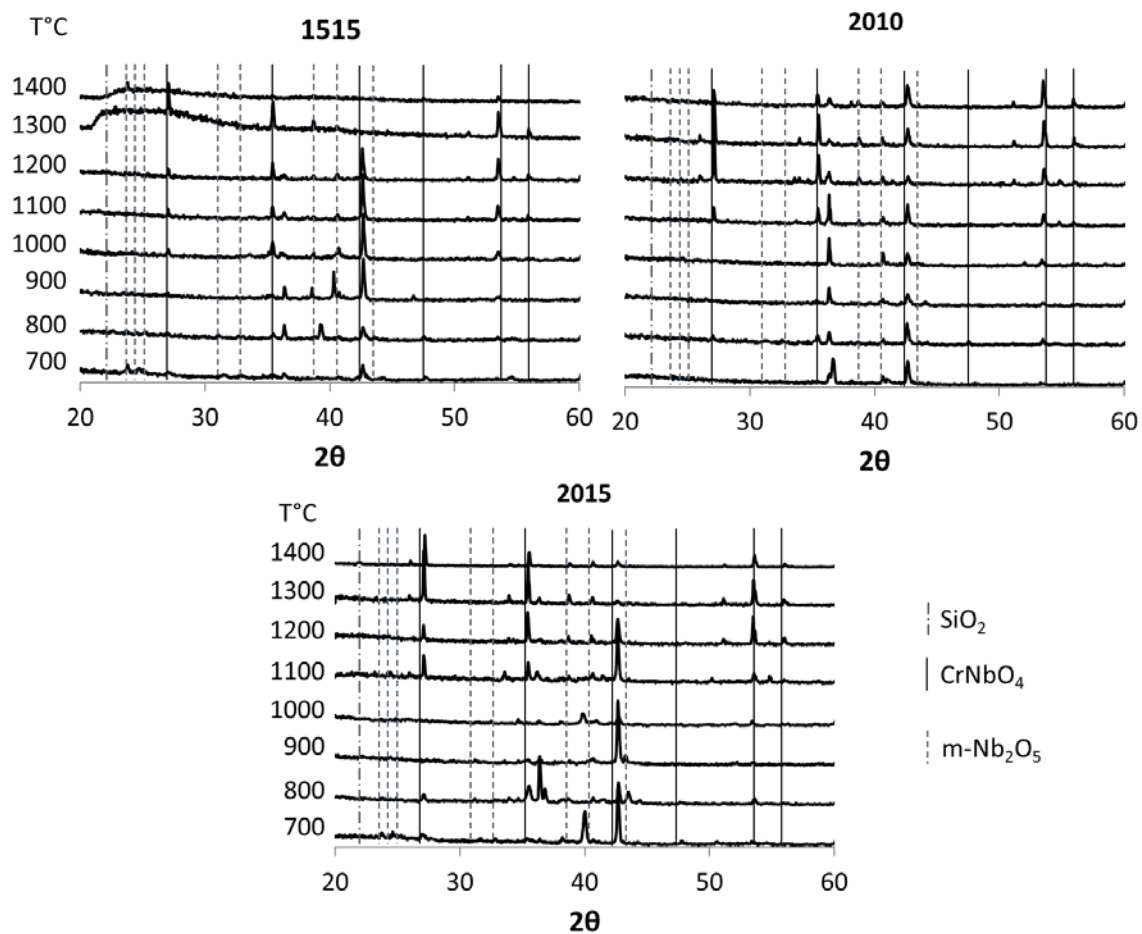


Figure 4.61: XRD patterns obtained for the alloys after 24 hours oxidation.

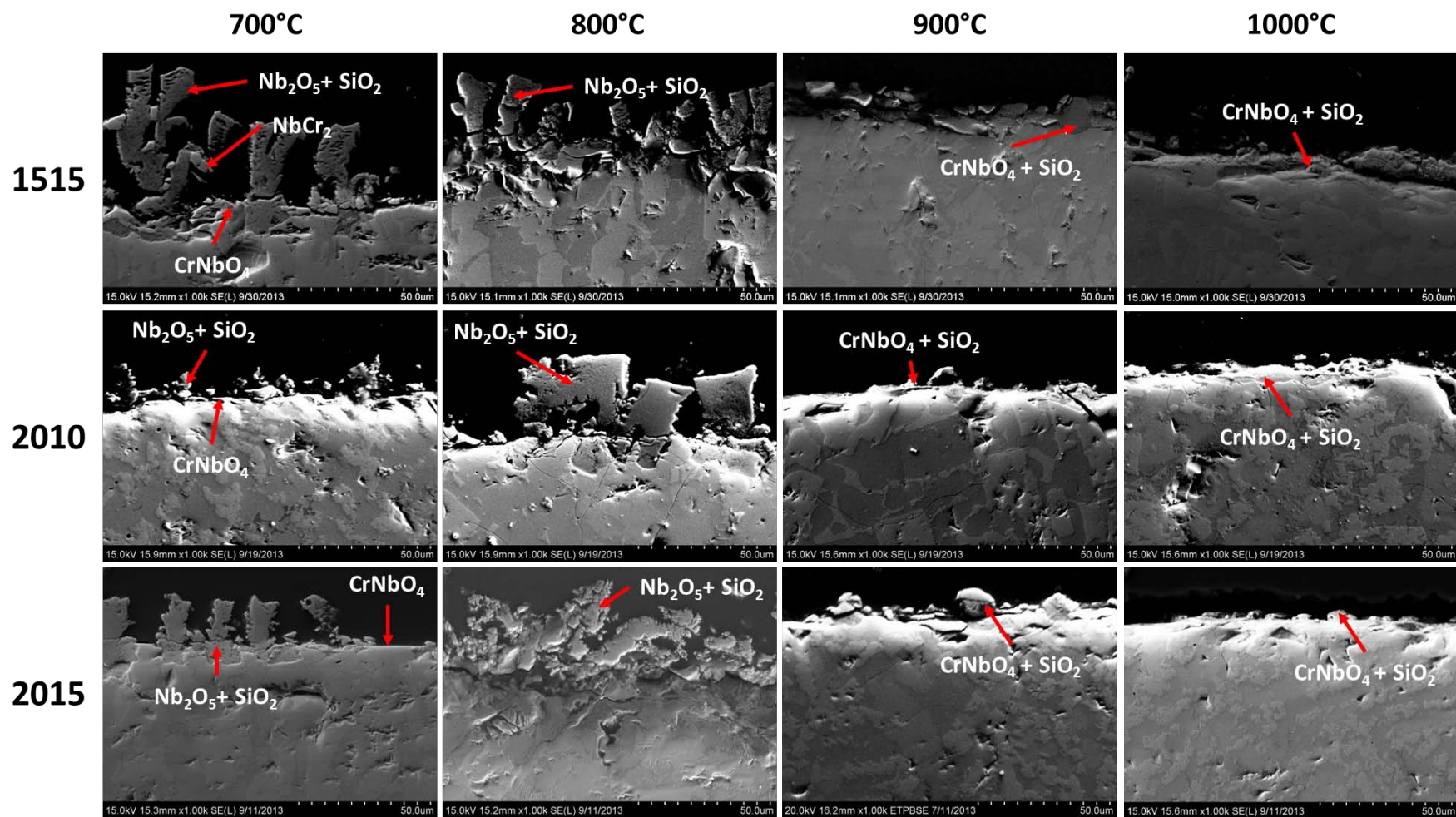


Figure 4.62: Oxide metal interfaces developed after short term oxidation at indicated temperature for the 1515, 2010, and 2015 alloys; micrographs collected in secondary imaging mode.

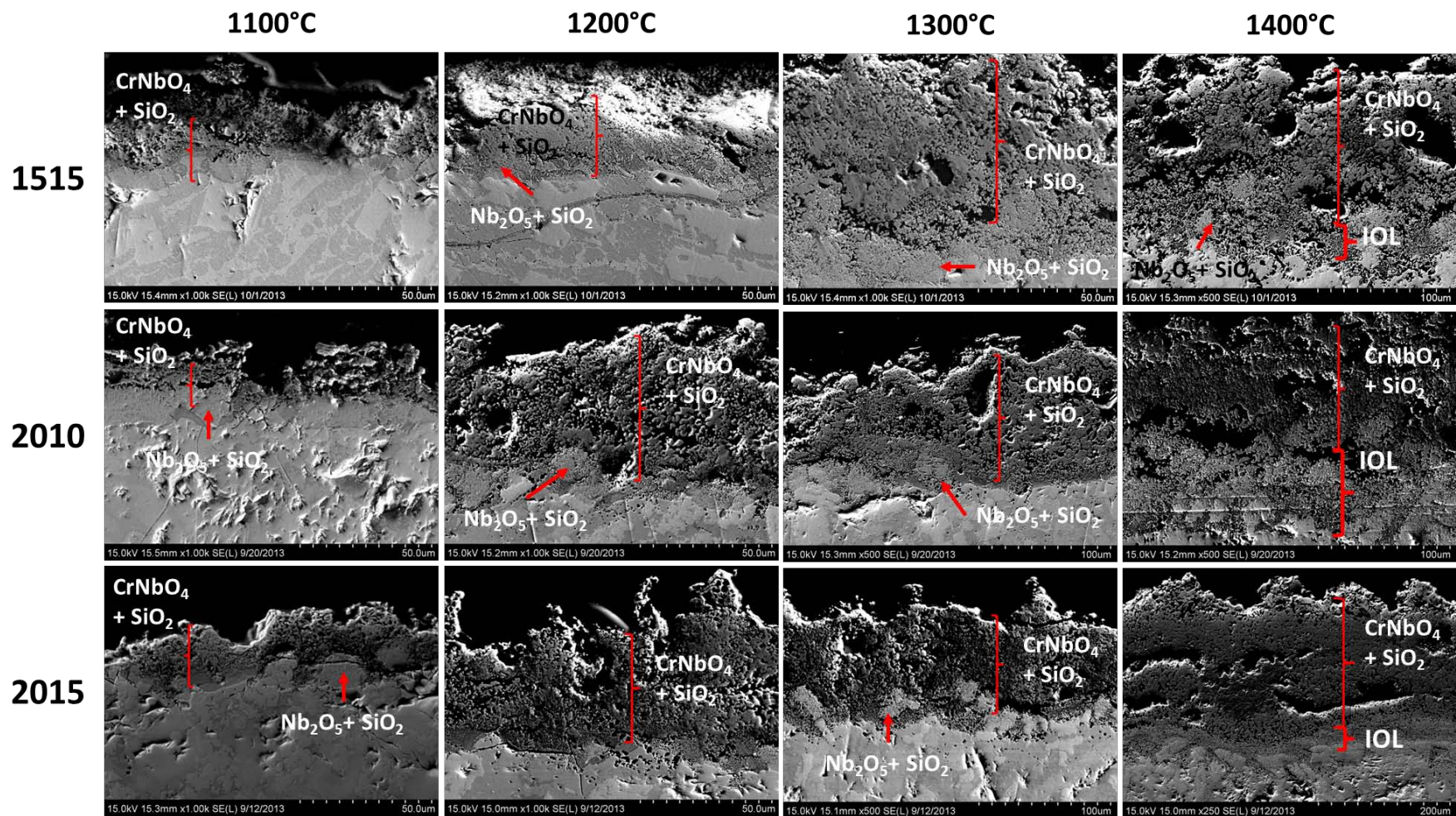


Figure 4.63: Oxide metal interfaces developed after short term oxidation at indicated temperature for the 1515, 2010, and 2015 alloys; micrographs collected in secondary imaging mode.

4.3.3 Cyclic Oxidation

Samples were exposed to cyclic oxidation for one week, after oxidation the developed oxides were analyzed by XRD as is shown in Figure 4.64. Variations in the pattern were contained to the maximum temperature at which the Nb_2O_5 was detected at the surface, for the 1515 alloy this was 900°C, for the 2010 and 2015 alloys detection stopped after 1000°C. The 2010 and 2015 alloy show the SiO_2 peak while for the 1515 alloy the amorphous bulge was present.

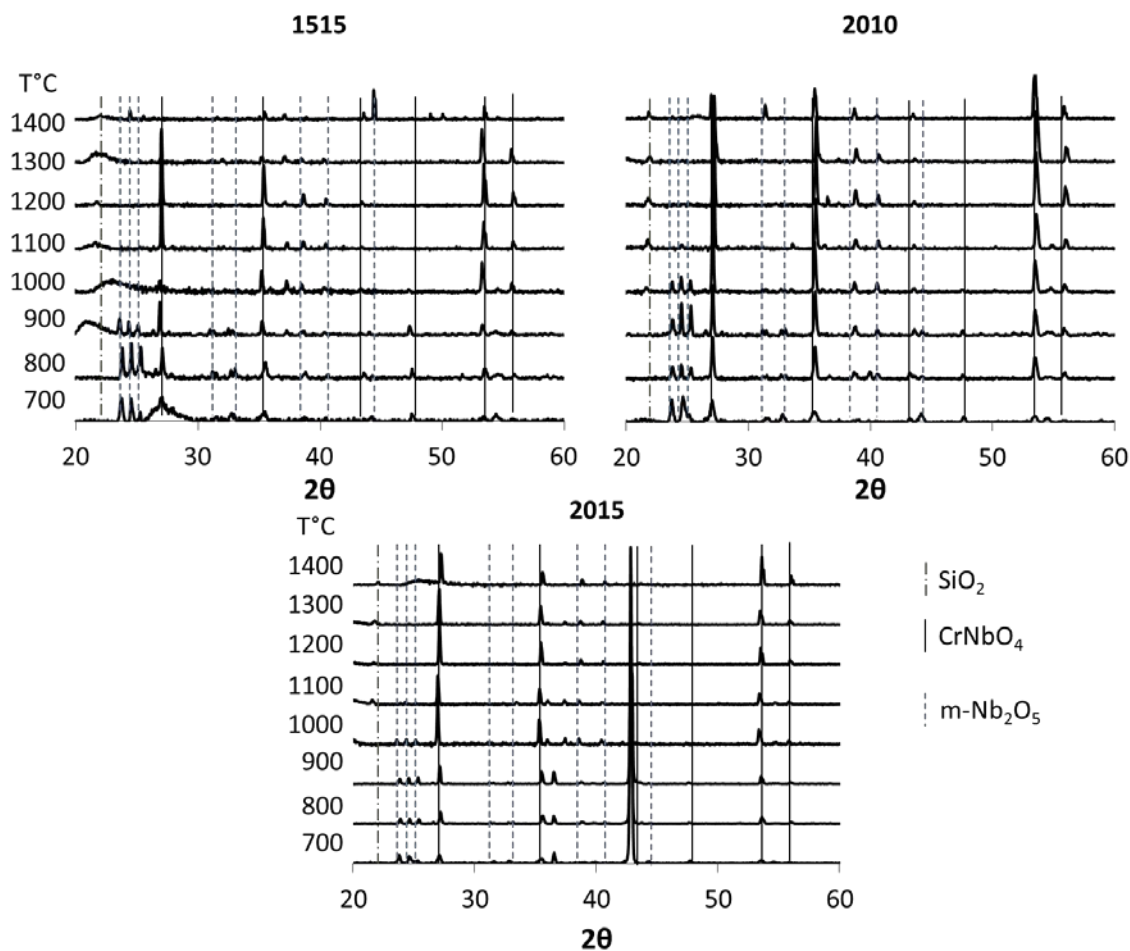


Figure 4.64: XRD patterns obtained for the alloys after cyclic oxidation.

The cyclic oxidation results after seven cycles of exposure at 700-900°C are presented in Figure 4.65a-c. The 2010 alloy maintained a similar weight gain for all three temperatures while the 1515 alloy tended to lower weight gains as the temperature increased, likely due to the small amount of pest product that forms at 700°C. The 2015 sample had a slight increase in oxidation at 800°C but

maintained relatively low weight gain. The microstructure remained similar to the as cast structure for all samples after exposure, recall that in the 10B and 15B alloys, at least a 72 hour continuous exposure at 900°C was required to see any changes in microstructure. When compared to the data available for the 10B and 15B samples in Portillo and Rangel's work, the 15Mo alloys perform comparably in the low temperature regime.

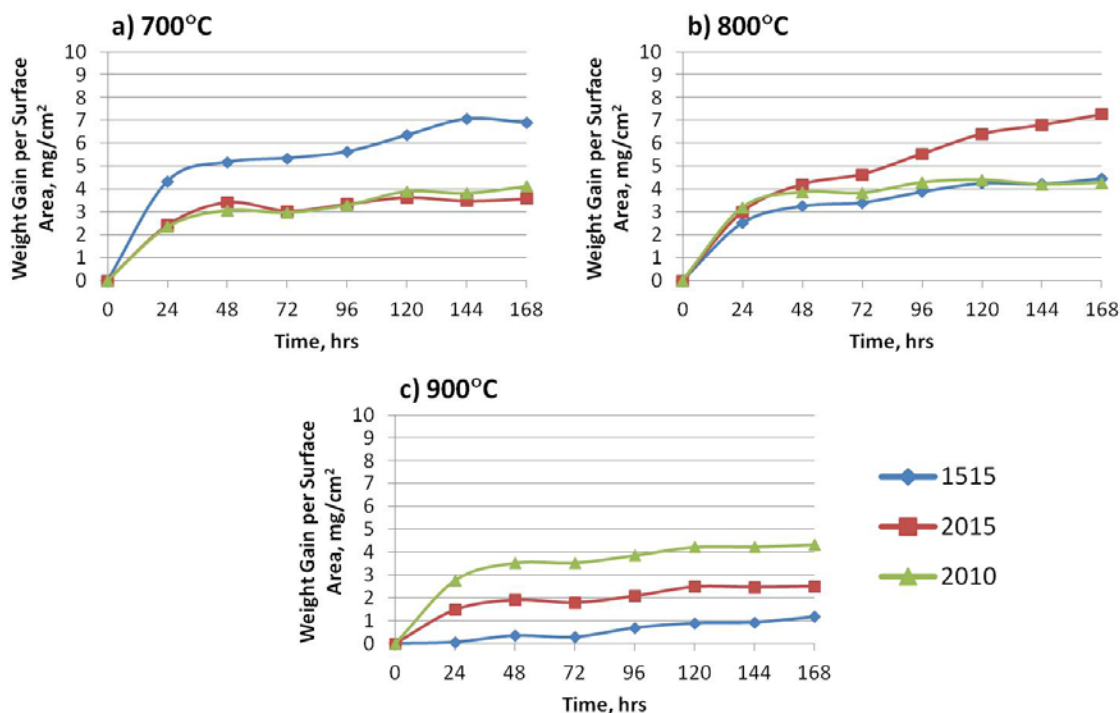


Figure 4.65: Gravimetric curves developed for the 15Mo alloys after cyclic oxidation at a) 700°C, b) 800°C, and c) 900°C.

Oxides developed at 700°C temperature are very fragile, after mounting and during sectioning/polishing, separation of the mount from the sample caused the bulk of the oxide to remain suspended in the epoxy mount for the 2010 and 2015 samples. The samples develop discontinuous oxide layers comprised primarily of Nb₂O₅ and SiO₂ columnar like protrusions growing from the silicides with small granules of CrNbO₄, characteristic micrographs of the oxide layers are shown in Figure 4.66. This development is very similar to the oxides formed by previous alloys in this system. As oxidation temperature increased at the interface of the bulk Nb₂O₅ and SiO₂ protrusions and the metal a thin

CrNbO_4 layer develops. The 1515 alloy showed the most prominent layer of CrNbO_4 at the interface contributing to the low weight gain response at 900°C .

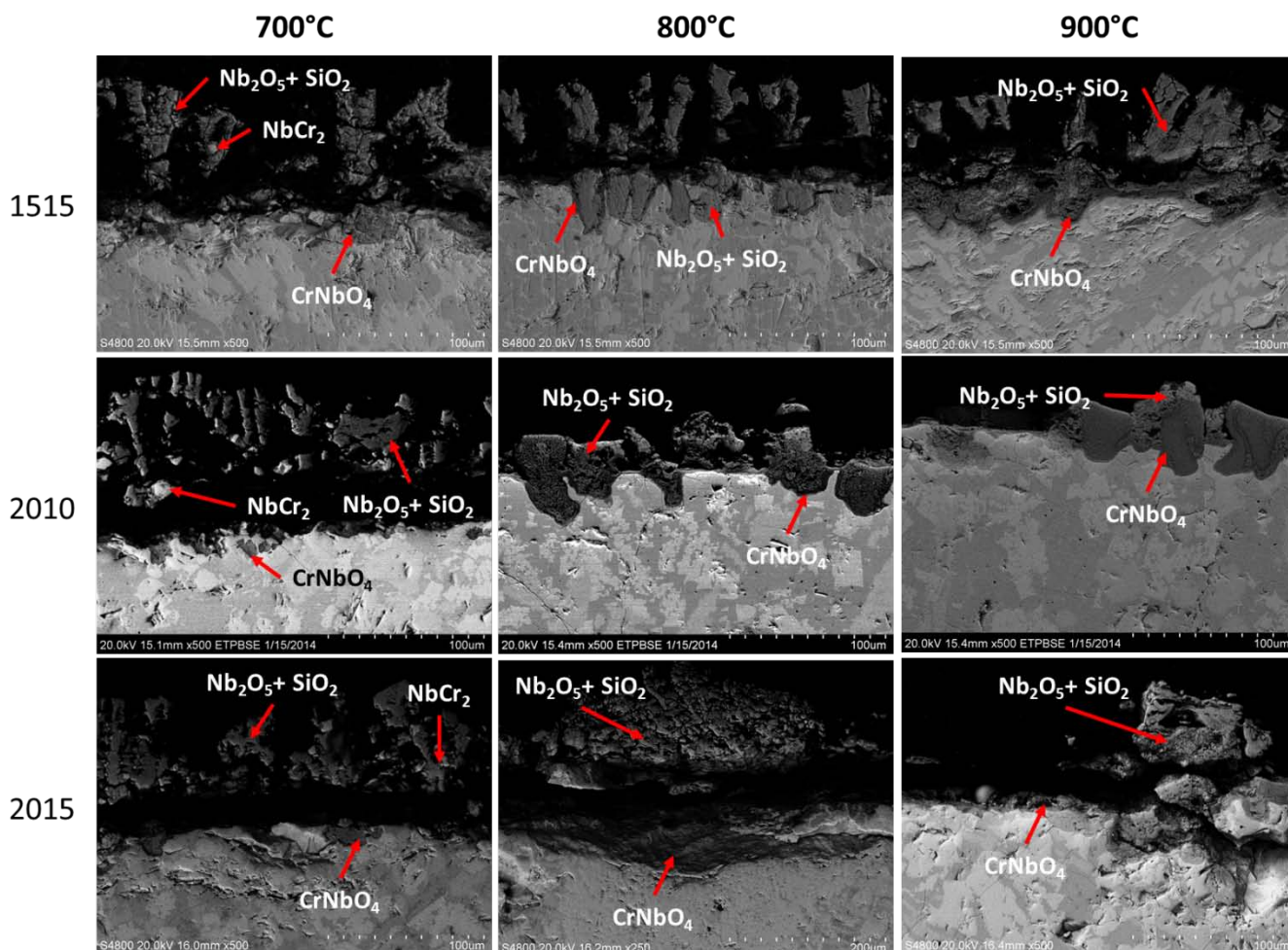


Figure 4.66: Oxide metal interface developed for the 1515, 2010, and 2015 samples after cyclic oxidation at 700°C , 800°C and 900°C .

The gravimetric curves for samples exposed at 1000°C are presented in Figure 4.67. Oxidation carried out at 1000°C showed the lowest weight gains for the 2010 and 2015 alloys, while the 1515 alloy had a slight increase from the oxidation at 900°C . The oxides are continuous and primarily composed of CrNbO_4 and SiO_2 with Nb_2O_5 retained near the interface, characteristic micrograph is shown in Figure 4.68, the developed scales are also the thinnest among all temperatures. The beginning stages of the intermediate oxide layer (IOL) formation are found at the interface, though it is not a continuous layer at

this temperature. Similar to the 10B alloy, the 1515 alloy develops a Mo-rich precipitate within the Laves phase, visible within the bulk metal below the interface. The 2010 alloy does not show any microstructural changes at this temperature. The dark grey phase in the 2015 alloy is identified as having a close to that of Cr_3Si in isolated regions though this may be a Si enriched Laves phase. Micro-cracking is observed in the 2010 and 2015 samples, no oxidation was found within the cracks suggesting they formed during cooling. At 1000°C the 15Mo alloys achieve comparable weight gain results as the 10B and 15B [16, 15].

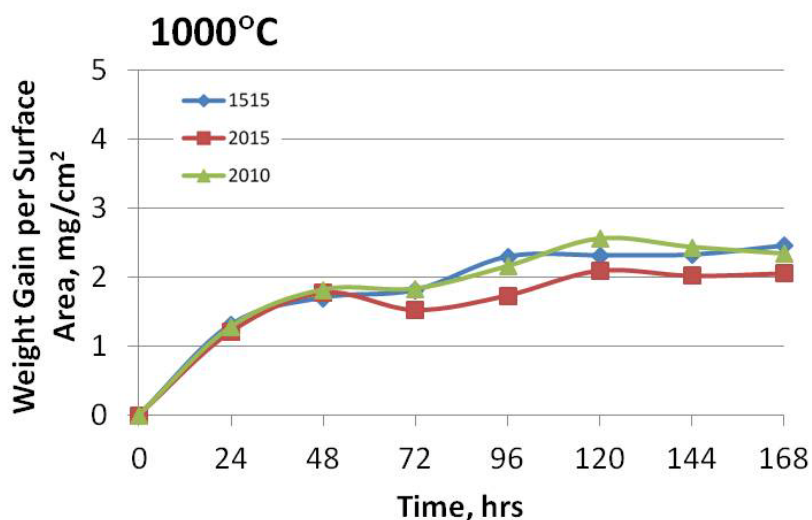


Figure 4.67: Gravimetric curves developed for the 15Mo alloys after cyclic oxidation at 1000°C .

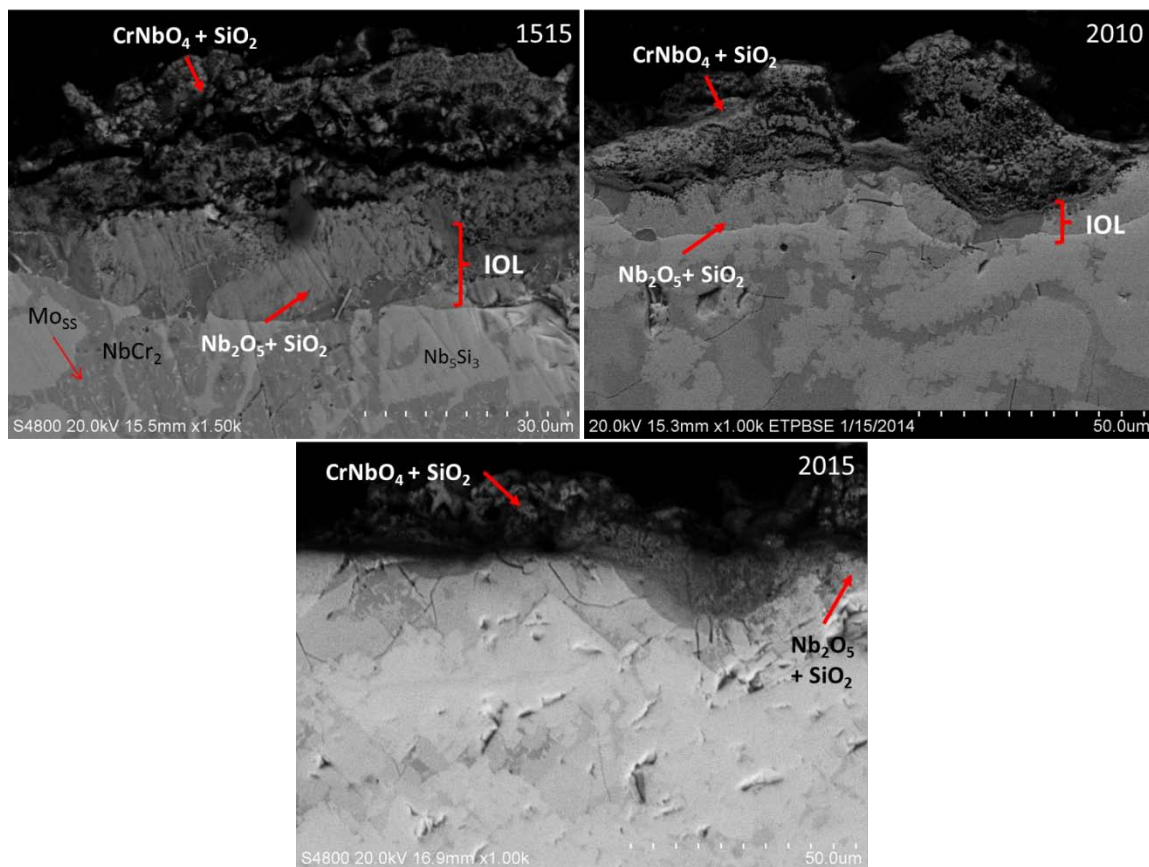


Figure 4.68: Oxide metal interface developed for the 15Mo alloys after cyclic oxidation at 1000°C.

Results for samples exposed from 1100-1300°C are presented in Figure 4.69. The 1515 alloy shows a comparatively large increase in weight gain as compared to the 2010 and 2015 alloys as the temperature is increased. The 2015 alloy had an increase in oxidation from 1100°C to 1200°C but no increase from 1200 to 1300°C. Comparing the 2010 alloy with the 10B alloy [16, 15], at 1300°C the final weight gains were within a few mg/cm^2 . For the 2015 alloy versus the 15B alloy [16], oxidation resistance improved at 1300°C. The microstructural morphology followed similar patterns as was found for the 10B and 15B samples. The 1515 alloy developed Mo_{SS} at 1100°C but returned to the two phase structure at 1200°C as shown in Figure 4.70. The 2010 alloy remained relatively unchanged from its as cast state up to 1300°C, shown in Figure 4.71. The 2015 alloy eutectic region which contains the Laves phase, begins to lose the well-defined eutectic by 1300°C, as shown in Figure 4.72. Samples developed thicker oxides comprised of CrNbO_4 and SiO_2 with porosity present within the scale, as seen in Figure

4.73, the oxides coarsened as temperature increased. Starting at 1300°C there is subscale internal oxidation of silicon within the phases to form SiO₂, most prominent in the 2010 alloy.

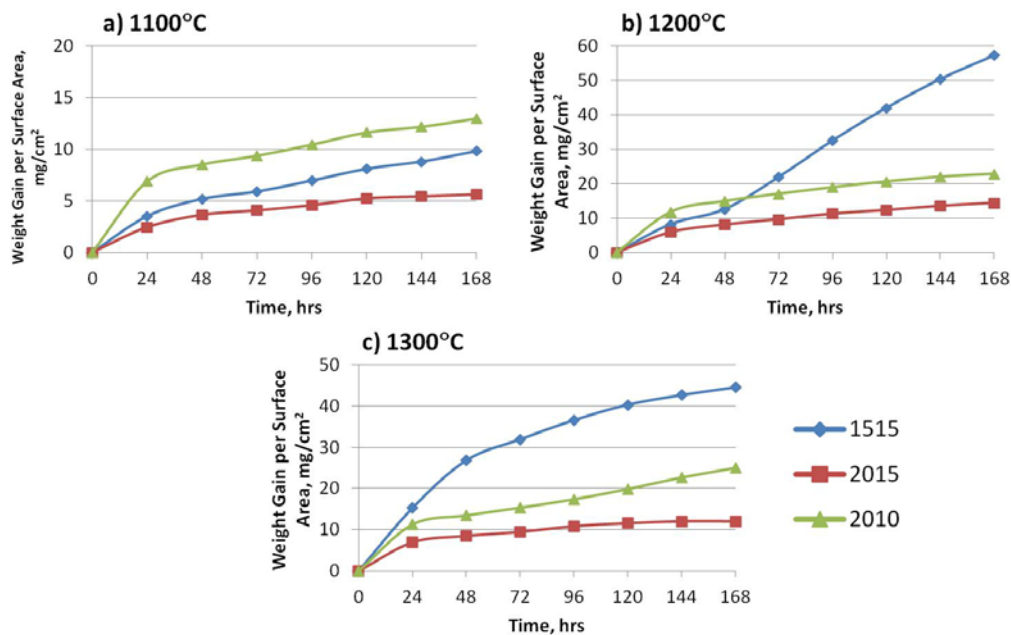


Figure 4.69: Gravimetric curves developed for the 15Mo alloys after cyclic oxidation at a) 1100°C, b) 1200°C, and c) 1300°C.

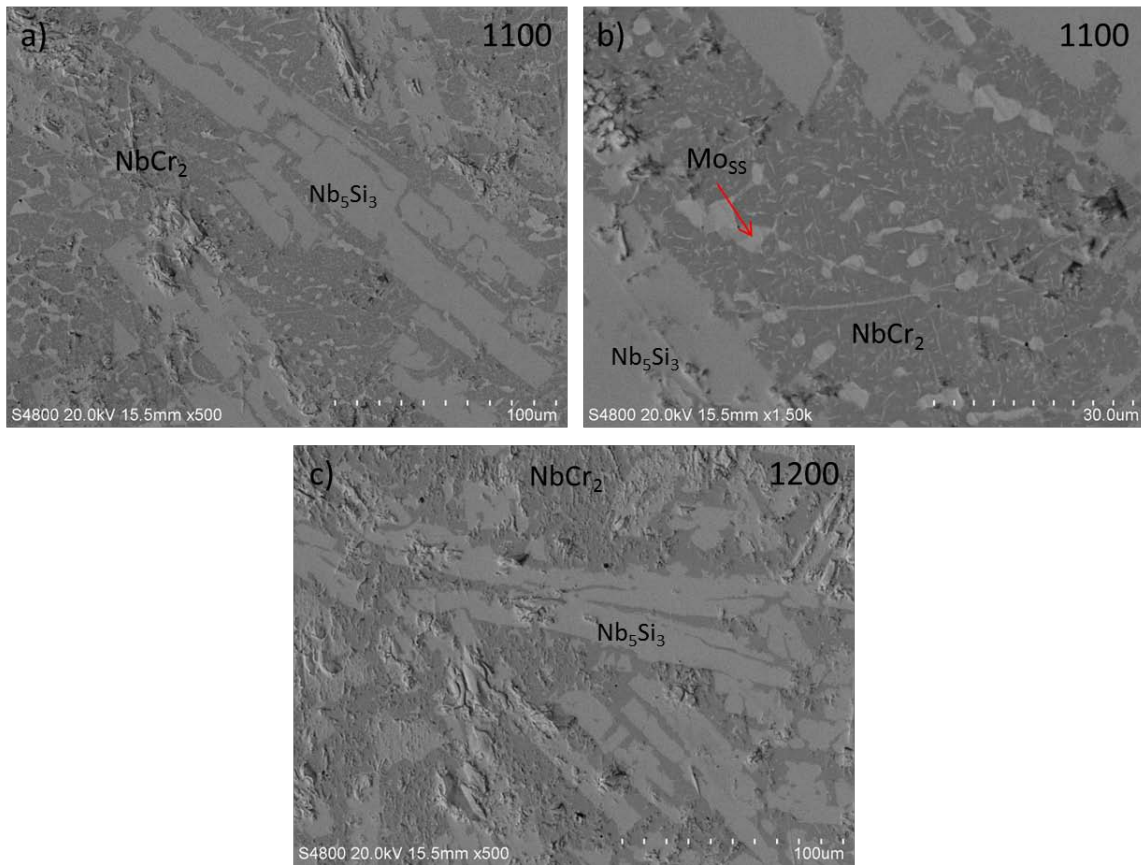


Figure 4.70: Bulk metal remaining for the 1515 alloy at 1100°C at a) low magnification, b) high magnification of the Laves phase showing precipitated Mo_{SS} and c) at 1200°C.

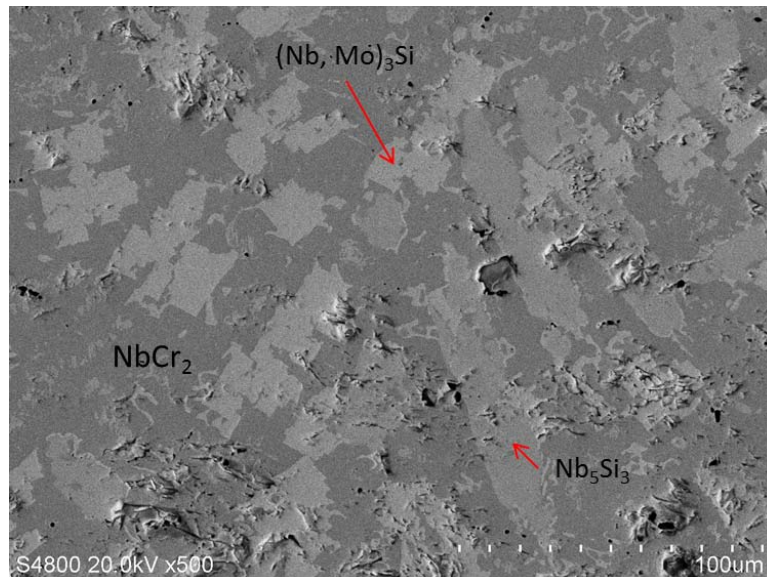


Figure 4.71: Bulk metal remaining for the 2010 alloy at 1300°C.

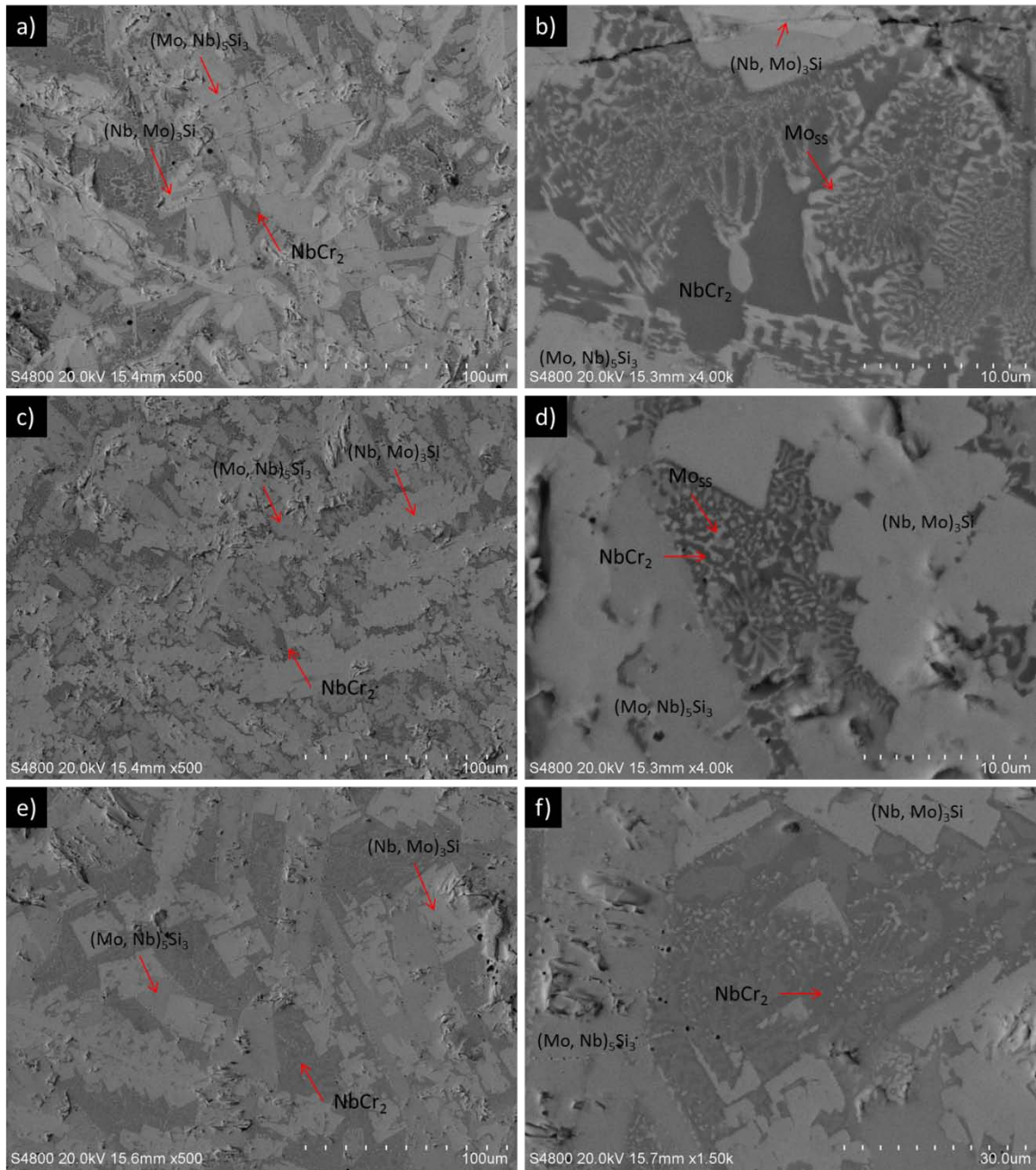


Figure 4.72: Bulk metal remaining for the 2015 alloy at a) 1100°C – low magnification, b) 1100°C – high magnification of Laves region, c) 1200°C – low magnification, d) 1200°C – high magnification of Laves region, e) 1300°C – low magnification, f) 1300°C – high magnification of Laves region.

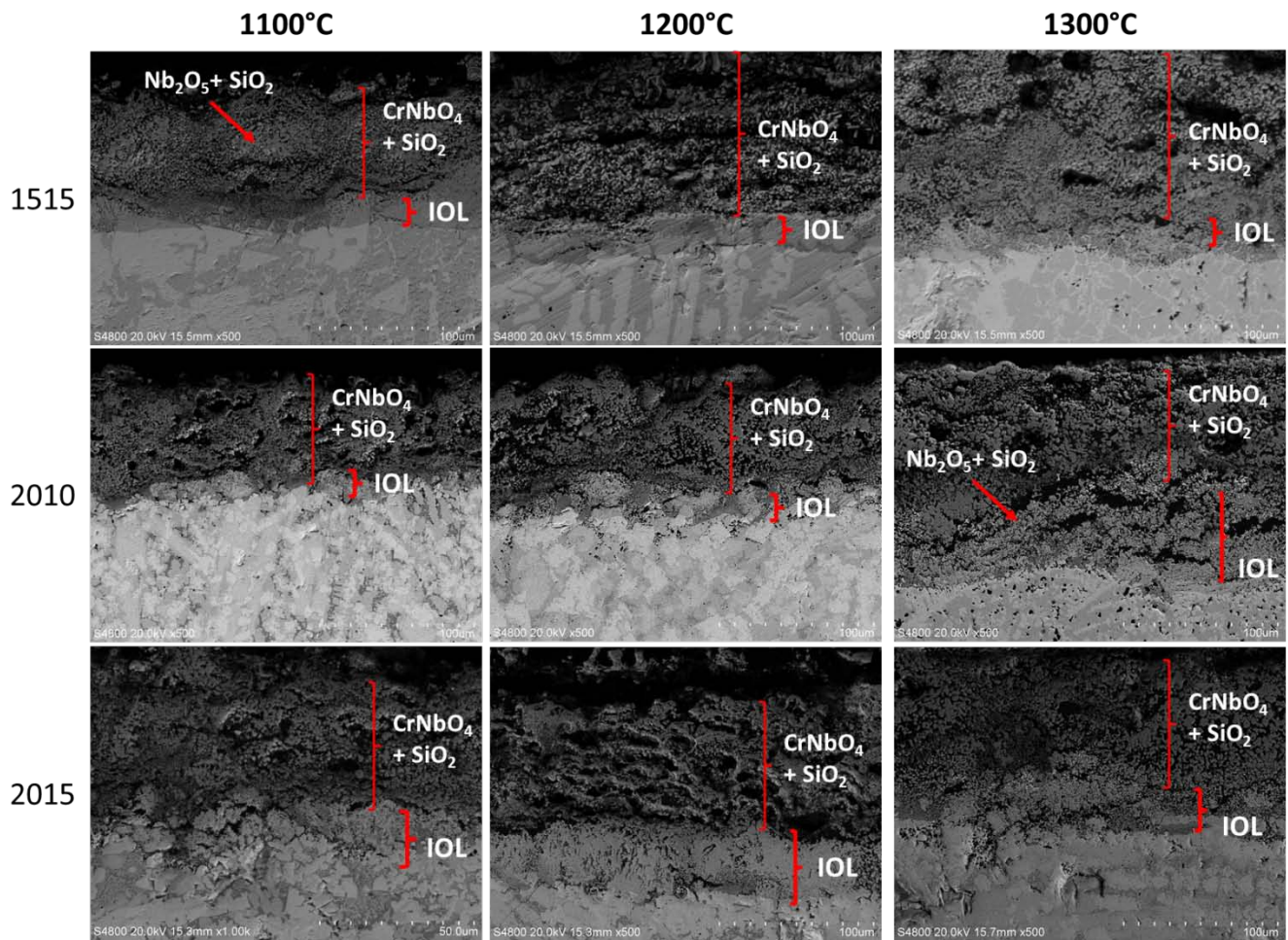


Figure 4.73: Oxide metal interface developed for the 1515, 2010, and 2015 samples exposed at 1100°C, 1200°C, and 1300°C.

The three alloys showed significant increases in weight gain at 1400°C as shown in the gravimetric curves in Figure 4.74. The 1515 and 2010 samples obtained similar final weight gains while the 2015 alloy maintained a lower overall gain. Approximate metal remaining for the alloys at this temperature was 25% for the 1515, 10% for the 2010, and 70% for the 2015 alloy. The 2010 and 2015 alloy showed a significant decrease in oxidation resistance to the 10B and 15B alloys at this temperature suggesting that the effect of the additional 3-1 silicide is negative in the highest temperature regime.

The microstructure of all samples showed internal oxidation of silicon, as shown in Figure 4.75, this is most prominent in the 1515 sample an 2010 sample had the least amount of internal oxidation. Oxide scales grown at this temperature, shown in Figure 4.76, were much thicker than those grown at

1300°C, though they contained similar features such as the bulk structure of CrNbO_4 and SiO_2 , the presence of the IOL is shown by the brackets, though it is not as easily delineated as in the 10B and 15B alloy. At the interface the scales are well adherent to the base metal, though cracking likely due to differences in coefficients of thermal expansion is seen in some areas. A complete SiO_2 layer previously observed in the Nb-25Cr-20Mo-15Si-15B alloy was not achieved within the 168 hour period of this study for any of the alloys.

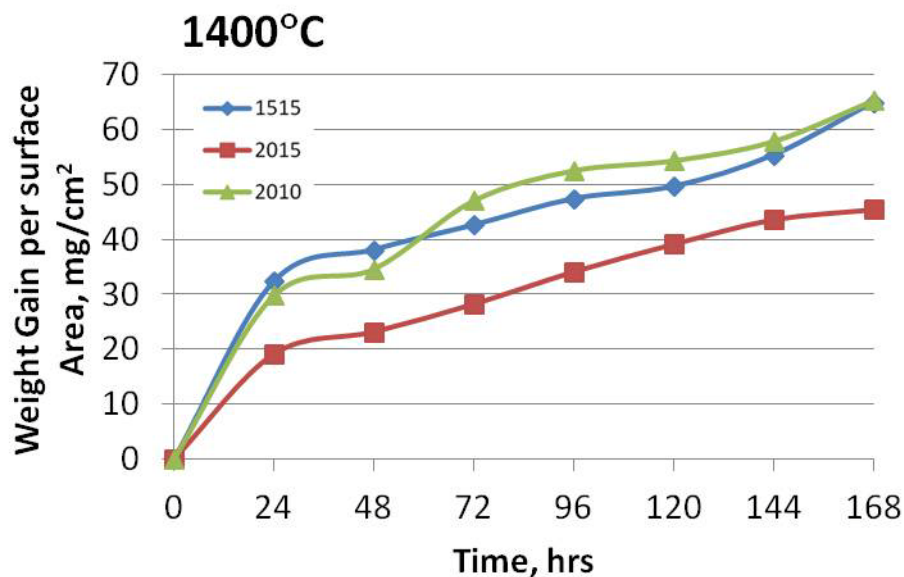


Figure 4.74: Gravimetric curves developed for the 15Mo alloys after cyclic oxidation at 1400°C.

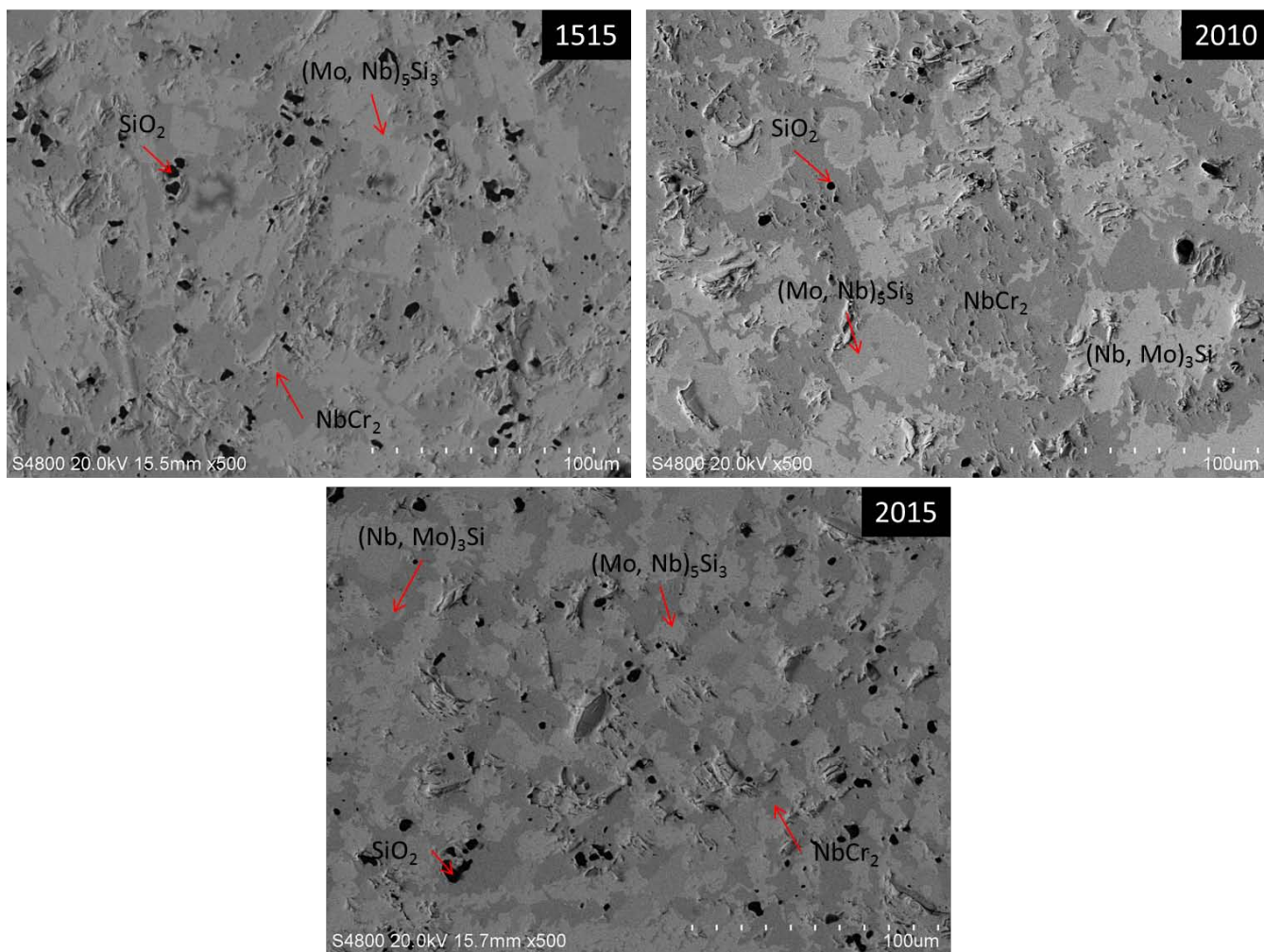


Figure 4.75: Bulk metal remaining for the 15Mo alloys after cyclic oxidation at 1400°C, internal oxidation of Si-containing phases to form SiO_2 occurs in all samples.

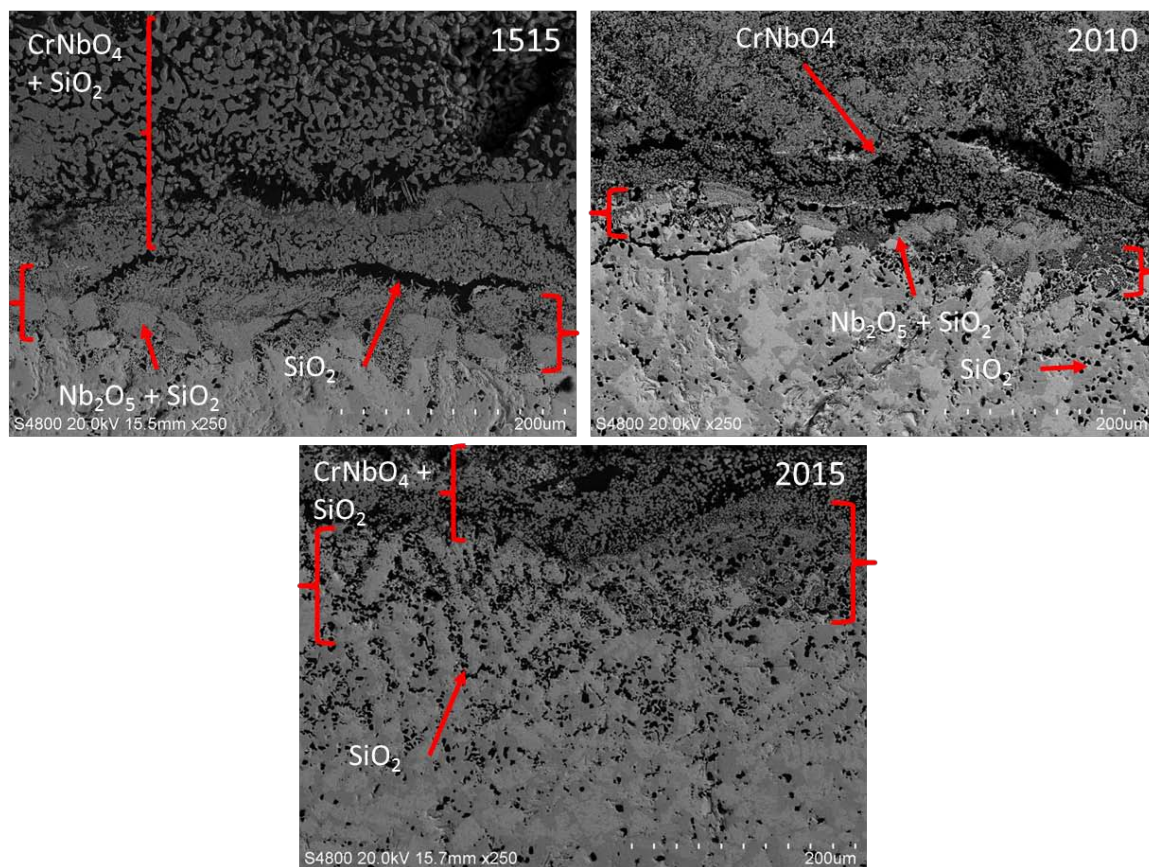


Figure 4.76: Oxide metal interface developed for the 15Mo alloys after cyclic oxidation at 1400°C.

4.3.4 Static Oxidation

The 15Mo alloys were subjected to one week of continuous exposure at 700, 900, 1100, and 1300°C to check for any changes in the oxidation response versus those that were exposed cyclically and to compare their response with that of the 10B and 15B alloys. The gravimetric data obtained for the alloys is presented in Figure 4.77 along with data for the 10B and 15B alloys.

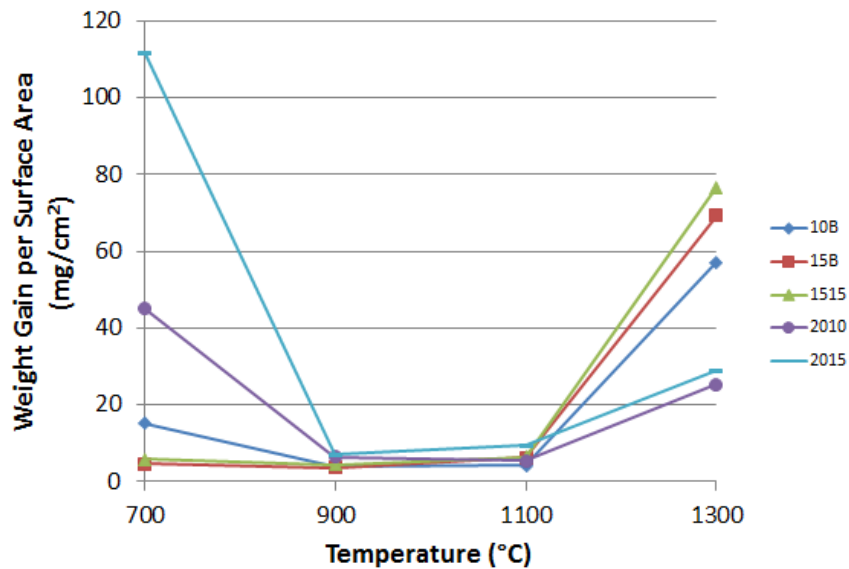


Figure 4.77: Weight gain data for the alloys obtained after a week of static exposure.

At 700°C the 15B and 1515 samples perform the best, showing the least amount of weight gain along with no pest product visible within the crucibles, approximately 99% of metal remains for both samples. The 10B samples performance is within the range for its previous exposures, having 50% metal remaining. The 2010 and 2015 samples both show increased weight gain and significant pest product within the crucible after exposure, with 20 and 60% metal remaining respectively. This is most likely due to the increased percentages of silicide within the microstructure which leads to greater formation of the Nb_2O_5 oxide in the lower range of temperatures. The mid-range temperature exposures for all samples are comparable, showing little variation in weight gain for any sample, metal remaining for all samples is approximately 99%. At 1300°C the 2010 and 2015 alloys have the lowest weight gain.

For the samples exposed at 700°C there is little to no change in the microstructures of the samples from their as-cast state, the 1515 sample having the two phase structure like the 10B and 15B samples is expected to have only the dissolution of the inter-dendritic 5-3 silicide to a eutectic like structure, as has started in the 10B, or no change at all, like the 15B. The scales developed are reminiscent of those found during previous exposure periods, viewed in Figure 4.72. At 900°C and

1100°C the scales were again dominated by CrNbO_4 and SiO_2 with the development of the IOL at the higher temperature, the scales are viewed in Figures 4.73 and 4.74 respectively.

While having similar features as the 10B and 15B alloy, the scale developed in the modified alloys was thinner and held less porosity.

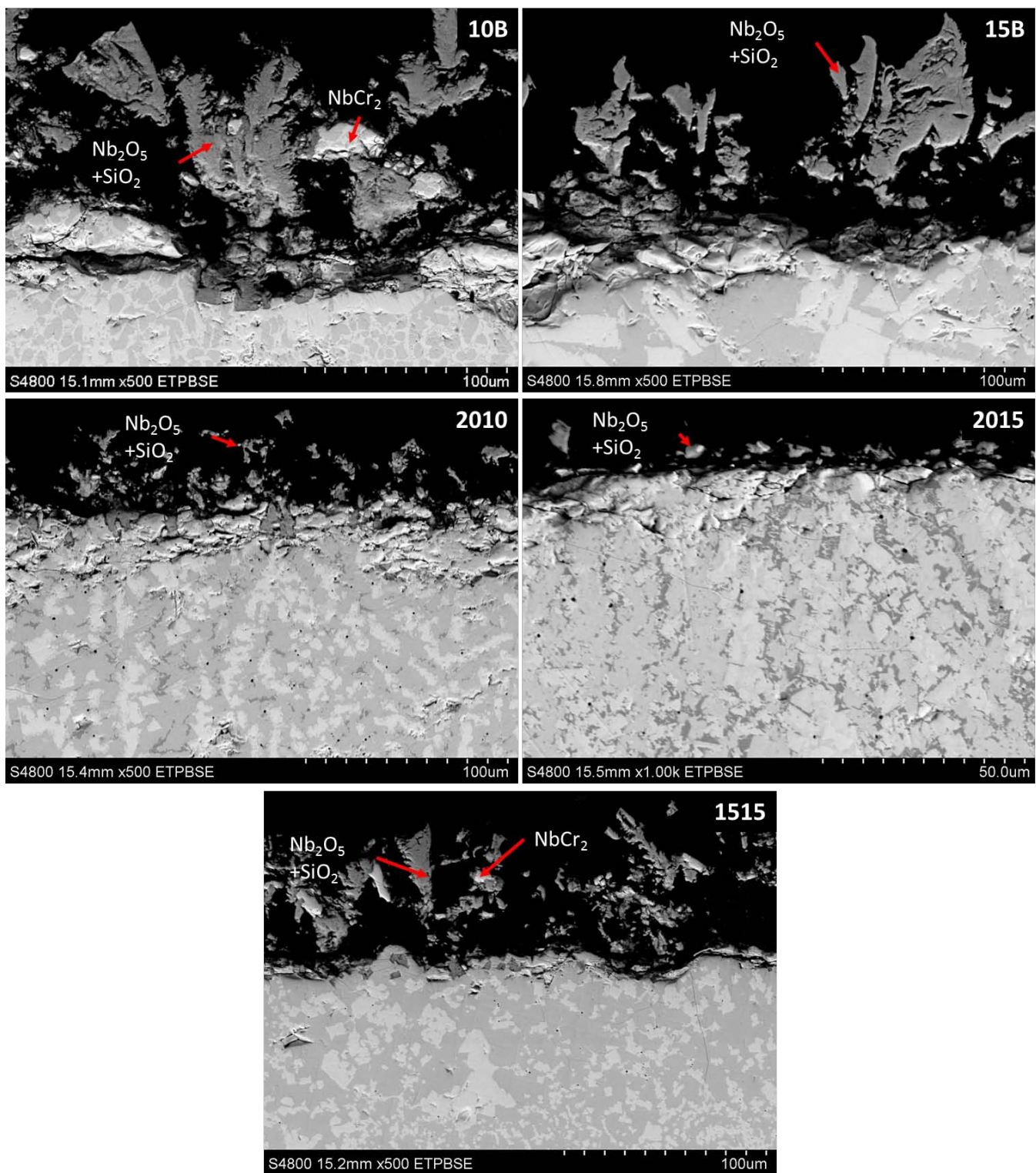


Figure 4.72: Oxide and microstructure of metal remaining for the alloys after 7 days static oxidation at 700°C.

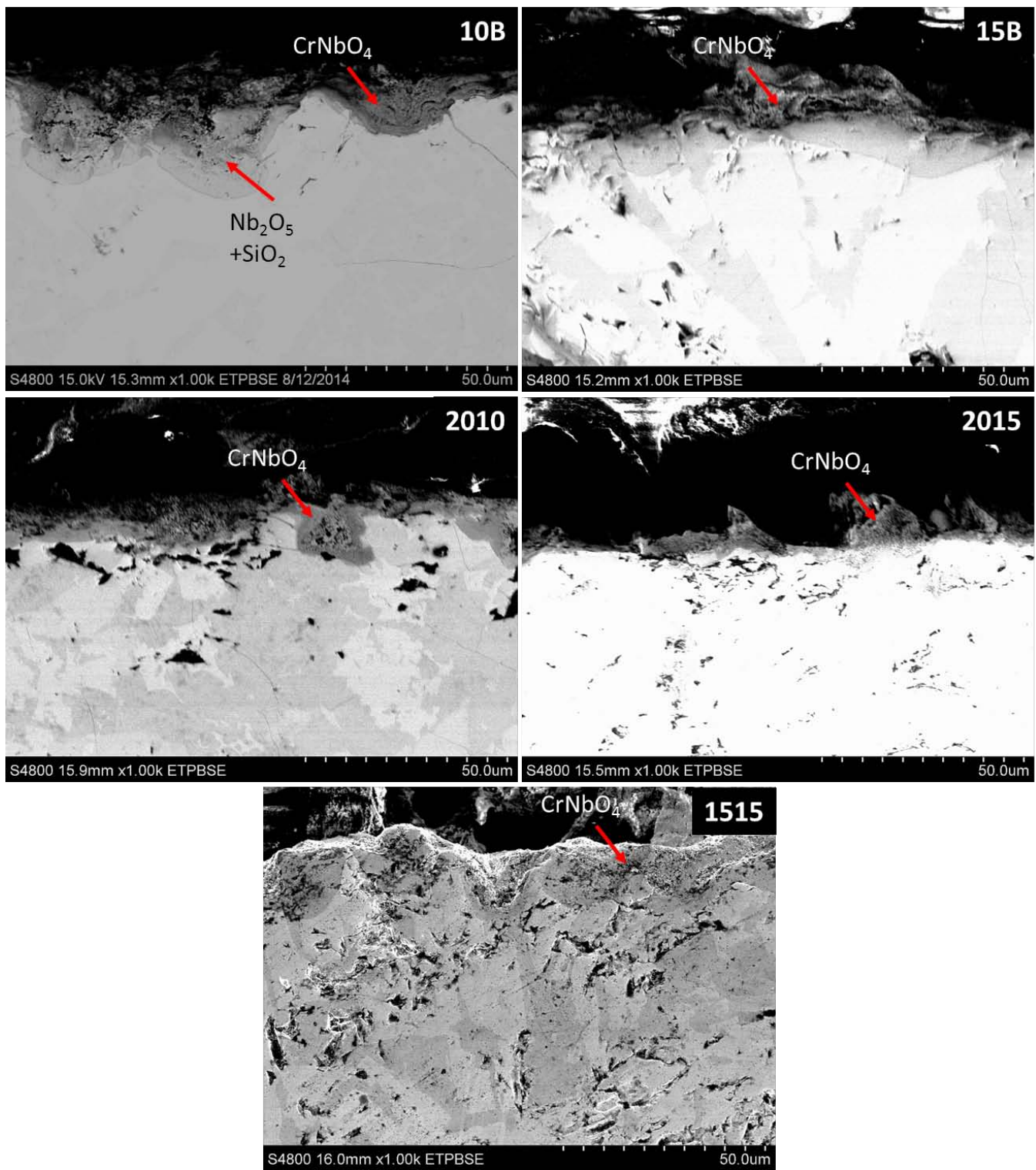


Figure 4.73: Oxide metal interface for the alloys after 7 days static oxidation at 900°C.

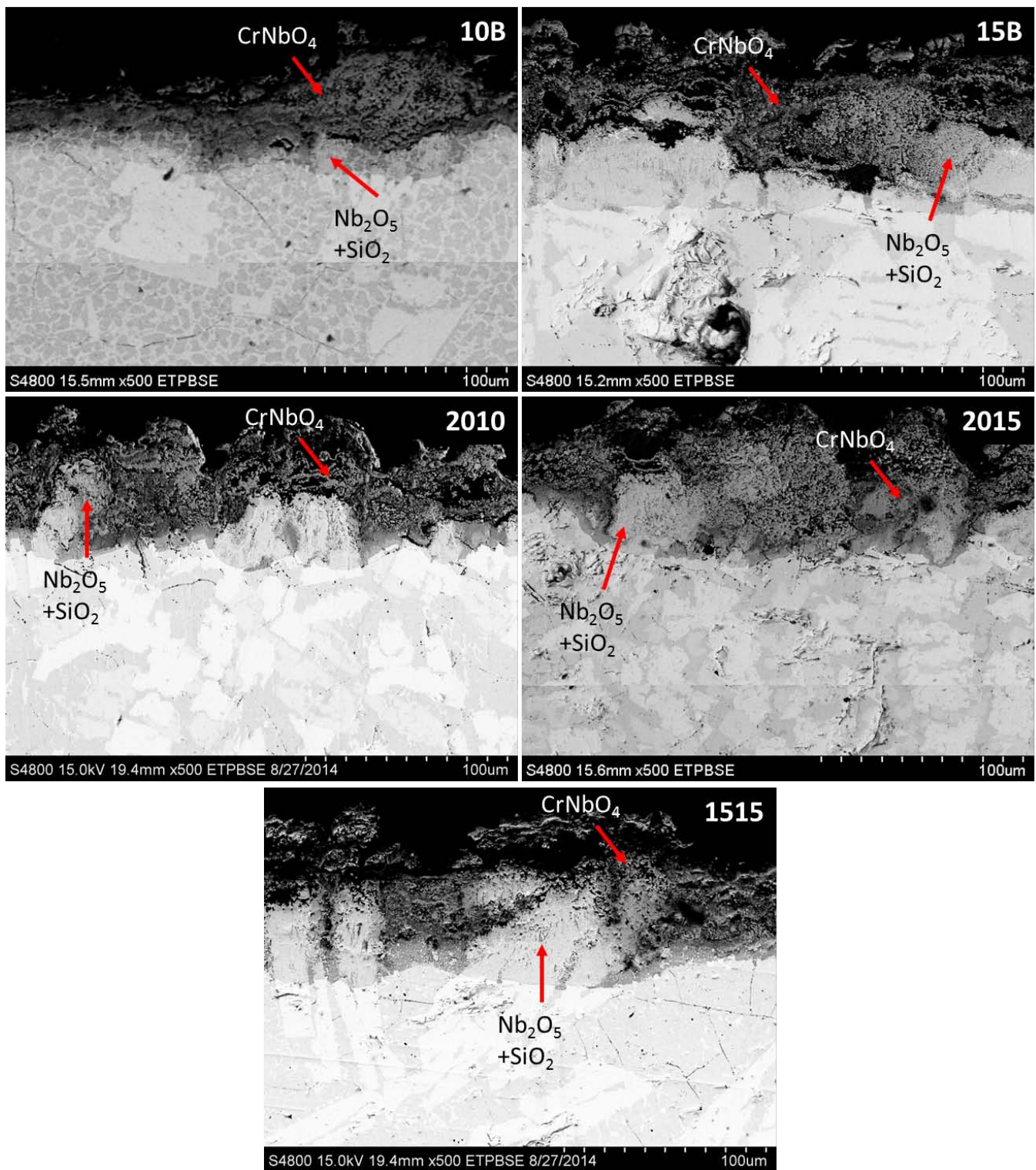


Figure 4.74: Oxide metal interface for the alloys after 7 days static oxidation at 1100°C.

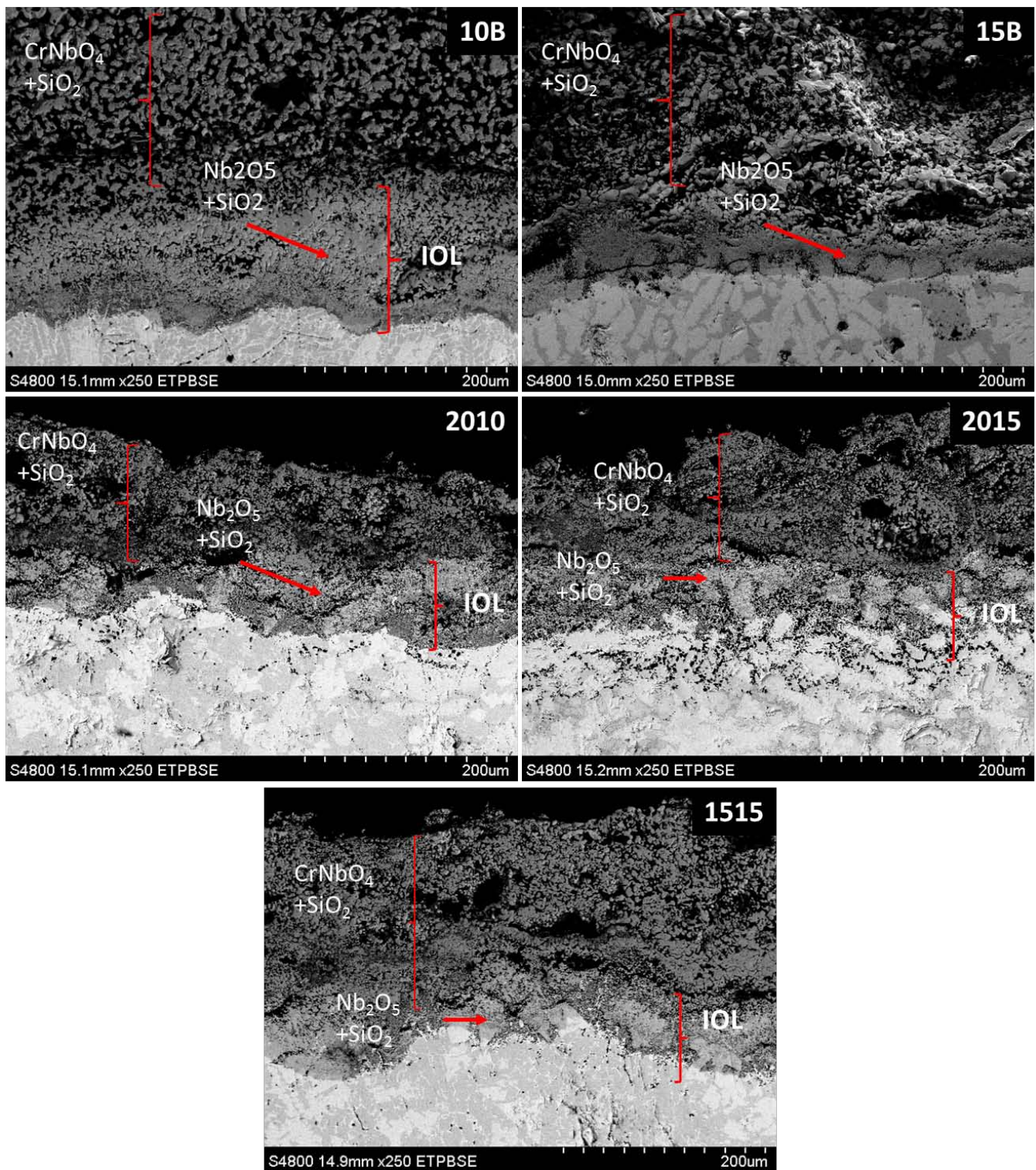


Figure 4.75: Oxide metal interface for the alloys after 7 days static oxidation at 1300°C.

Chapter 5: Discussion, Recommendations and Future Work

The oxidation behavior and microstructure of five Nb-Cr-Mo-Si-B alloys have been evaluated for potential use as high-temperature materials.

5.1 DISCUSSION

Microstructural features of all alloys studied include the NbCr₂ Laves phase with the C14 structure and (Nb, Mo)₅Si₃ silicide. High silicon containing alloys include the addition of (Nb, Mo)₃Si silicide. Microstructural transformations occur primarily at high temperature. The Nb-25Cr-20Mo-15Si-10B and Nb-25Cr-15Mo-15Si-15B alloy maintains a two-phase structure of NbCr₂ and (Nb, Mo)₅Si₃ until 1100°C at which Mo-rich precipitates are formed within the Laves phase region. The formation of the precipitate in the Laves region at 1100°C and below may be related to the interaction of Cr and Mo which in their binary mixture contain a miscibility gap up to approximately 1100°C. This would explain why the precipitate is not found in the 1300°C samples. When the samples are cast they are cooled in non-equilibrium conditions allowing for a higher content of Mo within the Laves phase region to remain in solution.

The alloys tended to form a mix of monoclinic Nb₂O₅ and CrNbO₄ at lower temperatures, with the scale becoming dominated by CrNbO₄ as the temperature increased. This is confirmed by the investigations of the oxide-metal interface described in the previous section. At 700°C it was expected that some molybdenum oxides would form, however, through the XRD results it was not possible to differentiate a MoO₃ or Mo₁₃O₃₃ specific oxide, at higher temperatures the molybdenum oxides would volatilize. While crystalline SiO₂ is only ever detected by XRD at the higher temperatures its presence is likely as an amorphous structure as it is easily detected by EDAX analysis. As the crystallinity of the SiO₂ occurs higher oxidation responses are found in the materials, oxygen is allowed to penetrate

through the crystalline structure to further oxidize the base material, reducing the protective nature of the mixed CrNbO_4 and SiO_2 layer.

As is apparent from the various graphs detailing the oxidation behavior over long-term periods the Nb-25Cr-20Mo-15Si-15B alloy shows superior oxidation resistance to the Nb-25Cr-20Mo-15Si-10B alloys. The higher boron content has suppressed the pest response in the lower temperature regime. The base-centered monoclinic form of Nb_2O_5 has been suppressed in the mid-range temperatures this may be due to a combination for a small Nb/Cr ratio (1 to 1.2) and the high boron content. The concentration of B or B_2O_3 within the scale is still difficult to quantify however its presence is assumed. The volatilization of B_2O_3 among other oxides is expected to attribute to any weight loss seen in the higher temperature samples, though this is generally offset by gains due to the formation of non-volatile oxides.

The detection of Mo within the scale despite temperatures exceeding the volatilization temperature may be due to several factors. It is possible that the Mo detected within the scale is due to a solid solution of MoO_3 - CrNbO_4 , similar to that found in a study [54] of Cr_2O_3 - α - Sb_2O_4 - MoO_3 where the Cr^{3+} and Sb^{5+} ions were substituted with Mo^{6+} within the scale producing vacancies. This behavior could also explain the mobility of oxygen through the scale despite the presence of CrNbO_4 and SiO_2 . The presence of a Mo oxide below the SiO_2 layer may be due to the sub-scale location where the pressure associated with the scale prevents the volatilization.

The 15B samples showed only minor weight gain variations from the cyclic to the static test at 700 and 900°C, suggesting that there was little influence of intermediate heat and cooling cycles on the oxidation products from a weight gain perspective. An intermediate oxidation layer which has been described as a protective layer [55, 15] has been observed for 15B alloys at temperatures above 900°C and in the 10B alloys at 1300°C. The 15B alloy static samples exhibited the trend of low weight gain at low temperatures followed by increases at 1100 and 1300°C. For the two higher temperature exposures, only a slight gain in oxidation over the cyclic samples was observed in the static samples. The oxidation

behavior of the alloys follows the schematic developed by Portillo. The 5-3 silicide first oxidizes to Nb_2O_5 and the CrNbO_4 layer is developed as chromium diffuses outward. This process is likely dependent on the width of the chromium/silicon depletion region. The formation of the Mo-rich solid solution may be due to the presence of the miscibility gap in the Cr-Mo system above 850°C . The 15B alloy show only coarsening of the Laves and silicide phase, the Mo-rich solid solution only developed in long term static exposures. The increase in boron stabilizes the two phase microstructure across the temperature range.

Cracks occurring where the majority of the bulk scale changes from Nb_2O_5 to CrNbO_4 were present in both cyclic and static modes. The crack formation may be attributed to the differences in the coefficients of thermal expansion of the oxide and the metal. Some literature values of the linear coefficients of thermal expansion are given in Table 4.2, notice that both monoclinic Nb_2O_5 and CrNbO_4 exhibit strong anisotropy with the largest coefficients existing for the c lattice parameter.

Table 4.2: Literature values of the coefficient of thermal expansion for oxides and the phases of the study.

Compound	a (10^{-6}K^{-1})	b (10^{-6}K^{-1})	c (10^{-6}K^{-1})	Ref.
SiO_2	0.51	—	—	[56]
CrNbO_4	5	5	8	[57]
$m\text{-Nb}_2\text{O}_5$	5.3	0	5.9	[58]
Nb_5Si_3	8.638	—	12.380	[59]
NbCr_2	6.4	—	—	[60]

Oxide products for all alloys include the formation of CrNbO_4 , Nb_2O_5 and SiO_2 . Continuous SiO_2 layers were achieved in the Nb-25Cr-20Mo-15Si-10B alloy at the oxide-metal interface after exposure at high temperature, however a large $\text{CrNbO}_4\text{-SiO}_2$ oxide layer is present. Microcracks are present at the oxide-metal interface. Oxide scales are fragile and discontinuous at low temperatures though bulk pest oxidation has been eliminated.

The oxide scale at low temperatures (700-800°C) develops initially through independent oxidation of the phases, Nb₅Si₃ and Nb₃Si oxidize to Nb₂O₅ and SiO₂ while the NbCr₂ Laves phase develops CrNbO₄ and SiO₂. With continued exposure, the outward diffusion of Cr allows for development of CrNbO₄ from the Nb₂O₅. In mid- and high-range temperatures (900°C-1400°C) the oxidation follows initially a cooperative

While the 15B samples do exhibit the best oxidation resistance of the two alloys studied here, they fall quite short of current Ni-base alloys. Estimated parabolic rate constants, k_p , for the samples range from 1.5 to $2 \times 10^{-5} \text{ mg}^2\text{cm}^{-4}\text{s}^{-1}$ which remains some orders of magnitude higher than those reported values for several Ni-based superalloys [61]. There is still a great deal of progress that needs to be made in order to reach the goal of replacing Ni-base superalloys with respect to oxidation resistance as currently for exposure times up to 300 hours at 1000°C isothermal testing [62] yields values below 0.001 g/cm^2 . Scales achieved in the Nb-25Cr-20Mo-15Si-15B sample are notably thinner than those of the Nb-25Cr-20Mo-15Si-10B, in comparison with Ni-based alloys, which have 10µm-thick oxides [62]; there is still a great deal of progress that needs to be made.

5.2 RECOMMENDATIONS AND FUTURE WORK

This work has been performed in order to evaluate the potential of Nb-Cr-Mo-Si-B alloys for high-temperature applications. Alloy design, as with any design process, is an iterative one in which each study provides new information for further development. The oxidation results presented here show a favorable direction for development; however this has been at the sacrifice of the mechanical properties of the material. Brittleness is a concern in the alloys due to the significant amount of intermetallic compound within the samples. Alloy composition development should look into either a lower Cr content or look into ternary phase containing compositions, which have also shown promising results [63]. Further work on the increase of oxidation resistance should be relegated to coating and near-surface interfaces, in order to allow the development of more mechanically sound materials for the bulk of the component. Laves phase or high Cr containing coatings may be favorable as the potential for protective Cr_2O_3 or CrNbO_4 is possible. Nb-silicide based coatings are not recommended due to the formation of the non-volatile Nb_2O_5 oxide that disallows formation of continuous SiO_2 layers.

As a first attempt at coating development a Mo coating on a substrate of the Nb-25Cr-20Mo-15Si-15B alloy has been shown to be highly dependent on the temperature of sputtering in order to adhere to the substrate.

References

- [1] J. H. Perepezko, "The Hotter the Engine, the Better," *Science*, vol. 326, pp. 1068-1069, 2009.
- [2] B. P. Bewlay, J. J. Lewandowski and M. R. Jackson, "Refractory Metal-Intermetallic In-Situ Composites for Aircraft Engines," *Journal of Materials*, pp. 44-45, 1997.
- [3] B. P. Bewlay, M. R. Jackson, J. C. Zhao and P. R. Subramanian, "A review of very high temperature Nb-silicide based composites," *Metal. Mater. Trans. A*, vol. 34A, pp. 2043-2051, 2003.
- [4] T. L. Yau and R. T. Webster, "Corrosion of Niobium and Niobium Alloys," in *ASM Metals Handbook*, 9th ed., vol. 13, 1987.
- [5] R. A. Perkins and G. H. Meier, "The Oxidation Behavior and Protection of Niobium," *JOM*, pp. 17-21, August 1990.
- [6] P. Kofstad, *High Temperature Corrosion*, 1988.
- [7] F. R. A. B. M. a. B. M. Holtzberg, "Chemistry of the Group VB Pentoxides. VI. The Polymorphism of Nb₂O₅," *J. Am. Chem. Soc.*, vol. 79, no. 9, pp. 2039-2043, 1957.
- [8] K. S. Chan, "Cyclic Oxidation Response of Multiphase Niobium-Based Alloys," *Metallurgical and Materials Transactions A*, vol. 35A, pp. 589-597, February 2004.
- [9] V. Behrani, A. J. Thom, M. J. Kramer and M. Akinc, "Microstructure and oxidation behavior of Nb-Mo-Si-B alloys," *Intermetallics*, vol. 14, pp. 24-32, 2006.
- [10] D. A. Helmick, G. H. Meier and F. S. Pettit, "The Development of Protective Borosilicate Layers on a Mo-3Si-1B (Weight Percent) Alloy," *MMTA*, vol. 36A, pp. 3371-3383, December 2005.
- [11] K. S. Chan, "Cyclic-Oxidation Resistance of Niobium-Base in situ Composites: Modeling and Experimentation," *Oxidation of Metals*, vol. 61, pp. 165-194, April 2004.
- [12] J. Ventura and S. K. Varma, "The Oxidation Resistance of Nb-20Mo-15Si-20Cr-5B up to 1,300°C," *JOM*, vol. 61, no. 7, pp. 72-75, July 2009.
- [13] S. K. Varma, C. Parga, K. Amato and J. Hernandez, "Microstructures and high temperature oxidation resistance of alloys from Nb-Cr-Si system," *J Mater Sci*, vol. 45, pp. 3931-3937, 2010.
- [14] B. I. Portillo and S. K. Varma, "Oxidation Behavior of Nb-20Mo-15Si-25Cr and Nb-20Mo-15Si-25Cr-5B Alloys," *Metall. Mater. Trans. A*, vol. 43A, January 2012.
- [15] B. I. Portillo, "Development and Characterization of the Oxidation Behavior of Various High Temperature Niobium Based Alloys," 2011.
- [16] V. R. Rangel, *The Effect of Al, Mo, And B on the Oxidation Behavior of Three Nb-Based Alloys*, 2012.
- [17] MatWeb, LLC., "MatWeb Material Property Data," 1996-2013. [Online]. Available: <http://www.matweb.com/>.
- [18] J. W. Martin, "Intermetallics: Laves Phase," in *Concise Encyclopedia of the Structure of Materials*, Elsevier, 2006, pp. 239-246.
- [19] A. V. Kazantzis, M. Aindow, I. P. Jones, G. K. Triantafyllidis and J. T. M. DeHossien, "The mechanical properties and the deformation microstructures of the C15 Laves phase Cr₂Nb at high temperatures," *Acta Materialia*, vol. 55, pp. 1873-1884, 2007.
- [20] C. T. Liu, J. H. Zhu, M. P. Brady, C. G. McKamey and L. M. Pike, "Physical metallurgy and mechanical properties of transition-metal Laves phase alloys," *Intermetallics*, vol. 8, pp. 1119-1129, 2000.

- [21] J. H. Westbrook, *Intermetallic Compounds*, New York: Wiley, 1967.
- [22] M. Yoshida and T. Takasugi, "The alloying effect on the high temperature deformation of Laves phase NbCr₂ intermetallic compound," *Materials Science & Engineering A*, Vols. A234-236, pp. 873-876, 1997.
- [23] J. C. Zhao, M. R. Jackson and L. A. Peluso, "Determination of the Nb-Cr-Si phase diagram using diffusion multiples," *Acta Materialia*, vol. 51, pp. 6395-6405, 2003.
- [24] O. N. Senkov, S. N. Senkova, D. M. Dimiduk, C. Woodward and D. B. Miracle, "Oxidation behavior of a refractory NbCrMo_{0.5}Ta_{0.5}TiZr alloy," *J Mater Sci*, vol. 47, pp. 6522-6534, 2010.
- [25] B. P. Bewlay, Y. Yang, R. L. Casey, M. R. Jackson and Y. A. Chang, "Effect of Cr Addition on the Phase Equilibria of the Nb-Si System," in *Mater. Res. Soc. Symp. Proc.*, 2007.
- [26] N. David, Y. Cartigny, T. Belmonte, J. M. Fiorani and M. Vilasi, "Thermodynamic description of the Cr-Nb-si isothermal section at 1473K," *Intermetallics*, vol. 14, pp. 464-473, 2006.
- [27] H. Zheng, S. Lu, Q. Su and F. Quan, "Study on scaling of mechanically alloyed and hot pressed NbCr₂ Laves phase at 1200C in air," *International Journal of Refractory Metals & Hard Metals*, vol. 26, pp. 1-4, 2008.
- [28] M. Venkatramen and J. P. Neumann, "The Cr-Mo (Chromium-Molybdenum) system," *Bulletin of Alloy Phase Diagrams*, vol. 8, no. 3, pp. 216-220, July 1987.
- [29] R. M. a. K. R. K. Chattopadhyay, "Nonisothermal and Isothermal Oxidation Behavior of Nb-Si-Mo Alloys," *Metall. Mater. Trans. A*, vol. 39A, pp. 577-592, 2008.
- [30] T. Geng, C. Li, X. Zhao, H. Xu, Z. Du and C. Guo, "Thermodynamic assessment of the Nb-Si-Mo system," *Calphad*, vol. 34, no. 3, pp. 363-376, 2010.
- [31] J. H. Schneibel, R. O. Ritchie, J. J. Kruzic and P. F. Tortorelli, "Optimization of Mo-Si-B Intermetallic Alloys," *Metll. Mater. Trans. A*, vol. 36A, pp. 525-531, March 2005.
- [32] H. Y. A. S. L. Z. J. W. Wei Li, "Effect of Mo addition on the phase stability of b-Nb₅Si₃ phase," *Intermetallics*, vol. 14, p. 392-395, 2006.
- [33] C. L. Fu and J. H. Schneibel, "Reducing the thermal expansion anisotropy in Mo₅Si₃ by Nb and V additions: theory and experiment," *Acta Materialia*, vol. 51, pp. 5083-5092, 2003.
- [34] K. Chattopadhyay, G. Balachandran, R. Mitra and K. K. Ray, "Effect of Mo on microstructure and mechanical behavior of as-cast NbSS-Nb₅Si₃ in situ composites," *Intermetallics*, vol. 14, pp. 1452-1460, 2006.
- [35] Y. Liu, M. J. Kramer, A. J. Thom and M. Akinc, "Oxidation Behavior of Multiphase Nb-Mo-Si-B Intermetallics," *Metall. Matl. Trans. A*, vol. 36A, pp. 601-607, March 2005.
- [36] C. A. Nunes, D. M. Pinto Jr., G. C. Coelho, P. A. Suzuki, A. A. A. Pinto da Silva and R. B. Tomasiello, "Isothermal Section of the Nb-Si-B System at 1700C in the Nb-NbSi₂-NbB₂ Region," *Journal of Phase Equilibria and Diffusion*, vol. 32, no. 2, pp. 92-96, 2011.
- [37] H. Nowotny, E. Dimakopoulou and H. Kudielka, "Untersuchungen in den Dreistoffsystemen: Molybdän-Silizium-Bor, Wolfram-Silizium-Bor und in dem System: VSi₂-TaSi₂," pp. 180-192.
- [38] Y. Murayama and S. Hanada, "High temperature strength, fracture toughness and oxidation resistance of Nb-Si-Al-Ti multiphase alloys," *Sci Tech Adv Mater*, vol. 2, pp. 145-156, 2002.
- [39] E. McCafferty, "Chapter 15: High-Temperature Gaseous Oxidation," in *Introduction to Corrosion Science*, Springer, 2010.
- [40] G. Wahl, "Coating composition and the formation of protective oxide layers at high temperatures," *Thin Solid Films*, vol. 107, no. 4, pp. 417-426, 1983.

- [41] G. Wang, B. Gleeson and D. L. Douglass, "A Diffusional Analysis of the Oxidation of Binary Multiphase Alloys," *Oxidation of Metals*, vol. 35, no. 5/6, pp. 333-348, 1991.
- [42] G. Wang, B. Gleeson and D. L. Douglass, "An Extension of Wagner's Analysis of Competing Scale Formation," vol. 35, no. 3/4, pp. 317-332, 1991.
- [43] F. Gesmundo, F. Viani, Y. Niu and D. L. Douglass, "Further Aspects of the Oxidation of Binary Two-Phase Alloys," *Oxidation of Metals*, vol. 39, no. 3/4, 1993.
- [44] G. R. Smolik, D. A. Petti and S. T. Schuetz, "Oxidation, Volatilization, and Redistribution of Molybdenum From TZM Alloy in Air," 2000.
- [45] M. K. Meyer, A. J. Thom and M. Akinc, "Oxide scale formation and isothermal oxidation behavior of Mo-Si-B intermetallics at 600-1000C," *Intermetallics*, vol. 7, pp. 153-162, 1999.
- [46] Y.-H. C. T.-H. F. Y.-S. C. Y.-L. C. Yu-Jen Hsiao, "Dielectric relaxation property and barrier layer formation in CrNbO₄ oxides," *Journal of Alloys and Compounds*, vol. 421, pp. 240-246, 2006.
- [47] D. Caplan and M. Cohen, "The Volatilization of Chromium Oxide," *Journal of the Electrochemical Society*, vol. 108, no. 5, pp. 438-442, 1961.
- [48] M. Skeldon, J. M. Calvert and D. G. Lees, "An Investigation of the Growth-Mechanism of Cr₂O₃ on Pure Chromium in 1 atm Oxygen at 950C," *Oxidation of Metals*, vol. 28, pp. 109-125, 1987.
- [49] F. Peng, "Pressureless Sintering and Oxidation Resistance of Zirconium Diboride Based Ceramin Composites," ProQuest, 2009.
- [50] CompuTherm, LLC., "PandatTM," Madison.
- [51] P. R. Subramanian, M. G. Mendiratta, D. M. Dimiduk and M. A. Stucke, "Advanced intermetallic alloys - beyond gamma titanium aluminides," *Materials Science and Engineering*, Vols. A239-240, pp. 1-13, 1997.
- [52] P. Patnaik, Handbook of Inorganic Chemicals, New York: McGraw-Hill, 2003.
- [53] M. E. Schlesinger, H. Okamoto, A. B. Gokhale and R. Abbaschian, "The Nb-Si (Niobium-Silicon) System," *Journal of Phase Equilibria*, vol. 14, no. 4, pp. 502-509, 1993.
- [54] E. Filipek, M. Kurzawa and G. Dabrowska, "Solid Solutions in the Cr₂O₃-aSb₂O₄-MoO₃ System," *Journal of Thermal analysis and Calorimetry*, vol. 64, pp. 1105-1111, 2001.
- [55] K. S. Thomas and S. K. Varma, "A Comparison of Static and Cyclic Long-Term Oxidation of Two Nb-Cr-Mo-Si-B Alloys," 2013.
- [56] H. Tada, A. E. Kumpel, E. R. Lathrop, J. B. Slanina, P. Nieva, P. Zavrachy, I. N. Miaoulis and P. Y. Wong, "Thermal expansion coefficient of polycrystalline silicon and silicon dioxide thin films at high temperatures," *Journal of Applied Physics*, vol. 87, no. 9, pp. 4189-4193, 2000.
- [57] P. Tabero, "Thermal Expansion of MNbO₄ Phases Where M=Al, Cr, Fe, Ga," *Journal of Thermal Analysis and Calorimetry*, vol. 88, 2007.
- [58] W. R. Manning, J. O. Hunter, F. W. Calderwood and D. W. Stacy, "Thermal Expansion of Nb₂O₅," *J. Am. Ceram. Soc.*, vol. 55, no. 7, pp. 342-347, 2006.
- [59] L. Zhang and J. Wu, "Thermal expansion and elastic moduli of the silicide based intermetallic alloys Ti₅Si₃(X) and Nb₅Si₃," *Scripta Materialia*, vol. 38, no. 2, pp. 307-313, 1997.
- [60] B. Mayer, H. Anton, E. Bott, M. Methfessel, J. Sticht, J. Harris and P. C. Schmidt, "Ab-initio calculation of the elastic constants and thermal expansion coefficients of Laves phases," *Intermetallics*, vol. 11, pp. 23-32, 2003.
- [61] A. Chatterjee, S. Srikanth, S. Sanyal, L. Krishna, K. Anand and P. R. Subramanian, "Kinetic modeling of high temperature oxidation of Ni-base alloys," *Computational Materials Science*, vol.

50, no. 3, pp. 811-819, 2011.

- [62] A. Sato, Y. L. Chiu and R. C. Reed, "Oxidation of nickel-based single-crystal superalloys for industrial gas turbine applications," *Acta Materialia*, vol. 59, pp. 225-240, 2011.
- [63] B. Voglewede, V. R. Rangel and S. K. Varma, "The effects of uncommon silicides on the oxidation behavior of alloys from the Nb-Cr-Si system," *Corrosion Science*, vol. 61, pp. 123-133, April 2012.
- [64] M. Akinc, M. K. Meyer, M. J. Kramer, A. J. Thom, J. J. Huebsch and B. Cook, "Boron-boped molybdenum silicide for structural applications," *Matl. Sci. Engr.*, vol. A261, pp. 16-23, 1999.
- [65] V. S. Braga, F. A. C. Garcia, J. A. Dias and S. C. L. Dias, "Phase Transition in Niobium Pentoxide Supported on Silica-Alumina," *J. Therm. Ana. Cal.*, vol. 92, no. 3, pp. 851-855, 2008.
- [66] H. Fritze, "High-temperature piezoelectric crystals and devices," *Journal of Electroceramics*, vol. 26, pp. 122-161, 2011.
- [67] F. Gesmundo and B. Gleeson, "Oxidation of Multicomponent Two-Phase Alloys," *Oxidation of Metals*, vol. 44, no. 1/2, 1995.
- [68] S. L. Q. S. F. Q. H. Zheng, *International Journal of Refractory Metals & Hard Materials*, vol. 26, pp. 1-4, 2008.
- [69] R. S. R. a. H. S. P. J. R. J. L. Waring, vol. 77, J. Res. Natl. Bur. Stand., 1973, pp. 705-711.
- [70] B. P. a. S. V. J. Ventura, *Journal of Alloys and Compounds*, vol. 476, no. 1-2, pp. 257-262, 12 May 2009.
- [71] W.-Y. Kim, H. Tanaka and S. Hanada, "Microstructure and high temperature strength at 1773 K of NbSS/Nb5Si3 composites alloyed with molybdenum," *Intermetallics*, vol. 10, pp. 625-634, 2002.
- [72] W. Li, H. Yang, A. Shan, L. Zhang and J. Wu, "Effect of Mo addition on the phase stability of b-Nb5Si3 phase," *Intermetallics*, vol. 14, pp. 392-395, 2006.
- [73] D. V. Myasnikov, A. V. Konyashkin and O. A. Ryabushkin, "Identification of eigenmodes of volume piezoelectric resonators in resonant ultrasound spectroscopy," *Technical Physics Letters*, vol. 36, no. 7, pp. 632-635, July 2010.
- [74] S. Qu, Y. Han and L. Song, "Effects of alloying elements on phase stability in Nb-Si system intermetallics materials," *Intermetallics*, vol. 15, pp. 810-813, 2007.
- [75] S.-y. Qu, R.-m. Wang and Y.-f. Han, "Microstructure of Nb/Nb5Si3 in-situ composites," *Trans. Nonferrous Met. Soc. China*, vol. 12, no. 4, pp. 691-694, August 2002.
- [76] C. X. A. K. M. K. Y. T. H. I. M. Y. T. Murakami, *Intermetallics*, vol. 7, pp. 1043-1048, 1999.
- [77] C. Valot, D. Ciosmak and M. Lallemand, "Morphological Characteristics of the Oxidation of Niobium II: The Role of Stresses on High-Temperature Morphologies," *Oxidation of Metals*, vol. 41, pp. 235-250, Nov 1994.
- [78] H. T. a. S. H. Won-Yong Kim, "Microstructure and high temperature strength at 1773 K of Nbss/Nb5Si3 composites alloyed with molybdenum," *Intermetallics*, vol. 10, pp. 625-634, 2006.
- [79] K. Yongwang, H. Yafang, Q. Shiyu and S. Jinxia, "Effects of Alloying Elements Ti, Cr, Al, and Hf on b-Nb5Si3 from First-principles Calculations," *Chinese Journal of Aeronautics*, vol. 22, pp. 206-210, 2009.

Vita

Kathryn Thomas was born in Alamosa, Colorado on July 1st , 1989; soon after the family moved to El Paso, Texas. The only child of John and Diane Thomas, she graduated from Andress High School, El Paso, Texas in the spring of 2007 as salutatorian and entered The University of Texas at El Paso in the fall with the Presidential Scholarship. She received her Bachelor of Science degree in Metallurgical and Materials Engineering in 2012 and joined the Materials Science and Engineering program that summer.

While pursuing her bachelor's degree in Metallurgical and Materials Engineering she worked as an undergraduate research assistant on a project associated with the Office of Naval Research. As a graduate student she acted as a teaching assistant for Dr. S. K. Varma in his classes, Nanofunctional Physical Metallurgy, Mechanical Behavior of Materials, and Phase Transformations. She presented work at various international conferences including the Materials Science and Technology 2011, 2012, 2014 Conference and The Minerals, Metals & Materials Society 2013, 2014, and 2015 Annual Meeting & Exposition. Her work on "A Comparison of Static and Cyclic Long Term Oxidation of Two Nb-Cr-Mo-Si-B Alloys" was published in Metallurgical and Materials Transactions A in 2013 and work on the 15Mo system is published in MMA entitled "Microstructural Analysis of Three Nb-Alloys."

Permanent address: 3109 Mesa Verde Ln.
El Paso, TX, 79904

This dissertation was typed by Kathryn S. Thomas.